Spin Transport in Carbon Nanotubes with Circular Nanodot Contacts

Dissertation

der Mathematisch-Naturwissenschaftlichen Fakultät
der Eberhard Karls Universität Tübingen
zu Erlangung des Grades eines
Doktors der Naturwissenschaften
(Dr. rer. nat.)

vorgelegt von
Serhat Şahakalkan
aus Ankara/Türkei

Tübingen
2017

Gedruckt mit Genehmigung der Mathematisch-Naturwissenschaftlichen Fakultät der Eberhard Karls Universität Tübingen.

Tag der mündlichen Qualifikation:	26.06.2018
Dekan:	Prof. Dr. Wolfgang Rosenstiel
1. Berichterstatter:	Prof. Dr. David Wharam
2. Berichterstatter:	Prof. Dr. Dieter P. Kern

ITHAKA

As you set out for Ithaka
hope your road is a long one,
full of adventure, full of discovery.
Laistrygonians, Cyclops,
angry Poseidon - don't be afraid of them:
you'll never find things like that one on your way
as long as you keep your thoughts raised high,
as long as a rare excitement
stirs your spirit and your body.
.....

Hope your road is a long one.
May there be many summer mornings when,
with what pleasure, what joy,
you enter harbours you're seeing for the first time;
may you stop at Phoenician trading stations
to buy fine things,
.....

Keep Ithaka always in your mind.
Arriving there is what you're destined for.
But don't hurry the journey at all.
Better if it lasts for years,
so you're old by the time you reach the island,
wealthy with all you've gained on the way,
not expecting Ithaka to make you rich.

Ithaka gave you the marvellous journey.
Without her you wouldn't have set out.

She has nothing left to give you now.

And if you find her poor, Ithaka won't have fooled you.

Wise as you will have become, so full of experience,

you'll have understood by then what these Ithakas mean

Constantine Cavafy, Alexandria, 1911

Zusammenfassung

Die Entwicklungen der letzten Jahrzehnte zeigen eine deutliche Wandlung der sozio-ökonomischen Strukturen. Die digitalen Medien und ihre Anwendungen beherrschen unser Leben. Wir sind im sogenannten Informationszeitalter angekommen, welches seinen Namen der Haupthandelsware, der Information, zu verdanken hat. Diese Wandlung wurde durch die rasante Entwicklung des Internets und der Geräte möglich. Dieser liegt die sehr schnelle Entwicklung der Rechenleistung der Geräte zugrunde, welche wiederum durch die Miniaturisierung von integrierten Schaltungen möglich wurde. Es wird aber vorausgesagt, dass diese Miniaturisierung bald an ihre physikalischen Grenzen stoßen wird. Deshalb sind viele Hochtechnologie-Unternehmen und Forscher auf der Suche nach Kandidaten, die diese Entwicklung weiter fortsetzen könnten. Einige Forschergruppen untersuchen neue Materialien, andere wollen eine prinzipielle Umstellung der bisher bekannten Elektronik.

Als Material werden unter anderem, auch aufgrund ihrer Größe, Nanomaterialien in Betracht gezogen. **Kohlenstoff-Nanoröhren (CNT)** sind einer der erfolgversprechenden Kandidaten. Diese sind faserartige reine Kohlenstoff-Makromoleküle, welche eine sehr hohe mechanische und thermische Stabilität mit einer hohen elektrischen Leitfähigkeit verbinden. Sie können sowohl

halbleitend oder auch metallisch leitend sein.

Als eine prinzipielle Umstellung der Elektronik werden Themen wie Quanten-Computing oder **Spintronik** in Betracht gezogen, wobei es sich bei der letzteren um eine neuere Elektronik handelt, welche außer der Ladung des Elektrons auch dessen intrinsisches magnetisches Moment, den **Spin**, mit einbezieht. Interessanterweise weisen die Kohlenstoff-Nanoröhren eine geringe Spin-Bahn-Kopplung auf, was sie zu einem geeigneten Material für einen besseren Spin-Transport macht. In solchen Materialien kann aufgrund der geringen Spin-Relaxation die Spin-Polarisation länger aufrecht gehalten werden.

Um diese zwei neuen Ansätze miteinander kombinieren zu können, haben wir uns für die Untersuchung des Spin Transports innerhalb von Kohlenstoff-Nanoröhren entschieden. Dafür haben wir uns die **Spin-Ventil** Konfiguration ausgesucht. Es handelt sich dabei um eine einwandige Kohlenstoff-Nanoröhre (SWNT), welche mit ferromagnetischen Metallen an beiden Enden kontaktiert worden ist. Diese Anordnung ist ihrem Pendant aus der Optik mit einem Polarisator und einem Analysator sehr ähnlich. Die Polarisationsrichtung des Elektronenspins wird in diesem Fall durch die Magnetisierungsrichtung der Kontakte vorgegeben. Ein bekanntes Beispiel sind Multilagen aus ferromagnetischen und nicht magnetischen Metallen, die auf dem Riesenmagnetowiderstand (GMR) Effekt basieren, dessen Entdeckung 2007 mit dem Nobelpreis ausgezeichnet wurde. Bei diesem Effekt ändert sich der elektrische Widerstand der Struktur schlagartig, wenn die Magnetisierungsrichtung durch ein äußeres Feld von parallel auf antiparallel umgeschaltet wird. Der Widerstand kommt auf den Ausganswert wieder zurück, wenn sich die zweite Schicht auch umschaltet und die Magnetisierung der beiden Seiten wieder parallel ist. Bei unseren anfänglichen

Versuchen haben wir immer wieder nicht eindeutig identifizierbare Effekte beobachtet, wie z.B. Stufen im Signal, das Schalten zwischen zwei Niveaus oder das nicht-symmetrische Schalten. Diese können auf das nacheinander Schalten von benachbarten ferromagnetischen Domänen zurückgeführt werden, jedoch ist die Deutung der Messergebnisse beliebig kompliziert und nicht reproduzierbar. Deshalb haben wir uns zunächst mit der Domänen-Struktur der benutzten Kontakte beschäftigt.

Einen entscheidenden Beitrag zum Erfolg der Spin-Transport-Versuche haben unsere Magnetkraftmikroskopie-Untersuchungen der Kontakte geleistet. Wir haben die Beobachtung gemacht, dass eckige oder lange stäbchenförmige Kontakte vermehrt zur Bildung von Multidomänen neigen. Im Gegensatz dazu haben runde Dünnfilm-Schichten in einem bestimmten Größenbereich zwei Grundmagnetisierungszustände: Entweder bilden sie einen Vortex oder sie bilden eine Einzel-Domäne. Dadurch ist das magnetische Umschaltverhalten deutlich einfacher zu verstehen. Auf diese Untersuchungen basierend, haben wir uns für runde, flache Kontakte entschieden. Solche Diskus-förmige ferromagnetische Dünnfilm-Strukturen im Sub-µm-Bereich sind unter Forschern aus dem Gebiet der magnetischen Materialien auch als **Nanodot** bekannt.

Es hat sich gezeigt, dass solche mit Nanodots kontaktierte Spin-Ventile aus SWNTs sich sehr gut für die Untersuchung des Spin-Transports eignen. Diese Arbeit ist, soweit uns bekannt, die erste, die den Spin-Transport in SWNTs mit runden Nanodot Kontakten untersucht. Mit dieser Anordnung konnten wir einen hoch-reproduzierbaren, scharf definierten und symmetrischen **Tunnel-Magnetwiderstand (TMR)** von bis zu -70 % messen. Dieser Wert ist deutlich höher als der bisher von CNT-Spin-Ventilen berichtete Wert von 30 %. Basierend auf dem

Jullière Model ergibt dieser Wert einen Spin-Polarizationsgrad innerhalb der Co-Kontakte von 48 %, was in guter Übereinstimmung mit anderen Werten aus der Literatur ist. Dieses Ergebnis führt uns zu der Annahme, dass die Spin-Polarisation über die gesamt Länge der SWNT von 950 nm erhalten bleibt.

Aus der Literatur ist bekannt, dass die benutzte Probengeometrie mit einer SWNT zwischen zwei metallischen Kontakten unter bestimmten Bedingungen einen sogenannten **Quanten-Punkt (QD)** bildet. So eine QD Struktur zeigt in ihrem Transportverhalten Oszillationen des Leitwerts, die sogenannte Coulomb-Blockade. In unserem Fall mit ferromagnetischen Kontakten konnten wir einen negativen Zusammenhang des TMR mit den Oszillationen des Leitwerts beobachten. Bei hohem Leitwert zeigt sich ein hoher negativer TMR, welcher dann in den Bereichen der Blockade auf einen kleinen Wert bis hin zu Null fällt. Dieses gegensätzliche Verhalten kann auf das Umklappen des Spins (Spin-Flip) während des Tunnelns zurückgeführt werden, welches wiederum durch die Absorption oder Emission von Magnonen verursacht wird.

Eine besondere Beobachtung, welches auch die Spin-Flip Idee unterstützt, ist der **Stromfluss bei 0 V Bias-Spannung**. Durch die langsame Veränderung der Gatespannung können die einzelnen Energieniveaus des Quantenpunkts durchgestimmt werden. Dabei konnte die Beobachtung gemacht werden, dass bei der Annährung eines Energieniveaus, z. B. von der negativen Gatespannungsseite zuerst der Strom in negativer Richtung fließt und sich auf der anderen Seite des Energieniveaus in die positive Richtung ändert. Solch ein Stromfluss bei Null Spannung wird in der Literatur mit einem magnon-assitierten Tunneln beschrieben. Die Richtung ergibt sich durch ungleichmäßige Kopplung der beiden ferromagnetischen Kontakte. Und der Richtungswechsel

des Stroms ergibt sich dadurch, dass das Elektron von einem, relativ zum Ferminiveau der Elektroden niedrigen QD-Niveau aus, ein Magnon absorbiert und somit in die Elektrode eindringen kann oder von der Elektrode aus wieder durch die Absorption eines Magnons in ein höheres QD-Niveau aufsteigt. Obwohl dieser Mechanismus schon in der Literatur theoretisch besprochen wurde, ist diese Arbeit die erste experimentelle Beobachtung, die mit dieser Theorie beschrieben werden kann.

Des weiteren wurde eine starke Abhängigkeit des TMR-Werts von der Bias-Spannung beobachtet. Während sich die sehr hohen absoluten TMR-Werte bei sehr geringen Spannung zeigten (bis zu null Volt), fallen diese Werte sehr rapide mit dem Anstieg der Bias-Spannung. Es ergibt sich eine Modulation des TMR-Werts, der auch einen Vorzeichenwechsel zeigt. Aber insgesamt geht der TMR-Wert gegen Null bei steigender Bias-Spannung. Dieser Effekt legt nahe, dass bei steigender Bias-Spannung die Spin-Polarisation stark abnimmt.

Contents

List of Symbols and Abbreviations

χ	Susceptibility
ΔE	Energy difference between states of a quantum dot
$\Gamma_{S,D}$	Tunneling barrier strenght of source, drain contact
μ	Permeability
μ_B	Bohr magneton
μ_e	Electron mobility
σ	Conductivity
ϱ	Resistivity
$\vec{a}_{1,2}$	Base vectors of hexagonal graphene lattice
$\vec{B}$	Magnetic flux density
$\vec{C}_h$	Chiral vector
$\vec{H}$	Magnetic field intensity
E_C	Charging energy
E_F	Fermi energy
$g(E)$	Density of states
G_0	Conductance quantum
H_a	Annihilation field
H_{Ci}	Intrinsic coerciv field
H_C	Coerciv field

H_n ..... Nucleation field
$I_{P,AP}$ ..... Current in the parallel, antiparallel configuration
I_{SD} ..... Source-drain current
l_m ..... Electron mean free path
M_R ..... Remanent magnetization
M_S ..... Saturation magnetization
P_i ..... Spin polarization degree of contact i=1,2
$R_{P,AP}$ ..... Resistance for parallel, antiparallel configuration
R_Q ..... Resistance quantum
T_C ..... Curie temperature
V_{SD} ..... Source-drain bias voltage
AFM ..... Atomic force microscopy
AMR ..... Anisotropic magnetoresistance
BZ ..... Brillion zone
CB ..... Coulomb blockade
CHP N-Cyclohexyl-2-pyrrolidone
CIA ..... Current-induced annealing
CIP ..... Current in plane
CNT ..... Carbon nanotube
CNT-SV ... Carbon nanotube - spin valve
CPP ..... Current perpendicular to plane
DAS ..... N-[3-(Trimethoxysilyl)Propyl] Ethylenediamine
DMS ..... Dilute magnetic semiconductor
DOS ..... Density of states
EBL ..... Electron beam lithography
ES ..... Excited states
FET ..... Field effect transistor
FM ..... Ferromagnetic metal
GMR ..... Giant magnetoresistance
ITRS ..... International Technology Roadmap for Semiconductors

LSMO..... Lanthanum strontium manganite
MFM..... Magnetic force microscopy
MIBK..... Methyl isobutyl ketone
MR ..... Magnetoresistance
MTJ ..... Magnetic tunnel junction
MWNT .... Multi walled carbon nanotube
NM ..... Nonmagnetic metal
NMP N-Methyl-2-pyrrolidon
PMMA..... Poly(methyl methacrylate)
PVD ..... Physical vapor deposition
QD..... Quantum dot
s ..... Spin quantum number
SDS..... Sodium dodecyl sulfate
SEM ..... Scanning electron microscopy
spin-FET... Spin field effect transistor
STM ..... Scanning tunneling microscopy
SV ..... Spin valve
SWNT ..... Single walled carbon nanotube
SWNT-QD-SV Single walled carbon nanotube - quantum dot - spin valve
SWNT-SV.. Single walled carbon nanotube - spin valve
TEM ..... Transmission electron microscopy
TMR..... Tunneling magnetoresistance
US ..... Ultrasound

Chapter 1

Motivation

We are living now in the so called *Information Age*, which could be considered as the third main socioeconomic formation after the agricultural and the industrial age. It is named after its main article of trade: *The Information* [1].

Within the recent two or three decades one could observe many signs of an evolution in society. One important feature is the increase of the number of people working in information industry compared to the number of people working in manufacturing jobs. This shift is a direct consequence of the technological development. With better technologies only a few people are needed to supply many others with food or other essentials. So that these many others were somehow pushed to find other goods to trade with like information.

We saw in the past several years how fast the internet developed and how important it became as the major platform for trading intellectual goods. Its vertiginous development was primarily possible because of the continuous miniaturization of the used technology. This progress was mainly pursued by the

profit-oriented industry according to *Moore's Law* [2], which says that roughly every second year the number of elements on an integrated circuit doubles. Probably this was a self-fulfilling prophecy, but nevertheless such a trend certainly can not be upheld infinitely. Within the recent years critical sizes of components on integrated circuits approached values around 10 nanometer. Therefore the industry had to utilize more and more expensive techniques to fulfill the requirements of the International Technology Roadmap for Semiconductors (ITRS) [3]. This international organization of the semiconductor companies foresees also that the miniaturization is speeding towards a brick wall of physical limitations. In order to meet the demands of this newly born age, the industry and also the researchers agree that there is an urgent need for a conceptual change of the technology used so far.

One of the proposals is to integrate the *Spin* into *Electronics*. This idea created a whole area of research, namely *Spintronics*. The spin of the electron is a kind of intrinsic angular momentum, which can have only two possible values pointing either up or down in the measured direction. It is mostly referred to as the spin-up or spin-down state of the electron. The spin is a purely quantum mechanical phenomenon and cannot be explained by classical means [4]. This additional degree of freedom with its inherent binary structure makes it a promising candidate for memory and logic applications. Such applications would have then the great benefit of being faster, nonvolatile and less power consuming [5]. In our common electronics most of the power is consumed to bring up the electrons into the conduction band, which is then actually only heating our lap while using our laptops. Due to the big challenges in the implementation of this property of the electron it was ignored for a long time by

the electronic industry. The discovery of the *Giant Magnetoresistance Effect* (GMR) was the first step to change this opinion. In the years 1987/88 two independent groups of, ALBERT FERT [6] in France and of PETER GRÜNBERG [7] in Germany, had made similar measurements on multilayers of alternating ferromagnetic and nonmagnetic metals. They had observed a huge change in the resistance of such structures, depending on the relative magnetic orientation of the ferromagnetic layers. Compared to other already known bulk magnetoresistances of a few percentages this effect was considered gigantic with its up to 65% magnetoresistance. Later it was even shown that with a slightly different configuration, which is then called the *Tunneling Magnetoressistance* (TMR) it is even possible to reach values up to 600% at room temperature [8] and even 1800% at 4,2K [9]. TMR and GMR are both based on the spin dependent scattering of the electrons while they travel through the structure. This discovery revolutionized the data storage and showed how important the role of the spin in electronics could be. Grünberg was the first one to recognize this importance and quickly patented the sensor application. IBM was then the first company to develop the technology for sensors based on GMR [10]. In 1997 they introduced commercially their multilayer GMR sensor named Deskstar16 GP [11]. Such read head sensors are now used in almost all hard disk drives of computers. For this important discovery Fert and Grünberg were rewarded the Nobel Prize in Physics in 2007.

Other proposals consider the incorporation of novel nano materials into the existing technology or even the replacement of the major component silicon. Among this novel nano materials *carbon nanotubes* (CNT) are the most famous ones. CNTs are tubules consisting of carbon atoms. They can be imagined as rolled up single atomic sheets of carbon, the so called *graphene*,

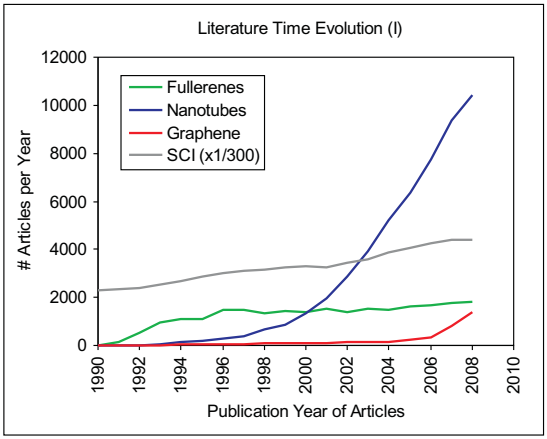

Figure 1.1: Time-dependent number of articles dealing with fullerenes, nanotubes, and graphene based on the Science Citation Index (SCI) and the Conference Proceedings Citation Index, Science (CPCI-S). The total number of articles covered by the SCI is shown as a rough measure for the growth of scientific literature [14, 15]. By courtesy of Werner Marx, CPT information service of MPG.

which is the highly esteemed material of research within the recent years. After their discovery in 1991 by Sumio Ijima [12] CNTs attracted a lot of attention. The huge increase of the number of publications dealing with carbon nanotubes can be seen in Fig. 1.1. This big interest is founded on their unique properties. They are small, can carry high currents, can be either semiconducting or metallic. They are stronger than steel and have a thermal conductance higher than diamond [13]. So all in all they are almost the philosophers stone. An other important advantage CNTs could offer is the long spin life time, due to their small spin-orbit coupling. Therefore strongly spin polarized currents can be transported through long nanotubes.

Taking these promising proposals into account we investigated spin transport in carbon nanotubes. Our main concern was on the problem of identifying the spin signal and the modulation of the spin signal with applied electric fields. In order to give a detailed explanation of our measurements the first 4 chapters are intended as an introduction. In **Chapter 2** the used material carbon nanotubes is introduced in detail with its structural, electronic and transport properties. Then in the **3rd Chapter** the spin phenomenon and its quantum nature are discussed, where also the work of others done so far is shown. **Chapter 4** is devoted to magnetism and miscellaneous magnetoresistance effects. The experimental efforts leading to our measurements are then introduced in the **5th Chapter**. In this chapter also our investigation of the domain structure is presented. This study delivered important insight which was significant for obtaining the main results of this work. In **Chapter 6** the results of our spin measurements on CNT are presented and discussed. Finally this dissertation is concluded with the **7th Chapter** as a summary and outlook.

Chapter 2

Carbon Nanotubes

In this chapter structural and electronic characteristics of carbon nanotubes (CNT) will be introduced. Also the electrical transport behavior of CNTs is described and, because of the experimental relevance, CNTs in a quantum dot configuration are shown.

2.1 Structure and Properties of Carbon Nanotubes

Carbon is one of the most interesting elements in the periodic table. It is the element with the largest variety of chemical combinations. Maybe that's the reason why life on earth is so versatile. Carbon is a four-valent atom but it can form single, double or triple bonds. This is due to the different mixing of its 2s- and 2p-orbitals, the *hybridization*. Carbon is known since the ancient times in its two famous allotropes namely diamond Fig. 2.1a) and graphite Fig. 2.1b). During the recent three decades new forms of carbon were discovered, the fullerenes Fig. 2.1c),

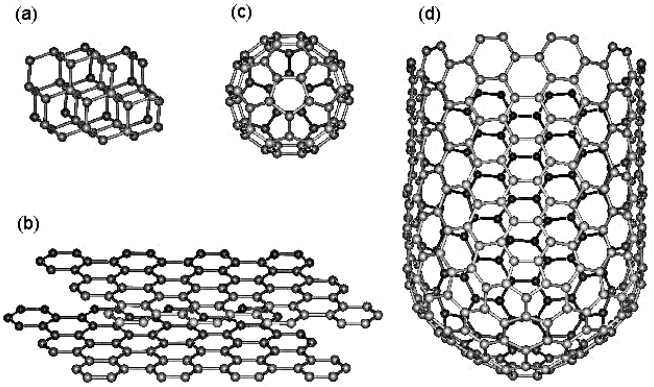

Figure 2.1: Atomic structure of the allotropes of carbon a) diamond b) graphite c) fullerene d) carbon nanotube.

carbon nanotubes Fig. 2.1d) and several years ago the realization of graphene. Although sometimes these are regarded as new allotropes, they are closely related to graphite. In fact, graphene is a single layer of graphite, and the others are bent forms of graphene, into a ball in the case of fullerenes and into a tube in the case of the nanotube. Because of their extraordinary properties each of them attracted a lot of attention in the scientific community. This interest was so much that in 1996 the discovery of fullerens and recently in 2010 the ground breaking experiments with graphene were rewarded with the Nobel Prize in chemistry and physics, respectively.

Although others had reported [16] earlier about tubular structures in carbonaceous materials, Ijima [12] was the first one to identify the atomic structure of carbon nanotubes. They can be imagined as rolled up sheets of single atomic layers thus forming seamless tubes. These tubes consist of either a single wall (SWNT) or of many tubes stacked concentrically into each other, which are then called multi walled carbon nanotubes (MWNT).

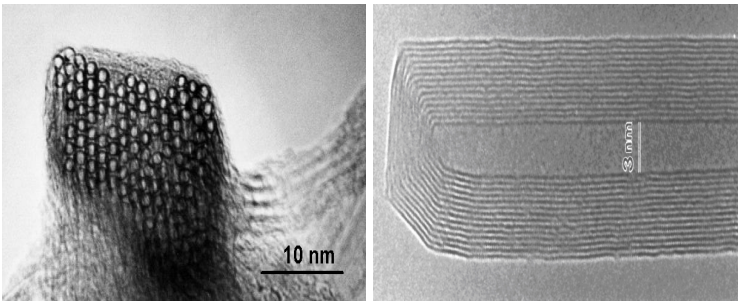

Figure 2.2: Transmission electron microscope images of carbon nanotubes: A bundle of SWNT on the left [17] and a multi walled carbon nanotube on the right [18].

Examples of transmission electron microscopic (TEM) images of SWNT and MWNT can be seen on Fig. 2.2a) and b), respectively. As can be seen from these images, the layers of the MWNT and the individual SWNT in the bundle are very close to each other, which is comparable to the graphitic interlayer distance of about 3 Å.

In this work we will mainly focus on individual single walled tubes in order to avoid any interaction between the layers of a MWNT or between the tubes within a bundle, which could disturb or cover the magnetic effects under investigation.

SWNT are divided into three categories. The names given them depend on the shape of the edge formed, when they are cut perpendicular to their axis. This shape is determined by the relative orientation of the hexagons with respect to the tube axis, see right side of Fig. 2.3. In the case of helical tubes Fig. 2.3c) an angle is formed between the bottom line of the hexagon and the tube axis which can have any value between 0° and 30°. The special cases of 0° and 30° are called zig-zag Fig. 2.3a) and armchair Fig. 2.3b), respectively. Because of the six fold

symmetry of a hexagon all other angles are equivalent or mirror symmetric.

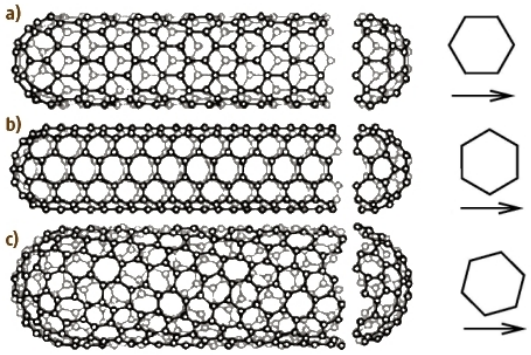

Figure 2.3: Different types of SWNTs a) zigzag b) armchair and c) helical tubes (adapted from [19]).

To identify the different types of CNT a closer look at the graphene crystal structure is necessary. The graphene lattice which is indicated by the hollow circles in Fig. 2.4 is spanned by two base vectors $\vec{a}_1$ and $\vec{a}_2$. The primitive unit cell is shown as the gray shaded area and contains the basis of two carbon atoms. The lattice of graphene could also be constructed from two different triangular sublattices which themselves would not be Bravais-lattices. They are indicated as red and blue triangles in Fig. 2.4.

To form a CNT one has to roll the single atomic carbon layer into a seamless tube. It has to be rolled in such a way that the starting lattice point coincides with an other lattice point. The vector connecting the starting lattice point with the end lattice point is the so called *chiral vector* $\vec{C}_h$. The terms chiral and chirality are widely used in connection with carbon nanotubes, but we should emphasize that these terms don‘t refer to the

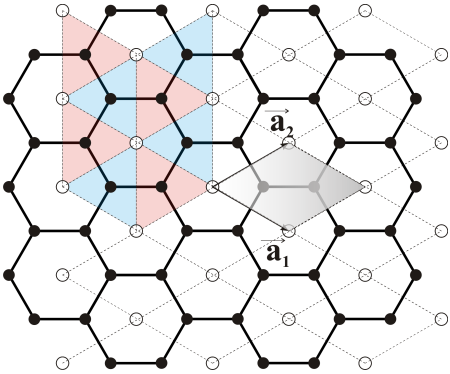

Figure 2.4: Ball and stick model of graphene. The open circles with the dashed lines are representing the underlying hexagonal lattice. Red and blue triangles show the two sublattices. The gray shaded area is representing the primitive unit cell of graphene, which is spanned by the basis vectors a_1 and a_2. There are two atoms in a unit cell.

handedness of the CNT. They rather want to point out that CNT can have a helicity. Therefore this somewhat misleading term *chiral vector* will be substituted in this text by *rolling vector*. This vector can be written as a sum of the two base vectors:

$$\vec{C}_h = n\vec{a}_1 + m\vec{a}_2 \tag{2.1}$$

(see Fig. 2.5). With this relation and the requirement $(n \geq m)$, all different possibilities to form a tube, are uniquely identified. The integer pair (n, m) are the so called indices and are used as a short notation to identify the CNT. As an example the construction of a tube is depicted in Fig. 2.5. The hexagonal mesh is cut and rolled in such a way that the origin O lies afterwards on the point A and the point B lies on C. This tube is than named according to $\vec{C}_h = 8\vec{a_1} + 4\vec{a_2}$, as a (8,4) tube. The length of the rolling vector is also the circumference of the tube and from this

the diameter of the tube can be calculated as follows:

$$d = \frac{1}{\pi}\left|\vec{C_h}\right| = \frac{a}{\pi}\sqrt{n^2 + nm + m^2} \tag{2.2}$$

where $a = 2,46\text{Å}$ is the length of the base vectors.

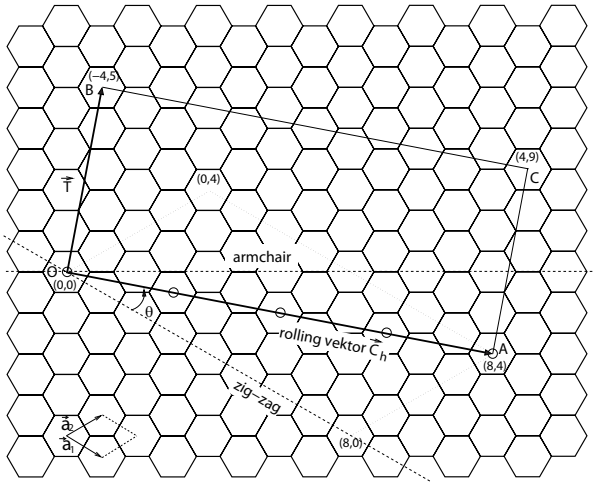

Figure 2.5: Graphene lattice with unit cell and the base vectors a_1 and a_2. The construction of a CNT is shown on the example of a (8,4) tube (adapted from [19]).

The two dashed lines in Fig. 2.5 show the borders for the rolling vector. All nanotubes formed with a rolling vector within these borders are of helical type. The angle between the zig-zag line (see Fig. 2.5) and the rolling vector is then the above mentioned chiral angle. If the vector is lying on the horizontal line then $n = m$ and the so formed tubes are the so called armchair tubes. If the vector lies on the other border, then $m = 0$ and the tubes are of the so called zig-zag type. The rectangle formed by the two vectors $\vec{C_h}$ and $\vec{T}$ is the unit cell of the CNT. $\vec{T}$ is the so called translational vector and corresponds to the unit vector of

the carbon nanotube. It is perpendicular to rolling vector and points from the origin O to the first lattice point along its direction. It can be expressed also like the rolling vector in terms of the base vectors of the graphene lattice as:

$$\vec{T} = t_1\vec{a}_1 + t_2\vec{a}_2 \tag{2.3}$$

The integers t_1 and t_2 are given in terms of the indices (n,m) of the corresponding CNT as:

$$t_1 = \frac{2m+n}{d_r}, \quad t_2 = -\frac{2n+m}{d_r} \tag{2.4}$$

where d_r is the greatest common divisor of $(2m+n)$ and $(2n+m)$.

2.2 Electronic Properties of Carbon Nanotubes

Besides their extraordinary mechanical properties carbon nanotubes have also excellent electronic properties. In order to understand this we have to start again from graphene. In graphene the electrons are sp^2-hybridized. This results in three strong σ-bonds between neighboring carbon atoms and the weakly bondig π-bond. This weak bond is responsible for the loose binding of the graphene layers in graphite. Since the electron in the p_z-orbital is also weakly bound it is delocalized over the whole area of graphene and is mainly determining the electronic properties of graphene. With tight binding calculations the energy dispersion of the π electrons can be obtained, which is shown in Fig. 2.6 within the first Brillion Zone (BZ). As can be seen, the binding π (last valence) and the anti binding $\pi^\star$ (first conduction) bands

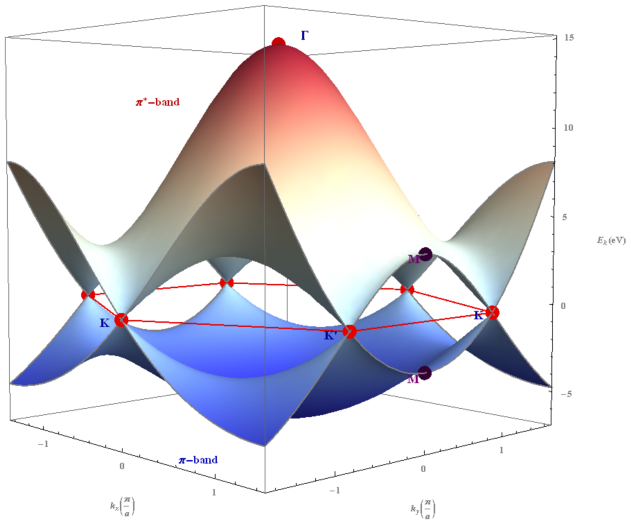

Figure 2.6: First Brillouin Zone and the energy dispersion relation of graphene. The upper conduction band and the lower valance bands touch each other at the K points. Therefore graphene is called a zero bandgap semiconductor [21][19].

touch each other at the symmetry points K and K'. This is the reason why graphene is called a zero bandgap semiconductor. For undoped graphene the Fermi level lies at these intersection points. The density of states (DOS) at this point is zero, accordingly the conductivity of undoped graphene is fairly low. It is in the order of the quantum conductance $G_0 \sim e^2/h$ [20].

To obtain the electronic structure of carbon nanotubes one has to superimpose the periodic boundary condition, that a CNT

is a tube, to the electronic structure of graphene. This is because of the quantum mechanical constraint that the electron wave has to interfere with itself constructively when it travels around the tube. This boundary condition results in the first Brillouin Zone for the CNTs, which is a set of equidistant lines. These so called *cutting-lines* are actually a subset of points of the band structure of graphene. As can be seen in Fig. 2.7, they differ for different CNT. The length and the spacing of these lines depend on the (n,m) indices. When these lines cross the symmetry point K or K' the bands touch each other and the corresponding CNT is metallic. For example this is the case for an (8,8) or an (8,2) tube, as can be seen from Fig. 2.7b) and c) where the bands are crossing each other. In contrast, in the case of a (8,0) tube (see Fig. 2.7a)) there is a gap between the bands. This means that there are no available states in the gap and such a tube is then a semiconducting tube. The band gap of the semiconducting CNTs are inversely proportional to their diameter.

$$\triangle E_g = \frac{2\pi a_c \gamma_0}{\sqrt{3}\left|\vec{C}_h\right|} \tag{2.5}$$

where γ_0 is the nearest-neighbor hopping energy ($\gamma_0 \approx 2.8$ eV) and a_c is the carbon-carbon bond length ($a_c \approx 1.42$Å) [22]. For a typical CNT with diameter of around 1.4 nm the gap is around $0,5\ eV$. For example, for the (17,0) tube the Eq. 2.5 gives a band gap of $\Delta E_g \simeq 0.59\ eV$.

The rolling vector determines if a tube is semiconducting or metallic. This means whenever $n-m$ is an integer multiple of 3 then the CNT is metallic, otherwise semiconducting.

$$m - n = 3j\,, \qquad j \in \mathbb{Z} \tag{2.6}$$

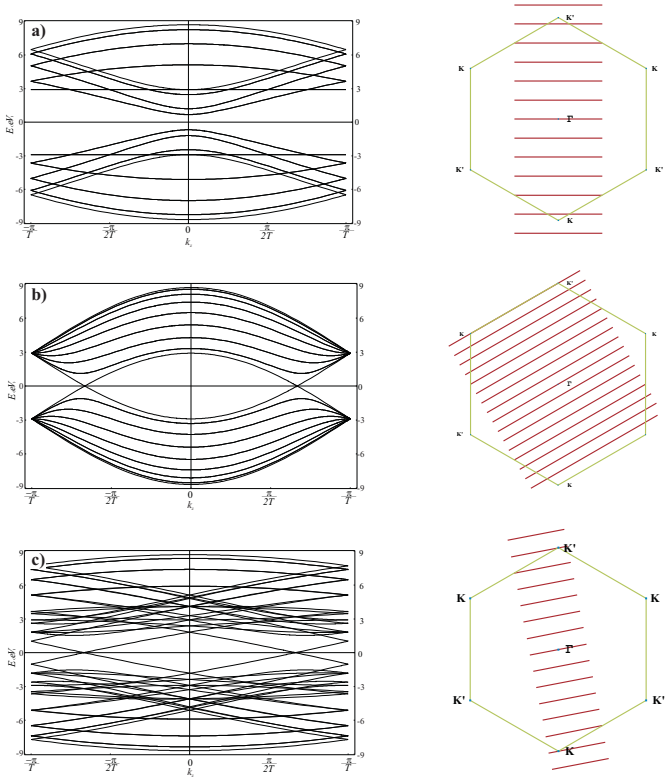

Figure 2.7: 1D Energy bands of a) (8,0), b) (8,8), c) (8,2) tubes with the corresponding cutting lines on the right, which arise due to the periodic boundary condition [23][24][19].

This is the case for all armchair tubes whereas the helical and zig-zag tubes can be of both types. The armchair tubes are also the so called *true metallic* ones. Because of the curvature and bending effects all other metallic tubes open a small band gap in the order of $10\,meV$. Such tubes are then called *small band gap* tubes.

Unfortunately, until now it is not possible to synthesize CNTs purely with the desired conduction type. But there are great efforts to enrich the amount of one type or to separate them after production [25]. The different rolling possibilities of a sheet of graphene in terms of the conduction type is shown in Fig. 2.8, blue dots represent metallic and red ones semiconducting CNTs. From this distribution we can deduce that $^2/_3$ of all possible CNTs are of semiconducting type [26].

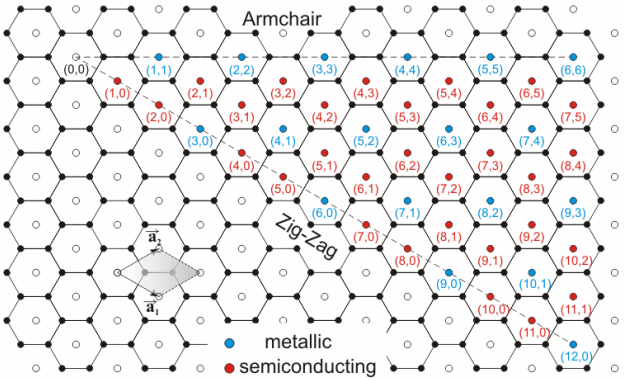

Figure 2.8: Graphene lattice showing the different possibilities of generating semiconducting or metallic SWNTs. The blue (n,m) indices represent metallic tubes and the red ones semiconducting tubes (adapted from [26]).

2.3 Transport Properties of Carbon Nanotubes

The extraordinary electronic properties of CNTs has fascinated researchers all over the world. There is certainly a fundamental interest to understand the underlying transport properties. Beyond this there is also an enormous interest to integrate them into electronic devices like *field effect transistors* (FETs) [27, 28]. At this point the question about the resistance arises. Resistance is the effect in matter to hinder the charge carriers to flow freely. It is caused by scattering of the charge carriers at static perturbations like defects or impurities and at lattice vibrations (*phonons*). At higher temperatures scattering at phonons is more dominant but with decreasing temperature the scattering at perturbations prevails. Scattering in 1D is different than in higher dimensions. Due to the dimensional constraints charge carriers are limited to scatter either forward or backward. In addition, in momentum space, available states for backscattering, which satisfy also the momentum and energy conservation, are also limited. Therefore the backscattering in SWNTs is suppressed. Carbon nanotubes are nearly perfect crystals and have only few defects and impurities. All this results in a very long *mean free path* l_m, this is the distance electrons travel in average before they undergo any scattering event. For metallic SWNTs a very long l_m has been measured, around $1\,\mu m$ at room temperature and even up $10\,\mu m$ at temperatures below 50 K [29]. This distance is an important characteristic length in mesoscopic science. If the mean free path becomes comparable to the sizes of the object under investigation, interesting phenomena like *ballistic transport* occur. This means that in such materials electrons can move without any collisions, unlike in diffusive systems. Ma-

terials in the ballistic conduction regime don´t have an internal resistance. Such systems are usually low-dimensional. At the interface between low and high dimensional materials e.g. at the contacts, a resistance occurs. This is caused by the mismatch of energy levels. To understand such phenomena we have to look at the Landauer Formula, which is describing transport in low dimensions. According to this formalism, the conductance of a 1D system is given by:

$$G = \frac{e^2}{h} \sum_i T_i \left(E_F \right) \tag{2.7}$$

where T_i is the transmission probability of the i´th 1D subband at the Fermi energy. For a carbon nanotube in the ballistic regime with ideal contacts we get a conductance of $G = 4G_0 = 4\frac{e^2}{h}$. This is four times the *conductance quantum* G_0, because of the four fold degeneracy at this energy level. As mentioned earlier, the Brilloin Zone of the CNT consist of subbands. Those subbands near K and K' form two valleys, which correspond to the clockwise and counterclockwise motion of the electron around tube. The other two fold degeneracy is because of two different spin orientations of the electrons in each of these subbands. This corresponds to four conduction channels, where each of them has the quantum resistance $R_Q = 25812,807\ \Omega$. So an ideal CNT with ideal contacts has a resistance of about $6,5\ k\Omega$. Although this value is approached in real experiments even at room temperatures [30], in usual practice the measured values are higher than this theoretical bound. The two sources of the higher resistance are the "not so transparent" contacts and the previously mentioned scatterings within the tube. At higher temperatures the subbands don't interfere and the total resistance of a whole CNT device with its contacts can be written as:

$$R_{CNT} = R_{Contact} + R_{Tube} \tag{2.8}$$

The transparency of the contacts is determined by two types of barriers formed at the interface between the tube and contacting metal. First one is the cleanliness of the interface. Although nanotechnology has improved enormously within the last two decades, it is still very difficult two prevent so called *schmutz* between the tube and the metal. These are leftovers from the various chemical and physical treatments the device undergoes during its fabrication. The other type is the *Schottky Barrier*, which is formed due to the relative alignment of the Fermi level and the band gap of semiconducting tubes. If it falls in the middle of the gap then there are equal barriers for electrons and holes. Whereas when it aligns with the valence band then it forms a barrier only for electrons. This basic picture is supported by many experiments with different contact metals [31]. Metals like Pd and Au have a higher work function, which results in p-type contacts whereas metals with lower work functions like Al give better n-type contacts.

2.3.1 CNT Quantum Dots and Coulomb Blockade

Carbon nanotubes contacted in a field effect transistor configuration, show some typical transport behavior. This configuration is shown in a simplified manner in Fig. 2.9. It consists of a CNT with three metallic contacts. The gate contact is only capacitively coupled to the CNT whereas the source and drain contacts are directly connected. But due to the reasons mentioned previously tunnel barriers are formed at the interface to the CNT. This is represented in the figure by the gaps.

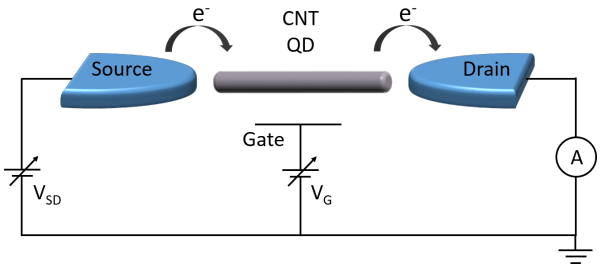

Figure 2.9: A schematical representation of a carbon-nanotube-quantum-dot. The gaps between the middle part (CNT-QD) and the source and drain electrodes represent the tunneling barrier which commonly arises because of lack of good wettability of the contacting metal or some impurities unintentionally built in during the production process.

The coupling of the leads to the CNT is defined in terms of the barrier strength $\Gamma_{S,D}$ and the capacitances C_S and C_D. At room temperature the thermal energy of the electrons is far higher than the barrier height. Depending on the response to the gate voltage one can distinguish three types of transport behavior at room temperature. The CNTs are either metallic with no response to the gate voltage, or semiconducting if the conduction is suppressed at either positive or negative gate voltages. The third kind shows an ambipolar behavior which is a high conductance at both positive and negative gate voltages but somewhere inbetween in a narrow region the conductance is suppressed. These are small bandgap semiconducting CNTs [32]. The width of this region is proportional to the gap in the band structure and its position depends on the doping level, which itself depends on the processing history.

At low temperatures quantum mechanical effects emerge and the CNTs behave under specific conditions as *quantum dots* (QD).

Whenever a carbon nanotube is weakly coupled to the contacts, actually a QD island is built. A QD is a small structure whose size is in all three spatial dimensions limited. This induces discrete energy states with ΔE level spacing for the electrons on the dot due to quantum confinement, like in the particle in a box problem. Therefore QDs are also called *artificial atoms*. Carbon nanotube devices fulfill this requirement and show at low temperature oscillating conductance peaks in their gate characteristic. The reason for this oscillation is the *Coulomb blockade* (CB). At low bias for some specific gate voltage there is a current flow observable but inbetween there are extended regions where the current is blocked. This is a result of the electrostatic repulsion of the electrons which are already on the island. It costs some amount of energy E_C to overcome this repulsion and to add one more electron onto the island. The charging energies for CNTs are typically in the range of $E_C = 5 - 20\, meV/L$, where L is length of the CNT in µm [29]. The charging energy is described by the classical total capacitance $C_T = C_S + C_D + C_G$ of the island and is given by:

$$E_C = \frac{e^2}{C_T} \tag{2.9}$$

CB can be observed when the coupling of the leads is sufficiently weak, this means that the tunneling resistance is substantially higher than the quantum resistance $R_T \gg R_Q = {}^{h}/_{e^2}$ and the thermal fluctuations are smaller than the charging energy $k_B T \ll E_C$ [33]. Under these circumstances transport happens via tunneling and this is possible whenever a state of the dot is aligned with the Fermi level of the contacts or states lie within the Fermi level window of both source and drain contacts. A

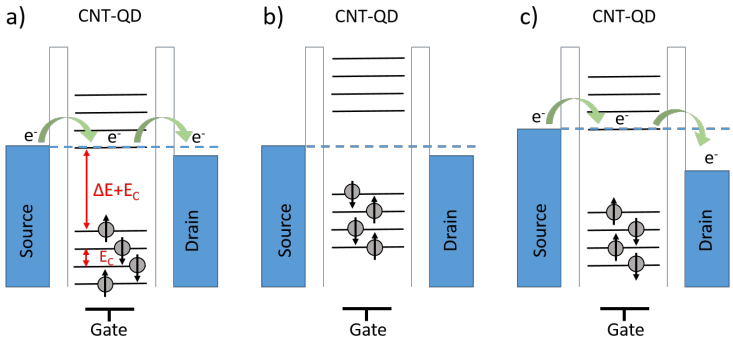

Figure 2.10: Schematic representation of the energy levels in an SWNT-QD at low temperatures in CB regime. Adapted from [33].

schematic description of this is given in Fig. 2.10a) and c) respectively. Otherwise the electrons are blocked to enter the dot, since all levels below the Fermi level are filled and the energy of the electrons is not enough to reach the next free state, this is represented in Fig. 2.10b). By changing the gate voltage the electrostatic potential of the dot is changed. This results in a shift of the energy levels and hence the states of a QD can be probed separately.

A SWNT-QD has a four fold degeneracy. This means that there are four different states with the same energy value. Therefore every energy eigenstate of the SWNT-QD can be occupied by four electrons, two because of the so called valley degeneracy and two because of the spin degeneracy. By changing the gate voltages these states can be moved with respect to the Fermi level of the contact. If one state is aligned with the Fermi level one electron can tunnel on and off the island, hence a current flow can be observed. To add the next electron one has to overcome the charging energy or shift the energy level by E_C. This

means that the energy levels of the four electrons are shifted. But the degeneracy is not lifted, because one can still not identify in which order the electrons enter the dot. If one level is filled by the four electrons to reach the next level one has to overcome the level spacing plus the charging energy $\Delta E + E_C$. Then again four electrons can be added.

The four-fold degeneracy can be observed in the transport behavior of clean, defect free tubes at low bias voltage [34]. A typical charge stability diagram is shown in the upper part of Fig. 2.11. Here the conductance is plotted as a gray scale plot against the bias and gate voltages. The white diamond shaped areas are the Coulomb blockade regions where the current is blocked. In this region the number of electrons on the QD is fixed. The lower part of the figure shows a single conductance measurement around zero bias voltage. It represents a cut through the diamond plot at $V_{SD} = 0V$.

Whenever a level of the QD is aligned with the Fermi level current can flow and hence a high conductance is observed. The four-fold degeneracy can be recognized here as the three small diamonds between the bigger diamonds. They correspond to the addition of single electrons to same QD eigenstate which are E_C apart and the addition of an electron to the next level $E_C + \Delta E$ respectively. The shape of the diamonds is asymmetric when the coupling of the source and drain contacts is asymmetric. The capacitances of the contacts can be calculated from the slopes of the diamonds $\beta = \frac{C_G}{C_S}$ and $\alpha = -\frac{C_G}{C_T - C_S}$ and coupling of the gate is given by the lever arm $\gamma = \frac{C_G}{C_T}$ [35].

If the level spacing ΔE between the electron eigenstates is smaller than the charging energy E_C the four fold symmetry in the stability diagram can not be observed. In this case the Coulomb diamonds have same sizes and the Coulomb peaks are

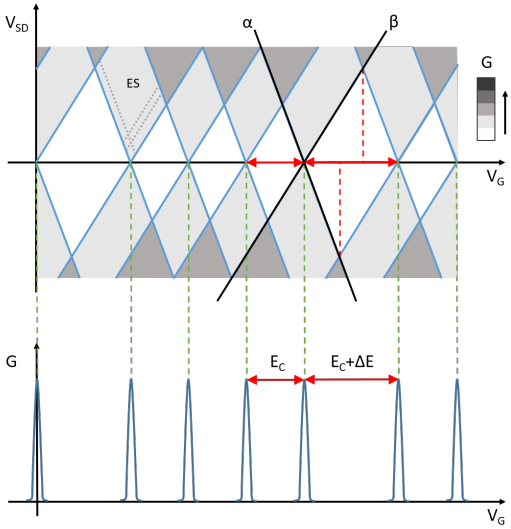

Figure 2.11: Charge stability diagram of SWNT-QD (top). The white diamonds correspond to regions where charge transport is suppressed due the Coulomb blockade. Corresponding CB oscillations at zero bias voltage (bottom) (adapted from [35]).

not grouped to four. But additional lines appear outside the blockade regions at higher bias voltages. This is also observed on CNT samples which are named as excited states (ES) [36]. Such lines are indicated on the diamond plot in Fig. 2.11 as dotted lines within the gray region marked as ES.

Chapter 3

Spintronics

3.1 Spin Degree of Freedom

Electrons do not only carry an electrical charge, they also have an intrinsic magnetic moment. We can imagine this magnetic moment as a result of the rotation of the electron around its own axis as depicted in Fig. 3.1. This imaginary rotation is called *spin*.

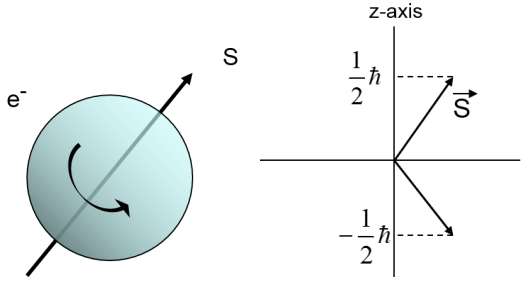

Figure 3.1: Imaginary rotation of an electron on the left and the two possible spin angular momentum values in a given direction on the right.

In the 1920s WOLFGANG PAULI suggested that a "fourth quantum number", which is "two-valued" would be needed to explain the magnetic effects of optical atomic spectra. In 1925 SAMUEL GOUDSMIT and GEORG UHLENBECK proposed the "intrinsic spin quantum number" $s = 1/2$ of the electron [37]. Often it is stressed that spin is a "purely quantum-mechanical phenomenon". If the electron is considered as a sphere with the classical electron radius $r_e = e^2/mc^2$, the velocity of a point at the equator would have to be ten times the velocity of light in order to produce a magnetic moment consistent with the experimental observations [38].

The magnetic moment of an electron rotating with angular momentum S is $\mu_s = -2\mu_B S/\hbar$, where μ_B is the Bohr magneton. The assumption of an intrinsic magnetic moment of the electrons does not only explain the atomic spectra but also the splitting of an atom beam in an inhomogeneous magnetic field, as observed in the Stern-Gerlach experiment.

3.2 Stern Gerlach Experiment

The experiment conducted by OTTO STERN and WALTHER GERLACH in 1922 in Frankfurt [39] reveals the quantum nature of the spin property. It was the first experiment to show that the spatial orientation of the magnetic moment is quantized. Therefore it became famous and was named after them as the Stern-Gerlach-Experiment.

The experimental setup is schematically shown on the left hand side of Fig. 3.2. In this experiment a beam of neutral silver atoms is sent perpendicularly through an inhomogeneous magnetic field. Unfortunately the experiment cannot be done with an electron beam since the Lorentz force acting on the charge

is much bigger than the force acting on the spin moment. The inhomogeneity in the magnetic field is generated through the shape of the pole shoes, which are formed like a blade and a furrow as the counter pole. The neutral silver atoms in the atomic beam have one unpaired electron in the outermost 5s shell. All other orbital angular and spin magnetic moments from the inner shells are compensated. So the experiment measures only the magnetic moment of the lone electron. Due to the magnetic moment the silver atom beam will be deflected in the inhomogeneous magnetic field. "Classically" seen, a magnetic moment can have any direction in space and statistically every direction should be present in the atomic beam equally. Therefore we would expect a vertical broadening of the beam. But the observed result is a splitting into two beams, as shown on the right hand side of Fig. 3.2.

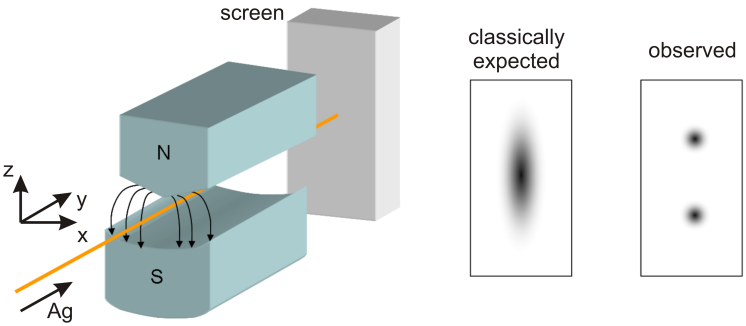

Figure 3.2: Schematical setup of the Stern-Gerlach experiment (left) and the expected vs. observed experimental results on the screen (right).

The splitting of the beam indicates quantization, where only the states "up" and "down" are allowed for the spin magnetic moment. Originally it was thought that the magnetic moment

of the s electron comes from the angular motion, but the later development of quantum mechanics tells us, that there is no angular momentum for s electrons, and that the Stern-Gerlach experiment measures the spin magnetic moment.

The spin magnetic moment is the origin of ferromagnetism which is used for long years in magnetic applications. On the other hand electrons are controlled in electronic applications by an electric field which is acting only on the charge property of the electron. The idea to jointly interact on the charge and the spin property and to control the one with the other and vice versa opened a new research area with many possibilities for new applications.

3.3 Datta-Das Transistor

In 1990 Supriyo Datta and Biswanjit Das proposed a new type of a field effect transistor [40]. Their idea was, unlike the previous ones, to modulate the spin state of the electrons in the conducting channel between the source and drain contact. As shown in Fig. 3.3 this transistor consists of two magentically parallel aligned ferromagnetic contacts (FM) connected to a quasi one dimensional conduction channel inside a semiconductor. On top of the channel a third electrode is placed, which acts as a gate electrode. Inside the semiconductor there is strong spin-orbit coupling causing an effective magnetic field which is indicated by the black arrows in Fig. 3.3. Due to their speed in the order of $10^6\, m/s$ the electrons experience, relativistically seen, the present electric field as an effective magnetic field. The effective magnetic field is perpendicular to the direction of movement of the electrons and also to the spin moment. This causes the spin moment, represented as the red arrows, to *precess* around the

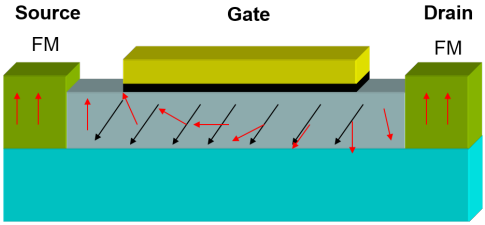

Figure 3.3: Schematic representation of the Datta-Das spin field effect transistor. Adapted from [42].

effective magnetic field. By applying an electric field on the gate electrode, the effective magnetic field can be changed and so the spin orientation of the electrons when they arrive at the drain contact. Depending on the relative orientation of the magnetization in the electrode and the spin orientation of the arriving electrons, they experience either a strong or weak scattering. The transistor is in the "on" state when they are aligned parallel and in the "off" state when they are antiparallel [41]. This new *spin field effect transistor* (spin-FET) presented the possibility how to alter the spin state by electrical means and therefore it is one of the important milestones in the development of the field of spintronics.

3.4 Spintronics

In applications the charge and spin property of electrons have been considered separately for a long time. Charges were manipulated by electrical fields, while the spin property was used in other technologies like magnetic recording, and here only through the magnetization of ferromagnets. The discovery of the *giant magnetoresistance* (GMR) (see. Sec. 4.2.2) opened a new way how to interact with the electron spin through the change of

magnetization. This initiated the development of a new field of research and technology, namely the *spintronics*, which is basically spin-based electronics. The advantage of spintronics over conventional electronics would be a very low energy consumption, higher data processing speed and increased density of transistors.

Conventional ferromagnetic metal thin-films are already used in spintronic devices as sensors like the GMR devices. Although they bring along many advantages like the high Curie temperatures, tunable magnetic anisotropy or well established production methods, they cannot be combined with semiconductors in a simple way. Due to the large resistance mismatch problem [43] the spin polarized currents cannot be efficiently transferred directly into the semiconductors. The aim to use the spin degree of freedom in semiconductor devices increased the importance of *dilute magnetic semiconductors* (DMS) in spintronics. DMS can actually combine the possibilities of semiconductor electronics with spin dependent effects. These materials are semiconductors which are slightly doped with rare earth or transition metals. Hideo Ohno was the first one to measure ferromagnetism in manganese doped gallium arsenide (GaMnAs) [44]. The ferromagnetism in DMS arises from the antiferromagnetic coupling between the Mn ions and the hole carriers, which mediate between the Mn ions and cause a ferromagnetic interaction between the Mn spins. For most of these materials the Curie temperature lies quite below room temperature, which makes a widespread application difficult. For reviews see [45][46].

For further development important issues like the injection of spin polarized current into semiconductors, efficient control of the spin orientation, preservation of the spin polarization over longer distances and the detection of spin polarized currents have

to be solved. An important issue which makes spintronics interesting is that in systems with pure spin currents Joule heating would be reduced largely for the spintronic operations[47].

3.5 Spin Relaxation

Spin polarization in nonmagnetic materials occurs via optical methods or via spin injection, which is basically transferring spin polarized electrons from a ferromagnet into the nonmagnetic material. The magnitude of spin is a conserved quantity but not its orientation. Therefore the imbalance in the "spin-up" and "spin-down" population in nonmagnetic materials has the tendency to equalize with time and distance away from the junction. Whereas the non-equilibrium accumulation near the FM/NM interface is at a similar high value as in the ferromagnet it decays exponentially with the distance away from the junction. This equalization happens via *spin relaxation* processes. The distance over which the spin polarization is preserved is called *spin diffusion length* l_{sd} and can be estimated by the following relationship [48]:

$$l_{sd} = \sqrt{\frac{\nu_F \tau_{\uparrow\downarrow} l_m}{3}} \tag{3.1}$$

where ν_F is the Fermi velocity, $\tau_{\uparrow\downarrow}$ is the spin flip time and l_m is the mean free path. If the spin relaxes too fast the distance that spin polarized currents can travel will be too short, which makes it difficult for practical applications.

Aside from scattering by magnetic impurities, spin relaxation happens mainly through spin-orbit coupling and hyperfine coupling to the nuclear spin. The spin-orbit coupling is a relativistic effect. It occurs whenever a particle with non zero spin moves

at a relativistic speed in an electric field. This relative motion results in an effective magnetic field. If we look at the case of an electron orbiting around the nucleus from the electrons rest frame then the nucleus with the charge Ze is actually orbiting around the electron. This motion is coupled with an angular momentum and hence with a magnetic field $\vec{B}_{orb}$ at the center of the orbit where the electron is located. The spin magnetic moment μ_s of the electron interacts with this magnetic field. The spin-orbit coupling energy can be given as: $E_{SO} = -\vec{\mu_s} \cdot \vec{B}_{orb}$ [49]. Therefore to minimize this energy the spin moment tends to orient parallel with the effective magnetic field. This interaction is for example also the reason of the magneto crystalline anisotropy, which is described in Sec. 4.1.1. Spin-orbit coupling increases with the atomic number Z, therefore in organic materials with low atomic numbers the spin-orbit coupling is small and hence these materials are better suited for spintronic applications.

There are three different mechanisms how spin-orbit coupling results in spin relaxation. The Elliot-Yafet mechanism decribes how momentum scattering is causing spin-flip. The Dyakonov-Perel mechanism is responsible for spin relaxation in solids without a center of symmetry. And the Bir-Aronov-Pikus mechanism describes spin relaxation by the exchange interaction between electrons and holes. For a detailed discussion see [50].

3.6 Spin Measurements on CNT

The first generation of spintronic devices was based on metallic thin films as they are used in GMR or TMR structures. In these metallic systems the carrier velocities are very large but the spin relaxation time τ_s is very small. Therefore device dimensions are in the range of a few nanometers in order to observe spin

dependent effects.

The wish to control the spin degree of freedom by electrical means and the knowledge on dilute magnetic semiconductors led to the second generation of spintronic devices, namely the semiconductor spintronic systems, like the aforementioned DMS (see Sec. 3.4). Here the main problem is the efficient injection of spin polarized currents which is mainly caused also by the conductivity mismatch problem. Therefore the search for solutions to preserve the spin polarization over longer time and space distances became important. This led the attention to systems with low spin-orbit interaction. After 1999 when spintronic experiments on carbon nanotubes were done molecular spintronics started, which is the third important field of spintronics. Herein the materials to study spin injection, spin accumulation and spin control are molecular structures, where the carbonaceous materials like carbon nanotubes or graphene represent an important part. The reason for this is the low spin-orbit interaction in materials with small atomic number. The spin-orbit interaction scales with Z^4. The first experiments were done by Tsukoagoshi et al. on MWNT with Co contacts [51]. The schematic device structure with a SEM image of the actual device can be seen on the left hand side of Fig. 3.4. Tsukagoshi et al. were able to see hysteretic behaviour in the differential resistance during the change of an applied magnetic field at 4.2 K. The device structure in Fig. 3.4 is also the basis of the experiment carried out in this thesis and the details will be discussed in Section 5.2 and 5.4. Some of their measurement results [51] can be seen on the right hand side of Fig. 3.4. The reported magneto resistance (MR) ratios were in the range of 2 - 9 %.

Other groups also reported on MWNT spin valve devices with Co [52] or PdNi [53] contacts. The observed MR ratios

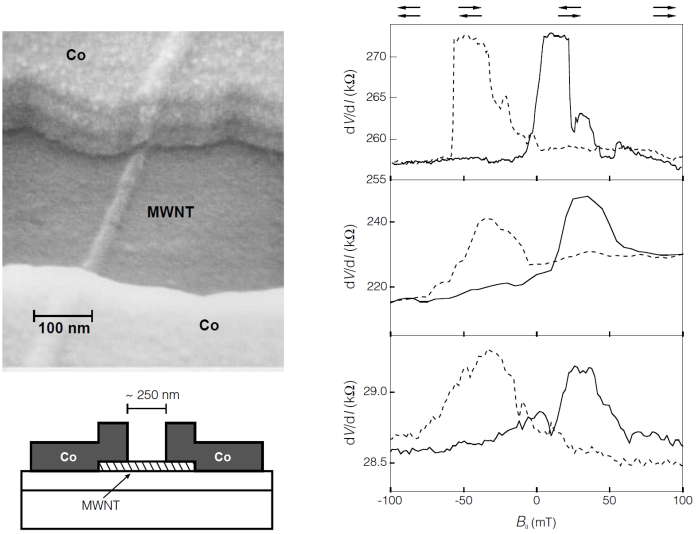

Figure 3.4: SEM Image of a MWNT spin valve device contacted with Co contacts on the left and differential resistance of three MWNT devices on the right. The arrows show the relative magnetic orientation of the contacts during the measurement [51].

were in the range of 1 - 2 %. Highest MR ratios observed with Co contacted CNTs were about 30% [54]. In later experiments, instead of ferromagnetic metals the contacts were realized by $La_{2/3}Sr_{1/3}MnO_3$ (LSMO) which is a semi-metal. In these materials the sub bands for the different spin orientation are shifted so much that at the Fermi level there are only states available in one sub band, which leads to 100 % spin polarization. Hueso et al. observed in spin valve devices, where MWNT were contacted with LSMO, an MR ratio of up to 61 % [55].

In contrast to MWNT, the SWNT could be a more interesting candidate to study spin dependent transport phenomena. In SWNTs there would be no spurious effects which would arise

from different nanotube shells as in the case of MWNTs. Also the band structures of SWNTs are well defined. Therefore SWNTs would show a ballistic spin transport behavior. First experiments with SWNT were done by Kim et al. with Co contacts. They report an MR ratio of 3.4 % at 0.2 K [56]. In later experiments with highly transparent PdNi contacts Sahoo et al. observed an oscillating behavior of the MR between -7 % and +17% with changing gate voltage [57]. The highest observed MR ratios were with GaMnAs contacts 75% [58] and with Fe contacts 100% [59] both measured at 0.3K.

Chapter 4

Magnetoresistance

As already mentioned during the introduction the aim of this work is to study spin dependent transport effects in CNT with ferromagnetic contacts. To understand how spin polarization in ferromagnetic materials occurs we have to gain some more insight how the coupling between the spins is causing different types of magnetic behavior and how spin polarization can be detected by electrical means. Therefore an introduction to magnetic materials and magnetoresistive effects is given in this chapter.

4.1 Magnetism

There are several different ways to produce a spin polarized current. To polarize the current means to achieve an imbalance in the population of electrons with different spin orientation. In addition to the optical methods, where for instance semiconductors are illuminated by circularly polarized light, there is also the possibility to pass the current through a ferromagnetic material [50]. In this work the main concept was to use ferromagnetic

metals attached as contacts to both ends of a carbon nanotube. In this way one of the contacts acts as a spin polarizer and can inject the polarized current into the carbon nanotube whereas the other one acts as an analyzer in analogy to the optical polarization experiments. To understand the effect of a ferromagnet on electrons we should first have a look on different magnetic materials.

In common belief all materials, which seem not to be affected by a magnetic field, are nonmagnetic. But in some sense all materials, although the effect might be very small, are magnetized by an applied external magnetic field. The reason for this behavior is either the orbital motion of the electrons, the magnetic moment associated with the electron spin or the combination of both. In this general discussion the nuclear spin will not be taken into account, since its magnitude compared to the electronic moments is more than three orders of magnitude smaller [49]. The materials where the effect is small but can still be detected macroscopically are the so called dia-, para- and antiferromagnetic materials. After inserting a material into a magnetic field the material gets magnetized. The emerging *magnetic flux density* $\vec{B}$ is the sum of the applied external *magnetic field intensity* $\vec{H}$ and the occurring *magnetization* $\vec{M}$. This is in the cgs system given as:

$$\vec{B} = \vec{H} + 4\pi\vec{M} \tag{4.1}$$

Every material reacts to an applied magnetic field with a different intensity. A quantity to describe magnetic material behavior is the *susceptibility* χ. It is the ratio of the magnetization to the field intensity and hence dimensionless. The magnetic susceptibility is for dia- and under some circumstances for paramagnetic materials independent of $\vec{H}$. For applications of ferro- and ferri-

magnetic materials the $\vec{B}$ field is of more importance, therefore the ratio of the flux density to the field intensity, namely the *permeability* μ is of more interest.

$$\chi = \frac{M}{H} \quad ; \quad \mu = \frac{B}{H} \tag{4.2}$$

Materials are not only classified according to the sign and magnitude of χ or μ but also according to the change of these with temperature and the field intensity. An overview is given in the table 4.1.

Table 4.1: Overview on different magnetic materials (from several textbooks).

Magnetic material	Susceptibility χ	M-H dependence	$1/\chi$ dependence on Temp.
Dia-	-10^{-5}	negative linear	no dependence
Para-	$+10^{-5}$– $+10^{-3}$	positive linear	linear
Antiferro-	low		below Neel Temp. decreasing, linear above
Ferri-	low	hysteretic	above T_C linear
Ferro	high	hysteretic	above T_C linear

Diamagnetism

Materials like Cu, Bi, pyrolitic graphite or water have a small, negative susceptibility χ in the order of 10^{-5} [60]. This means that they react to an applied field in an opposite way such that they are repelled from the applied magnetic field. In such materials there are no unpaired electrons and the only magnetism arises, classically seen, by the induced orbital motion of the electrons around the nucleus. From Lenz´s law we know that such

induced currents generate a magnetic field, which is always opposing the generating field. It is similar to the force acting on a piece of a permanent magnet when it is moved towards a conductive circular ring. In the case of the permanent magnet the acting force vanishes when the magnet is not moving any more, but in the case of a diamagnet the force does not vanish. This is also how magnetic levitation with pyrolitic graphite or water droplets works [61]. Diamagnetism is difficult to observe since it is easily hidden by magnetic atomic impurities.

Paramagnetism

In contrast to diamagnetic materials, paramagnets have already an existing magnetic moment. In the absence of an external field they are randomly oriented. This moment originates from the orbital motion and from the spin of the electrons. Typical paramagnets are Pt, Pd, Na or O. They are magnetized in parallel direction with the applied field, so that they are attracted towards the magnet. Their susceptibility is also small in the order of 10^{-3}-10^{-5} but positive. Due to their different electronic configuration their moments are randomly oriented. Unlike for diamagnetic materials there is a temperature dependence of the susceptibility. Its reciprocal increases linearly with temperature which is described by the *Curie law*.

Antiferromagnetism

In this class of magnetic materials the individual magnetic moments are antiparallelly oriented so that the net magnetization is zero. This arrangement of the moments is due to the interaction of neighboring atoms, which is also called the negative exchange interaction. Above the so called *Neel temperature* antiferromagnets show typical paramagnetic behavior and similarly they have

a small susceptibility. Below this temperature the spins are oriented in an antiparallel way and have a vanishing magnetization. Some examples would be Cr, FeMn or NiO.

Ferrimagnetism

Ferrimagnetic materials have, like antiferromagnets, antiparallel oriented spins on different sublatices. But in this case their magnitude is not equal and hence there is a net spontaneous magnetization in one of the directions. Below the Curie temperature they behave like ferromagnets. Since these materials have higher susceptibilities and show similar behavior on the M-H curve, are they comparable to ferromagnets.

4.1.1 Ferromagnetism

The interaction of ferromagnets with a magnetic field can easily be observed. Therefore they were considered as the only magnetic material for long time. Their susceptibility is several orders of magnitude higher compared to other materials. The magnetization in ferromagnets originates from the spin moment of the unpaired electrons. These moments are ordered parallelly by the so called *exchange interaction*. The sum over all the parallel moments gives rise to a high magnetization which is several orders of magnitude higher than in the other forms of magnetism. This ordering cannot be understood classically, it is the consequence of Pauli-Exclusion Principle and the Coulomb interaction of the electrons [49]. It can be imagined as an hypothetical *molecular magnetic field* orienting the spins in parallel. This imaginary field is about 1000 times stronger than the dipolar field of the spin moments. But this interaction is a rather short range interaction. It falls off exponentially with the distance whereas the dipolar interaction decays with the inverse third power of

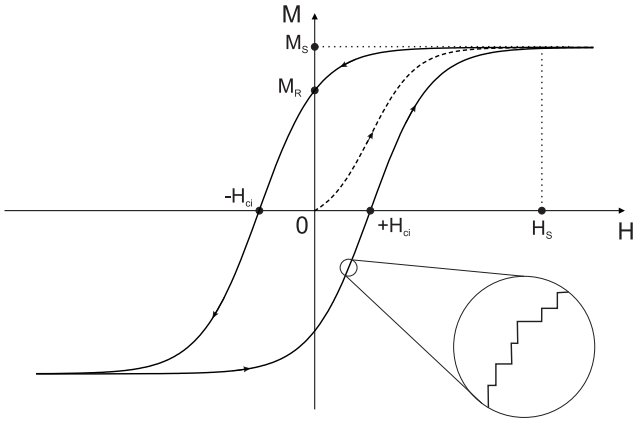

Figure 4.1: Magnetic hysteresis curve of a ferromagnet. Inset on the right shows the Barkhausen Effect.

the distance. The long range ordering phenomena due to the exchange interaction is a result of the chain reaction of neighboring spins. The exchange energy can be expressed according to the Heisenberg model as [62]:

$$E_{ex} = -2J_{ex}\vec{S}_i\vec{S}_j = -2JS_iS_jcos\phi \tag{4.3}$$

where J_{ex} is the exchange integral, S_i and S_j the spin angular momentum and ϕ is the angle between the spins. Hence the exchange energy is minimum when the spins are parallel. Above the so called *Curie temperature* T_C thermal agitation overcomes this ordering and causes a paramagnetic behavior.

The magnetization below T_C is not linear with respect to applied magnetic field and it is additionally depending on the magnetic history. It has a hysteretic behavior (see Fig. 4.1) which is peculiar to ferromagnets. Macroscopically seen, a piece of a ferromagnet initially has no net magnetization. As soon as an

increasing $\vec{H}$ field is applied the magnetization starts to increase. This is the initial magnetization and is described by the dashed curve in Fig. 4.1. After further increase of the applied magnetic field the magnetization reaches a saturation value M_S. This is the situation when all spin moments are aligned parallel to the field. When the magnetic field starts to decrease the magnetization does not follow the initial curve but follows the solid line in Fig. 4.1. When the applied field is decreased to zero the material will still remain magnetized. This is the value at which the curve crosses the y-axis and it is called the *remanent* magnetization M_R. By further decreasing the applied magnetic field the magnetization can be switched to the opposite orientation. The value at which this happens is the *intrinsic coercivity* H_{Ci}. This is slightly different then the *coercivity* H_C which corresponds to the magnetic field that is required to decrease the flux density B to zero [62]. Once a ferromagnet experiences a magnetic field its magnetization will follow the hysteresis curve while the applied magnetic field is varried between the $\pm H_S$ values. Depending on the point where the field is stopped the material will stay magnetized at some finite value. A ferromagnet can again be demagnetized either by increasing the temperature above the Curie temperature and then cooling down in the absence of a magnetic field or by applying an alternating $\pm H$ field where the amplitude of the field is slowly decreasing. In this way the total magnetization will be decreased slowly until it reaches zero.

Domain Structure

In ferromagnets, due to the parallel orientation of the spins, one would expect to observe the saturation magnetization. But for "unmagnetized" macroscopic samples the measured magnetization is much smaller than this value. This is the case for single

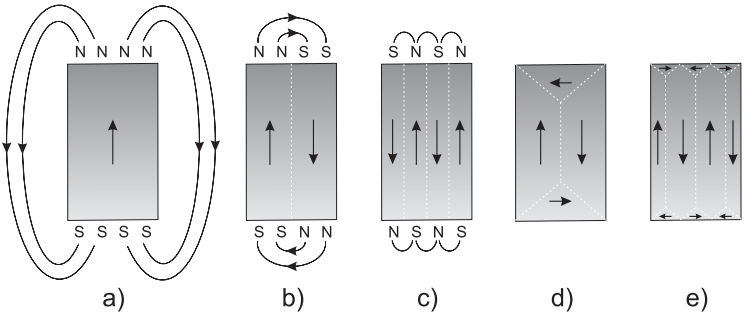

Figure 4.2: Formation of domains, the high stray field is reduced from a) to d) by the formation of domains. d) and e) are so called closure domain structures, where all the field is compensated inside material (adapted from[64]).

crystal as well as in polycrystal samples. The reason for this are the so called *domains* or *Weiss-Regions* named after Pierre Ernest Weiss, who first suggested their existence [63]. The magnetization of a single domain is always saturated but its orientation can vary. Different domains can be oriented in an opposite way so that their magnetization cancels. The reason for building up domains is to reduce the magnetostatic energy due to the demagnetizing filed. This is described in Fig. 4.2. A high stray magnetic field forms around a single domain (see Fig. 4.2a)). This field is reduced as shown in Fig. 4.2b) and c) by the formation of antiparallel domains. The stray field can even be almost canceled by the formation of so called *closure domains* as shown in Fig. 4.2 d) and e), where the orientation of the magnetization in neighboring domains forms closed loops inside the material.

In order to minimize the energy further, one would expect the formation of infinitely many small domains, which is actually not the case. It is even observed that in bigger samples the

tendency is to build bigger domains. The reason for this is that at the boundaries from one domain to another, spins with opposite orientation come very close to each other. At such small scales the exchange energy is much higher than the magnetostatic energy. To build domains costs also energy. Therefore the domain structure is a tradeoff between these energies [64].

Another important factor is the width of these domain walls. To build an abrupt change from one orientation in one domain to the opposite direction in the neighboring domain, would be highly energy-intensive, since the strong exchange interaction wants to align them parallel. Whereas a gradual change over many spin layers, where each of them is rotated by only a few degrees with respect to the previous one, reduces the exchange energy (see Eq. 4.3). This would on the other side imply that domain walls with infinite width would build-up. But that is also not the case. The reason for this is the so called magnetic anisotropy. This means that there are preferential orientations in solids for the orientation of the magnetization which is mainly given by the crystal structure of the material. Usually the magnetic moments tend to orient along the main crystal directions. This is caused by the so called *spin-orbit coupling*. Without this coupling there wouldn´t be preferential directions for the magnetization like the easy or hard axis in magnetic materials. The orientation of most of the magnetic moments within a domain wall are different from the easy axes. Therefore to build thick domain walls is also highly energy consumptive. The formation of domains inside magnetic materials is a complicated balance of the dipolar-, exchange- and spin-orbit coupling [65].

When a magnetic field is applied to a ferromagnetic material, at first these mentioned domain walls start to move and increase the volume of the parallel oriented domains. This is a reversible

process at small magnitudes of the applied field. As soon as the walls come across some irregularities in the crystal which act as pinning sites they stick. At higher magnetic fields they cross these hurdles abruptly as shown as irregular steps in the inset of Fig. 4.1, which can even be observed as a noise effect by a pick up coil. It is the so called *magnetic Barkausen noise* observed in 1919 by HEINRICH BARKHAUSEN [66]. These changes are not reversible and are the reason for the hysteretic behavior in ferromagnets [65]. There are also several other methods to observe the domain structure directly. They can be detected by different means like the Bitter method where magnetic colloidal particles are attracted towards the domain walls or the optical Kerr method where the polarization of a light beam is altered during the reflection from a magnetized surface. Further methods would be electron microscopy (TEM) or magnetic force microscopy (MFM) methods [67]. In this work the MFM method is applied to gain insight into the domain structure of the contacts used in the fabricated devices.

Magnetic Anisotropy

As mentioned earlier, there are preferential directions for the magnetization in magnetic materials. These are the so called *easy axes*, other crystallographic directions which are avoided are the *hard axis*. The energy needed to turn the magnetization from an easy axis to a hard axis is the anisotropy energy. The main reasons for this preference are the magnetocrystalline anisotropy, the form anisotropy and the induced anisotropy. The magnetocrystalline anisotropy is a result of the spin-orbit coupling. For elements with not fully filled shells the charge distribution is rather spheroidal then spherical. Therefore the orbital moments have a preferential direction and through the spin-orbit

coupling also the spin moments. For example iron has a body centered cubic structure where the easy axes are in the directions of the cube edges whereas in nickel the $\langle 111 \rangle$ and in cobalt the hexagonal axis perpendicular to the basal plane is the easy axis. Form anisotropy is depending on the shape of the specimen and is more relevant for small sizes. It derives from the demagnetizing field which itself is given by the shape (see Fig. 4.2). For a sphere it would be zero since there is no given specific direction but for a thin film the easy axes would be in the plane of the film. Induced anisotropy is a result of elastic strain or the coupling of nearby layers of magnetic materials. So the only intrinsic anisotropy is the magnetocrystalline, all others are artificial anisotropies.

4.1.2 DOS Splitting, Band Magnetism

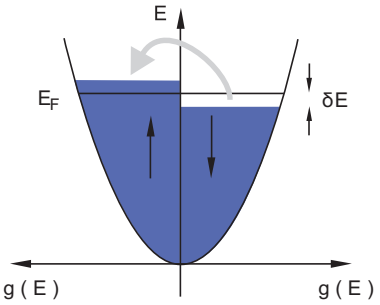

Figure 4.3: Density of states for spontaneous spin splitting subband.

The best known ferromagnets Fe, Co, and Ni show in experiments at low temperature non-integer atomic moment values like 2.22 μ_B, 1.72 μ_B and 0.61 μ_B, respectively. The *Bohr-Magneton* μ_B is the value of the magnetic moment of a spin or the magnetic moment due to the orbital motion of an electron in the

first Bohr orbit and therefore a fundamental quantity. Since ferromagnetism occurs due to the spin moment of the electrons one would expect to measure values around integer multiples of μ_B per atom. But that is obviously not the case. This problem was solved by the application of the band theory to magnetic materials, which is also called the *itinerant ferromagnetism*. Itinerant, because it takes into account the non localized conduction electrons in metals. Between 1933 and 1936 E.C. STONER and N.F. MOTT in UK and J.C. SLATER in US were the first ones to apply this theory to magnetism [62]. Due to the exchange interaction a parallel orientation of the spins is preferred. Therefore it is assumed that some electrons, lets say from the spin-down sub-band, are shifted to the spin-up sub-band which is shown in Fig. 4.3 by the gray shaded arrow. The number electrons which are shifted would then be $\delta N = g\left(E_F\right)\delta E/2$ where $g(E_F)$ is the density of states at the Fermi level and δE is the energy increase. This would mean that their kinetic energy is increased by:

$$\Delta E_K = \frac{1}{2}\, g(E_F)\,(\delta E)^2 \tag{4.4}$$

but an energy increase is not favorable. This could be compensated by the interaction with the molecular field. The potential energy in the molecular field is given by:

$$\Delta E_P = -\frac{1}{2}\, U\,(g(E_F)\,\delta E)^2 \tag{4.5}$$

where U is a measure of the molecular field or the exchange interaction, which itself is related to the Coulomb interaction. Now we can obtain the total energy by adding Eq. 4.4 and Eq. 4.5:

$$\Delta E = \Delta E_K + \Delta E_P = \frac{1}{2}\, g(E_F)\,(\delta E)^2\,(1 - U\, g(E_F)) \tag{4.6}$$

from this we can see that the total energy change ΔE can be negative if the requirement

$$U\, g(E_F) \geq 1 \tag{4.7}$$

is fulfilled. This is the so called *Stoner criterion* [68]. This means that in this case for the electron gas it is favorable to change the spin orientation and reduce hereby the energy. The result is spontaneous ferromagnetism which occurs in the absence of an external applied magnetic field. As we can see from the inequality Eq. 4.7 the Stoner criterion is fulfilled, if we have a high density of states at the Fermi level and/or if we have a high correlation parameter U. In Fig. 4.4 the Stoner factor for some elements up to atomic number 49 are listed. We can see that the condition is fulfilled for the well known ferromagnets Fe, Co and Ni. One can also recognize that Ca, Sc and Pd are very close to spontaneous ferromagnetism. This could be verified by experiments where by adding $0,15\,\%$ iron into palladium the alloy showed ferromagnetic behavior [69].

The splitting of the density of states into spin sub-bands for nickel is shown in Fig. 4.4b). The non-integer atomic magnetization is a result of a non integer occupation of the sub bands.

Conventionally the spin states with the larger number of electrons are called the majority spins. As shown in Fig. 4.4b) most of the states of the spin-up sub-band which lie below the Fermi level E_F, are filled (dark shaded area) whereas in the spin-down sub-band there are quite many unoccupied hole states above E_F (light shaded area). Therefore in this representation spin-up would be the majority. We should take into account that the magnetic moment is defined as $\vec{m} = -g\mu_B\vec{s}$ and therefore the spin and the associated momentum have opposite directions. By

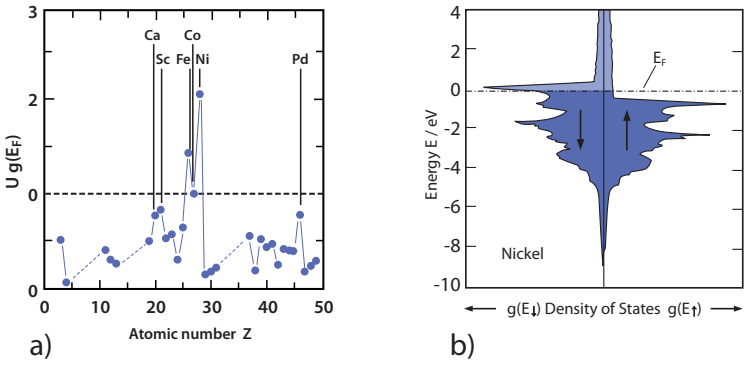

Figure 4.4: a) Stoner criterion value up to atomic number 49 b) Spin-splitting in the DOS of Ni (adapted from [70] [71]).

the shift of the sub-bands there occurs an imbalance in the number of available states around the Fermi level. There are more full and empty states for the minority spin direction at this level and we know that only the states around the Fermi level contribute to transport. So actually the minority spins are the responsible ones for the spin polarized transport [72].

4.2 Magnetoresistance

Magnetoresistance (MR) is the change in the electrical resistance of a material, when a magnetic field is applied. It is usually defined by the ratio of the change ΔR to the initial value $R(0)$.

$$MR = \frac{R(H) - R(0)}{R(0)} \tag{4.8}$$

The **ordinary magnetoresistance** occurs in all metals and it is positive, in contrast to other negative magnetoresistive effects in ferromagnetic metals. The magnetic field forces the electrons to a cyclotron motion, which is the reason for shorter mean free

paths and this results in an increase of the resistance. It scales for low magnetic fields with B^2 and is around 1 % at 1 T [73].

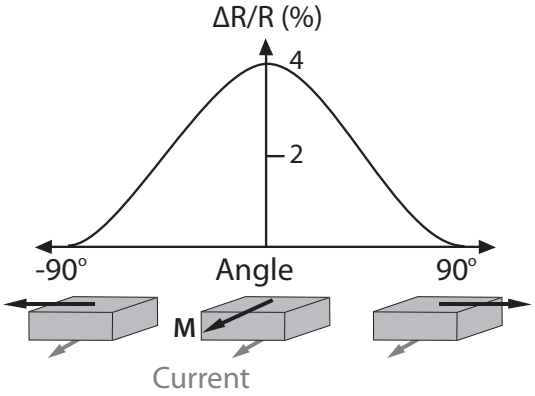

Figure 4.5: Anisotropic magnetoresistance, the resistance change is maximum when the magnetic field is parallel to the current flow (adapted from [72])

In 1856 William Thomson (later known also as Lord Kelvin) observed that the resistance of iron increases by 0.2 % when the applied magnetic field was parallel to direction of the current flow and decreases by 0.4 % when the directions are perpendicular to each other. This effect is known as the ***anisotropic magneto resistance*** **(AMR)**. Its magnitude can be, depending on the used material, up to a few percent (see Fig. 4.5). AMR originates from spin-orbit coupling [72]. Since a few millitesla are enough to achieve this change in resistance, AMR sensors were mainly used in the read heads of magnetic recording discs until the early 1990s, when larger resistive effects were discovered, which will be discussed in the following.

4.2.1 Two-Current Model

The two-current model was suggested by N. F. MOTT [74] and describes the conduction mechanism in ferromagnetic 3d-metals. In transition ferromagnets the 4s- and 3d-states are hybridized and exist both at the Fermi level. The conduction is mainly based on the 4s-electrons because of their higher mobility. The 3d-electrons are inefficient due to their higher effective mass and hence have a low mobility, $\mu_e = \frac{e\tau}{m^*}$. Although the 3d-ferromagnets compared to copper have a higher DOS at the Fermi level, they have a lower conductivity (see Table 4.2). This can be explained by the two-current model. The higher resistivity occurs due to the scattering of the 4s- minority spin-up electrons into the 3d-spin-up empty states. The more empty states are available, the higher is the scattering probability.

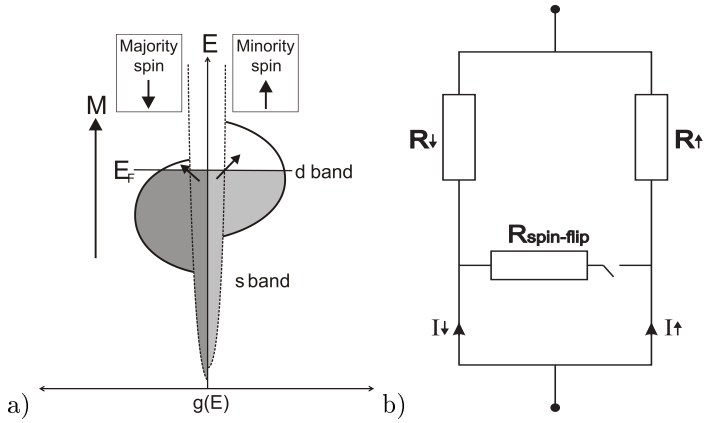

Figure 4.6: Spin selective scattering in the two-current-model (adapted from [72]).

The main assumption in this model is that there is no spin-flip scattering. This means that spin-up electrons scatter only into spin-up empty states and likewise for the spin-down elec-

trons (see Fig. 4.6a)). Conduction is normally a diffusive process, where the electrons are scattered by different obstacles. Actually they undergo many elastic collisions before an inelastic spin-flip scattering happens. Inelastic scattering, where energy is lost or gained, happens for example at collisions with magnons. Magnons are quantized oscillations of spin waves and appear much less well below T_C. They happen in the order of 100 times less than other scattering occasions. Therefore spin-flip can be neglected. If we now consider a strong ferromagnet, all the majority spin states are occupied, the 4s- minority spin-up states can scatter into the 3d- hole states. Due to the high density of empty 3d-states also more scattering can occur and that is the reason for the lower conductivity. For copper, all 3d-states are occupied and lie below the Fermi energy, therefore they are not available for scattering. This is the reason of the high conductivity of copper.

In this model, where spin-flip is not taken into account, the conduction takes place in two independent channels with different conductivities. This was verified, for example, with experiments on nickel with different impurities, consistent with models for the electronic structures of these impurities [75]. The two current conduction can be imagined like in Fig. 4.6b). Therefore the conductivities can be added in series $\sigma = \sigma_\uparrow + \sigma_\downarrow$ or the resistivities in parallel [73],

$$\varrho = \frac{\varrho_\uparrow \cdot \varrho_\downarrow}{\varrho_\uparrow + \varrho_\downarrow} \tag{4.9}$$

The overall conductivity of the metal is always larger than of the individual spin channel and double for paramagnets where $\sigma_\uparrow = \sigma_\downarrow$. The ratio of the conductivities of both channels is defined as $\alpha = {}^{\sigma_\uparrow}/_{\sigma_\downarrow} = {}^{\varrho_\downarrow}/_{\varrho_\uparrow}$. The resistivities for some metals

and their spin channels are given in Table 4.2.

Table 4.2: Spin dependent and overall resistivities of some 3d-transition metals and copper for comparison in $\left[10^{-8}\,\Omega m\right]$ [73].

Metal	Orbital	Magnetization	$\varrho_\uparrow$	$\varrho_\downarrow$	ϱ	α
Cu	4s-	paramagnetic	4	4	2	1
Ni	3d-	ferromagnetic	13	65	11	5
Co	3d-	ferromagnetic	8	120	15	15
Fe	3d-	ferromagnetic	32	28	15	0.9

A more detailed description, where also spin-flip scattering is taken into account was developed later by Campell and Fert [76].

4.2.2 Giant Magnetoresistance GMR

In 1988 two independent research groups, the one of Albert Fert in Paris and the one of Peter Grünberg in Jülich reported about a new type of magnetoresistance [6, 7]. They had observed an important change of the electrical resistance in thin-film multilayer structures, which consist of magnetic layers separated by nonmagnetic layers. The thicknesses of the layers are in the range of a few nanometers. The magnitude of this effect was some ten percent. This was about an order of magnitude higher than the till then known AMR. Therefore it was given the name *giant magnetoresistance* (GMR) and it attracted much attention, particularly with regard to data storage and magnetic recording. In Fig. 4.7 the results of the original measurements are shown, where one can see the decrease of the relative resistance with increasing magnetic field. Whereas in Fig. 4.7a) the measurement was carried out on a trilayer at room temperature, in Fig. 4.7b) stacks of up to 60 layers were used at low temperature (4.2 K). In these experiments it was shown that the spin

moment of the electrons played an important role in the transport of electric charge. This was an important discovery, which started a whole new research area namely "*spin electronics*". For their efforts Albert Fert and Peter Grünberg were rewarded in 2007 with the Nobel Prize in Physics.

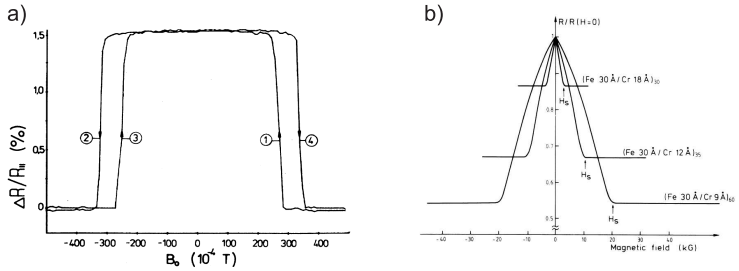

Figure 4.7: Original GMR measurements made by Grünberg and Fert [7, 6]

The GMR effect can be explained with the help of the previously mentioned two-current model. Lets consider a trilayer GMR structure like the one sketched in Fig. 4.8. As in the two-current model, the spin-up and spin-down currents can be assumed to flow on independent paths. In the lower part of Fig. 4.8a) the situation for antiparallel magnetization of the two ferromagnetic layers is shown. This is the case in the absence of an external magnetic field. The thickness of the separating NM layer is chosen so that the spontaneous orientation of the magnetization in the neighboring FM layers is antiferromagnetic. This is known as the interlayer exchange coupling, where the magnetic coupling between neighboring layer oscillates between ferromagnetic (parallel) and antiferromagnetic (antiparallel) depending on the thickness of the metallic nonmagnetic separation layer [77]. In the case of antiparallel orientation, as shown in Figure 4.8a), both spin channels experience similar scattering, the spin-

down channel more in FM1 and the spin-up more in FM2. The scattering events are depicted as stars on the sketched paths of the electrons. This is shown in the lower part of the circuit diagram (see Fig. 4.8b) by one small and one large resistor in each spin channel. When the externally applied magnetic field is increased the magnetization on both sides becomes parallel, which is depicted in the upper part of Fig. 4.8. In this case the resistivity of one channel increases, represented by two large resistances for the spin-down channel. But for the spin-up channel the electrons can pass the layered structure almost without scattering, as shown in the circuit by two small resistors. Since both channels are parallel the path with the lower resistance determines the total resistance. This is the reason for the extraordinary decrease. The GMR ratio is defined as:

$$GMR = \frac{\Delta R}{R} = \frac{R_{AP} - R_P}{R_P} \tag{4.10}$$

where R_{AP} corresponds to resistance of the structure when the FM layers are antiparallel oriented and R_P when they are parallel.

The scattering at the interfaces between FM and NM layers is also spin dependent [78]. Therefore they are added to the spin dependent scattering in the bulk and enhance so the effect. The resistance of the nonmagnetic layer is not included into the circuit diagram, since it has almost no dependence on the magnetic field and its value is low compared to the resistances of the interfaces and the bulk.

The schematics in Fig. 4.8 shows a GMR structure in the so called current perpendicular to the plane (CPP) configuration, where the current flows from one ferromagnet passing the nonmagnetic layer and then through the next ferromagnetic layer.

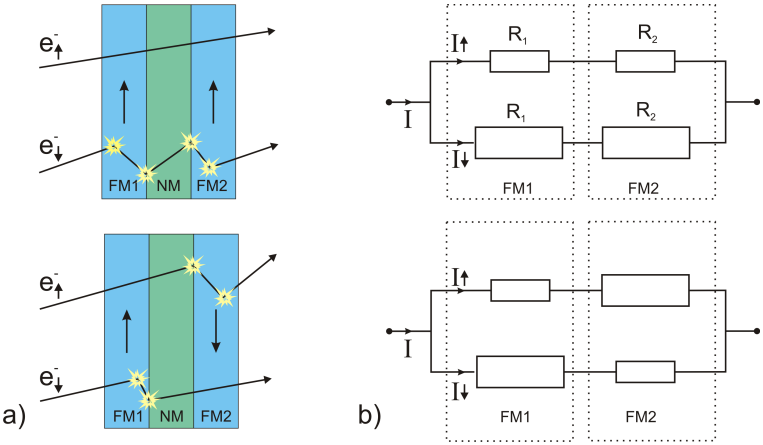

Figure 4.8: a) Schematic GMR structure consisting of ferromagnetic (FM) and nonmagnetic (NM) trilayer. Stars on the paths of electrons represent scattering events. b) Electrical equivalent circuit diagram for the two possible states parallel (upper part) and antiparallel (lower part) (adapted from[79]).

The earlier measurements were done in a configuration where the current was flowing parallel to planes. This is the current in plane (CIP) configuration. The magnitude of the GMR effect is higher in the CPP configuration, since the absolute resistance of CPP is much higher compared to CIP, also the relative effect is higher in these structures. The CPP structure is in some cases also called as a *spin valve (SV)*. This is the case when the antiparallel alignment is not obtained by interlayer coupling but due to the different coercivities or due to the pinning of the magnetization of one of the layers with an adjacent antiferromagnetic layer. Then the whole structure has two stable configurations and behaves like a valve.

4.2.3 Tunneling Magnetoresitance TMR

Magnetic tunnel junctions (MTJ), which are also known as *tunneling magnetoresistance* (TMR) structures, are built in a similar manner like the GMR trilayer in CPP geometry. They consist of two ferromagnetic layers separated by an insulator instead of the nonmagnetic metal as in the GMR case. In order to pass an electric current through such a structure the insulation layer may only be a few atomic layers thick, so that there is a reasonable probability for the electrons to tunnel through the barrier. This effect was first observed by M. JULLIÈRE in 1975 [80] on Fe/amorphous Ge/Co trilayer structures. He had observed a TMR effect of about 14 % at low temperatures. Since it was difficult at that time to produce reliable working tunnel junctions, the experiments were not pursued further. After the discovery of the GMR effect the interest in different magnetoresistive effects increased and the experiments on magnetic tunnel junctions gained more attention. As a result of this intensive studies much higher values of TMR, for example in Fe/MgO/Fe structures of about 200 %, were reported [81, 82].

The TMR value is defined similarly to the GMR case. It is the ratio of the difference in the resistance to the resistance in the parallel configuration.

$$TMR = \frac{R_{AP} - R_P}{R_P} \tag{4.11}$$

where R_{AP} and R_P correspond to resistances in the antiparallel and parallel configuration, respectively. This is the rather optimistic definition compared to the definition of ordinary magnetoresistance (Eq. 4.8). Its value is not limited since it is normalized to the resistance value in the parallel configuration.

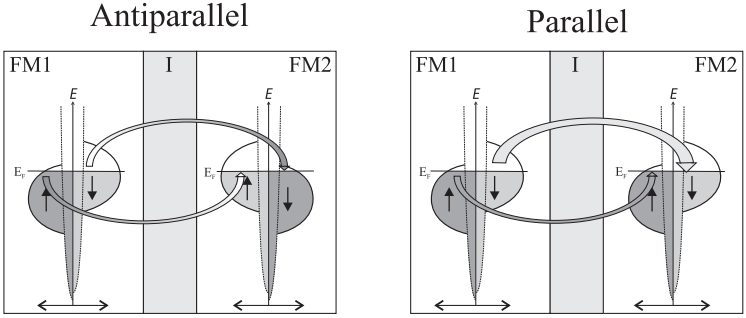

Figure 4.9: Magnetic tunnel junctions in antiparallel and parallel configuration. Conductance for the spin-up and spin-down channel are independent and proportional to the particular DOS at the Fermi-Level. This is represented by the width of the light and dark grey shaded arrows.

Jullière Model

The tunneling magnetoresistance is a consequence of spin dependent tunneling. In their early experiments R. MESERVEY and P. M. TEDROW [83, 84] had shown with trilayers of ferromagnet/insulator/superconductor (F/I/S) thinfilms the spin dependence of the tunnel current. The connection of TMR and spin dependent tunneling was explained already by M. JULLIÈRE in a simple model. He made two basic assumptions. First, the spin states of the electrons are not altered during the tunneling process. The spin-up electrons from FM1 tunnel to spin-up states of FM2 and spin-down electrons tunnel to the spin-down states of FM2. Both spin channels are independent as in the two-current model case. This means that if the two FM layers are magnetized antiparallel the electrons from the majority spin states tunnel to the minority spin states and from the minority states to the majority states, as depicted in Fig. 4.9 by the arrows. In this case the density of states is limited either on the

FM1 or on the FM2 side. But for the parallel magnetization the electrons tunnel to states with the same orientation and since the density of states for the minority states is relatively large on both sides this results in a higher conductivity. The second assumption is that the tunneling current is proportional to the product of initial and final density of states at the Fermi level of the corresponding spin state

$$G_P \propto g_{1\uparrow}(E_F) \cdot g_{2\uparrow}(E_F) + g_{1\downarrow}(E_F) \cdot g_{2\downarrow}(E_F) \quad (4.12)$$

$$G_{AP} \propto g_{1\uparrow}(E_F) \cdot g_{2\downarrow}(E_F) + g_{1\downarrow}(E_F) \cdot g_{2\uparrow}(E_F) \quad (4.13)$$

where $g_{i\uparrow}(E_F)$ are the DOS of the majority spin of FM(i=1,2) and $g_{i\downarrow}(E_F)$ the DOS of minority spin at the Fermi level. With these assumptions and the definition of polarization it is possible to rewrite the TMR expression in terms of the polarizations. The polarization $P_{i=1,2}$ in the corresponding FM layer is given as the ratio of the difference in the DOS of spin-up and spin-down states to the sum of the DOS of both orientations

$$P_i = \frac{g_{i\uparrow}(E_F) - g_{i\downarrow}(E_F)}{g_{i\uparrow}(E_F) + g_{i\downarrow}(E_F)} \quad (4.14)$$

If we rewrite Eq. 4.11 in terms of the conductance and use the second assumption (Eq. 4.12 and 4.13) we get

$$\begin{aligned} TMR &= \frac{G_P - G_{AP}}{G_{AP}} \\ &= \frac{[g_{1\uparrow} \cdot g_{2\uparrow} + g_{1\downarrow} \cdot g_{2\downarrow}] - [g_{1\uparrow} \cdot g_{2\downarrow} + g_{1\downarrow} \cdot g_{2\uparrow}]}{g_{1\uparrow} \cdot g_{2\downarrow} + g_{1\downarrow} \cdot g_{2\uparrow}} \\ &= \frac{2P_1P_2}{1 - P_1P_2} \end{aligned} \quad (4.15)$$

which is known as the Jullière model. By this definition the TMR value can be calculated from the polarization of the cor-

responding ferromagnetic layers. It can be used to explain the results of many experiments but besides its simplicity it has also limitations. For example in this model the spin-flip effects or the properties of the tunnel barrier are not taken into account. Therefore there are some discrepancies between the measured TMR values and the responsible polarization values. Some more accurate values of the polarization obtained by tunneling experiments across FM/I/S structures and by Andreev reflections are given in Tab. 4.3 [85].

Table 4.3: Experimentally measured spin polarization degrees of some ferromagnetic metals given in the literature.

Ref.	Ni [%]	Co [%]	Fe [%]
Meservey (1994) [86]	23	35	40
Moodera (1999) [87], Monsma (2000) [88]	33	42	45
Strijkers (2001) [89]	37	45	43

Chapter 5

Experimental

In this chapter some of the experimental specialties are described. At the beginning a short introduction to magnetic visualization techniques is given since they were crucial to identify the magnetic domain structure of the used contacts. This investigation led us to the selection of the contact geometry which was of great importance for the observed results. Then the peculiarities of sample preparation are revealed. One of these was the removal of adsorbates on CNTs which resulted in a clearer spin signal. And finally the measurement techniques and the setup for various experiments used in this work are described.

The spin degree of freedom of the electrons was for long ignored by conventional electronics. Although it has an inherent binary character and although it would be switchable energy efficiently [5], it could not make its way to industrial applications. The challenge is still to handle it in a controlled way. To overcome these challenges there are still many studies to be undertaken on the spin property.

The main goal of this work is to study spin transport in car-

bon nanotubes. It is motivated by the aim to combine the advantages of carbon nanotubes with the spin degree of freedom of the electrons. CNTs became famous for their outstanding transport properties, like being a ballistic conductor. This results in a long mean free path for the real devices. Thereby scattering events which would alter the spin state of the electrons are reduced. In addition to this, carbon itself has, due to its low nuclear mass, a low spin orbit coupling [48]. This results in a long spin diffusion length (see Sec. 3.5). Therefore it is well suited to study spin polarized transport phenomena over longer distances. In this work spin injection into the CNTs is realized through ferromagnetic contacts. We have observed in our early measurements that this is already the first hurdle to overcome. Therefore the influence of the ferromagnetic contact has to be understood in more detail and so the sources of perturbing magnetic effects can be avoided.

5.1 Influence of the Domain Structure

The proper way of handling the spin means the controlled injection of spin polarized current into the CNT, the accumulation of spin polarized electrons and the detection of the spin polarized current. To study this, one needs the possibility to orient the spin moment of more than half of the electrons. One possibility is to inject the electrons from a medium where they are already polarized, like in ferromagnetic metals. Therefore we first fabricated standard CNT devices in *field effect transistor* (FET) configuration with two contacts, one being the source and the other the drain contact. The highly doped Si substrate indicated by Si++ was acting as the gate electrode, controlling the current through the conduction channel. In our case the contacts were made of ferromagnetic Co, as shown in Fig. 5.1. The details of sample

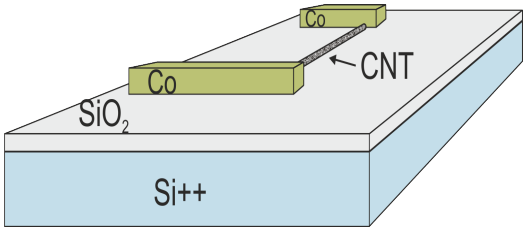

Figure 5.1: Schematic description of a standard CNT device in transistor configuration with ferromagnetic Co contacts for the spin valve measurements.

preparation are described in the next section.

Such a structure is called a *carbon nanotube spin valve* (CNT-SV). As explained in the previous chapter the density of states in ferromagnets is spin dependent, so that there are not enough states for an oppositely polarized current arriving at the drain contact. This increases the probability for scattering of oppositely polarized electrons. Depending on the relative orientation of the magnetization of the contacts the device reacts to a spin polarized electric current like a valve. This is similar to the polarizer and analyzer filters as in the optics case, where light also can pass only if both of the filters are parallelly oriented.

In our early measurements on CNT-SV we observed different types of switching effects. In Fig. 5.2 the current through a CNT-SV device at some constant bias voltage V_{SD} is shown, while an external magnetic field is increased slowly from negative to a positive value and then again decreased to the initial value. Some of this measurements showed step like switching as shown in Fig. 5.2a) some were a two level system like in Fig. 5.2b) and some others even were asymmetric with respect to 0 magnetic field. Similar spin valve signals were observed in individual thin (35 nm wide) Co stripes [90]. This happens when the current

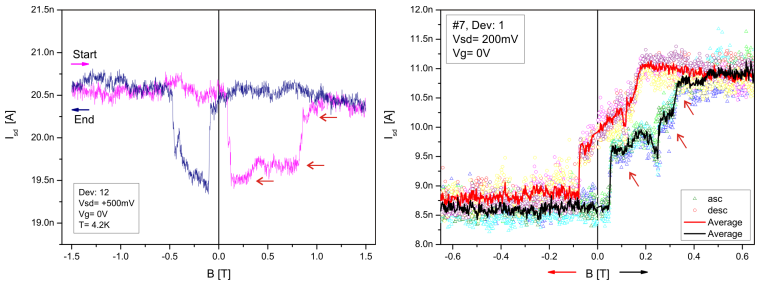

(a) (b)

Figure 5.2: Our early measurements on switching effects in magnetic field dependent current measurements through CNT spin valve structure. Non symmetric with steps a) and two level switching without valve effect b).

flows through a domain wall and the neighboring domains switch their magnetic orientation after each other. So one important problem in the study of spin transport across CNT was to clarify whether the magnetic field dependent signal was caused by the polarized electrons transported through the CNT or not. This led us to investigate the domain structure of the contacts with magnetic force microscopy.

It is known that ferromagnets build up an internal domain structure in order to reduce the magnetostatic energy (see Sec. 4.1.1). In each of these domains the magnetization and hence the polarization of the electrons is different. To gain insight into the domain structure we deployed *magnetic force microscopy* (MFM) as an imaging technique. MFM is a special type of the *atomic force microscopy* (AFM) which itself is a member of the scanning probe microscopy techniques.

The invention of the s*canning tunneling microscope* (STM) in 1982 by G. Binning and H. Rohrer [91] and the *atomic force microscope* (AFM) in 1986 [92] caused a revolution in the

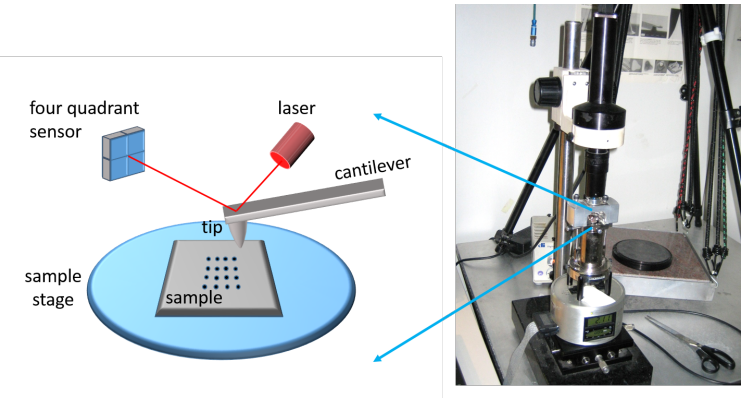

Figure 5.3: Schematic drawing of the measurement principle of an atomic force microscope (left) and the real device from Digital Instruments used in this work (right).

microscopy of surfaces. These techniques are used to investigate sample surfaces in the mesoscopic regime down to atomic resolution. Whereas in STM the tunneling current is detected in AFM a force between the sample and a fine needle is detected. This fine needle, which is also called the tip, is attached to a cantilever, which can be seen in the schematic drawing in Fig. 5.3. To generate an image the tip is scanned over the surface of a sample either in contact with the surface or in the regime where it is almost detached from it. A third method is to set the cantilever into vibration close to its resonance. At this frequency the amplitude is maximum and therefore the changes in the signal are easier to detect. The vibrating tip is then scanned at some distance over the surface of a sample. During the scan the distance between the tip and the surface changes depending on the surface topography. This affects the amplitude of the vibrating tip, which is then detected usually by a laser beam which is reflected from the cantilever towards a four-segment photo diode.

This change in the amplitude for every scan point results in the very often favored *amplitude* or the so called *false* image of the surface. The reason why this images are favored is because they look like an illuminated 3D image. During the scan, whenever a change in the amplitude is detected, a feedback loop system corrects the distance to the surface with the help of piezo crystals under the sample stage so that the amplitude is maximum again. This information is then used to generate the actual height or topography image.

For the magnetic force microscopy (MFM) a special tip coated with magnetic material is used. In this case the detected force is the dipole-dipole interaction between the magnetic surface and the magnetic tip. To generate an image with the magnetic information from the sample, the cantilever is scanned over the surface. But this is still challenging, while in the atomic force microscopy the forces are in the order of nN, the magnetic forces acting on the tip are two or three orders smaller [93]. When the tip is scanned close to the surface it is almost impossible to resolve the magnetic interaction. To measure the magnetic forces first the surface topography is scanned at a close distance to the surface, then on the same scan line but at a larger distance the tip retraces the topography. Since the atomic forces decay with r^{-6} and the magnetic forces with r^{-3}, the magnetic forces become predominant over the atomic forces at higher distances and can be detected more easily. This is the so called line-by-line method.

To verify this method some example images like on Fig. 5.4 were obtained on a piece of a computer hard disk. We see on the left side the usual AFM topography image of the surface of the hard disk with some scratches and dirt particles. The image on the right is acquired on the same area, but as mentioned

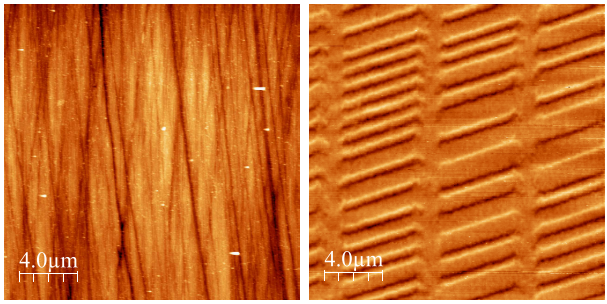

(a) (b)

Figure 5.4: Topography a) and MFM b) image of a typical computer hard disk. Both images are taken on the same area.

before at some higher distance. One can recognize clearly three vertical regions with differently thick segments. These segments are the ones and zeros of the binary recording. We don´t see extended dark or bright regions, we only see bright and dark lines forming the edges of the segments which correspond to domain boundaries. The color of the edge depends on the relative change of the orientation of the magnetization. Since the amplitude of the oscillation is always corrected to maximum, the color of an upward magnetized or a downward magnetized domain looks the same on the image. But during the scan, whenever the tip crosses a domain boundary, it is either attracted or retracted by the stray fields between the domains and this causes either a dark or a bright line.

When we imaged our early produced CNT spin valve samples with this method, we recognized, not surprisingly, that the contacting electrode paths consist of multi domains. The MFM images are shown in Fig. 5.5b) and c). The mosaic like patterns represent the ferromagnetic domains. One can recognize clearly how complicated this structure is built-up. In considera-

(a) Topographic AFM image (b) MFM image (c) MFM image zoomed

Figure 5.5: Cobalt thin film on Si/SiO_2 Substrate. It is lithographically structured in a typical contact geometry used for contacting individual CNTs.

tion of this fact, the results of our early measurements can now be explained more easily with the help of *the Barkhausen-Effect* [66]. HEINRICH BARKHAUSEN showed already in 1919 that the ferromagnetic hysteresis curve is actually not a smooth line but consists of small steps. This was the verification of differently oriented magnetic domains, the so called *Weiss-Regions* (see Sec. 4.1.1). While an applied magnetic field is smoothly increased these domains change their size and orientation abruptly, which is then the reason of the steps in the magnetization curve (see Fig. 4.1). Since the CNT length under the cobalt contact is several hundred nanometers it can happen that it is contacted by several domains and the one by one switching of the domains causes the steps in the spin valve signal, see red arrows in Fig. 5.2. Another effect is the internal magnetoresistance of the whole cobalt contact lead, caused by the changes in orientation between the domains. To explain these switching effects like in Fig. 5.2a) and b) one has to take complicated interactions between the domains into account. But for our basic study we need to be sure

to inject a spin polarized current into the CNT and to identify the signal, which is caused by this spin polarized current. This led us, of course, to the idea to produce CNT-SV devices with contacts which consist of only a single magnetic domain.

One possibility to create single domain contacts would be to shrink the size of the ferromagnetic material. To study this we have produced thin-film structures of thermally evaporated cobalt with varying shapes and sizes. Such structures are, due to their sizes, also named *nanodots* in the literature. It is known that the geometrical shape of a ferrogmagnet, especially in the nano regime, has a big influence on the domain structure. This is due to the so called geometrical anisotropy (see Sec. 4.1.1). One main appearance of this anisotropy is the in plane magnetization of thin ferromagnetic films [62]. Even the effect of crystallographic anisotropy is suppressed in thin films. To investigate this effect on the contacts of the CNT devices, thin films of ferromagnetic metals were produced. These are 30 nm thick layers of cobalt which were evaporated onto the usual Si/SiO_2 substrates, which are used throughout this work. Two fundamental shapes, squares and circles with different sizes were produced with the help of standard electron beam lithography (EBL), physical vapor deposition (PVD), and lift-off technique, for details see Sec. 5.2. These structures are then imaged with MFM.

As can be seen on Fig. 5.6, square shaped nanodots show still magnetic multi domain structure. The domain boundaries are clearly visible within the 1 μm edge sized bigger squares and are still recognizable down to the ones with 200 nm edges. This pattern is a so called closure domain structure, where the flux forms a closed path within the structure, compare to schematic in Fig. 5.9a). Such a configuration reduces the magnetostatic energy to almost zero [62]. It is formed mainly in cubic crystals

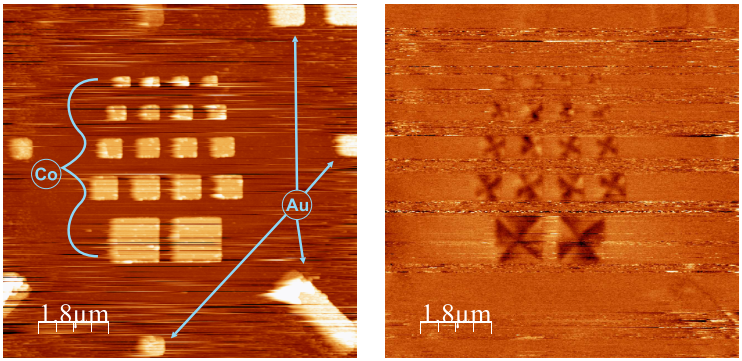

(a) Topography (b) MFM image

Figure 5.6: Square shaped cobalt nanodots with gold position markers. Both images are taken on the same area. The magnetic domains of the cobalt films are clearly recognized in b).

at corners and is a solution to avoid poles at edges.

On the contrary, such boundaries are not visible within the circular nanodots (see Fig. 5.7). These structures are also magnetized in plane, but due to the missing corners they show usually a vortex type magnetic domain. Similar to the square nanodots they form also a closed flux loop to minimize magnetostatic energy, with the magnetization parallel to the edges. But this vortex type domain structure has no internal domain walls. The orientation of every neighboring spin is turned only slightly with respect to the previous one. This circular orientation causes a singularity at the center. As can be seen in Fig. 5.7, there is a small dark region in the middle of the circles. This color contrast indicates a direction change of the magnetization. Hence the magnetization there is out of the plane. Based on the results of our magnetic domain study we produced for further investigations the contacts of the SWNT-SVs in this geometry. As we will

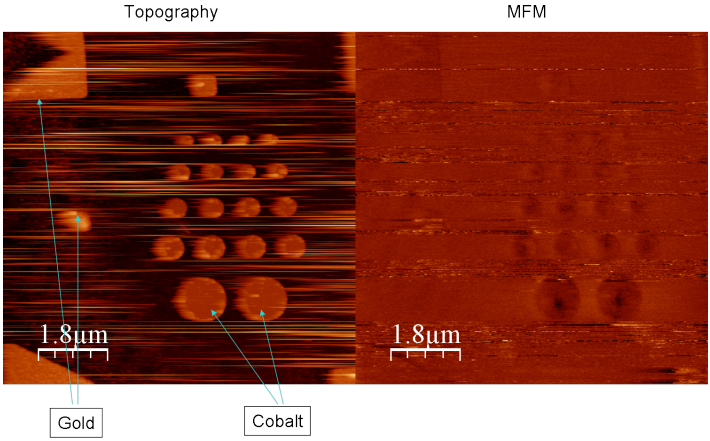

Figure 5.7: AFM & MFM images of circular nanodots. Vortex type domain structure is recognizable on the MFM image.

see in the next chapter the use of circular Co nanodot contacts was an important step in obtaining the spin dependent transport results presented there.

Our main concern during this study is to find out whether the spin polarization is preserved during the transport through the CNT. We have mentioned earlier that the observed changes in the current signal can be due the internal effects in the ferromagnetic contacts. To recognize the difference we have to avoid multi domains in our contacts and we have to be able to change the relative magnetic orientation between the two contacts. Therefore we have to know the magnetic hysteresis behavior, or, better to say, the reversal mechanism of the used magnetic structures. For single domains, which show single specific magnetic orientation, this reversal happens via coherent rotation [67]. This can be recognized by a high remanence at zero field and by an abrupt change at low field strength, similar to the ferromagnetic

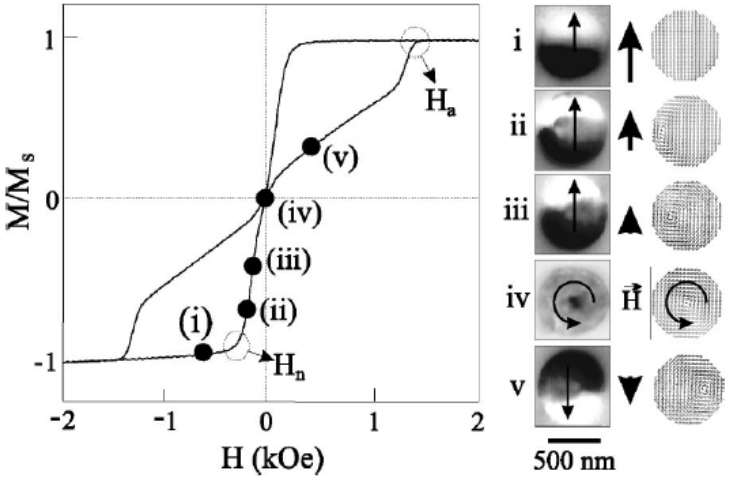

Figure 5.8: Magnetic hysteresis curve (left) and MFM images (middle) at the corresponding points (i-v) on the curve and simulated internal magnetization (right) for flat circular nanodots of 30 nm height [95].

hysteresis curve (compare Fig. 4.1). For circular nanodots in a specific range of dimensions the reversal happens via the vortex state [94][95].

The M-H curve for this kind of reversal is shown in Fig. 5.8. While the magnetic field is increased after negative saturation the single domain state (i) is preserved until a critical nucleation field H_n. Beyond this field a vortex appears at one of edges of the nanodot tangential to the applied field (ii). Further increase of the field moves the vortex through the nanodot perpendicular to the applied field (iii-iv-v). At zero field the vortex coincides with the center of the nanodot (iv) and the remanent magnetization is zero. The movement of the vortex continues until the annihilation field H_a at which the vortex is expelled from the opposite edge. The entrance point of the vortex can be on both

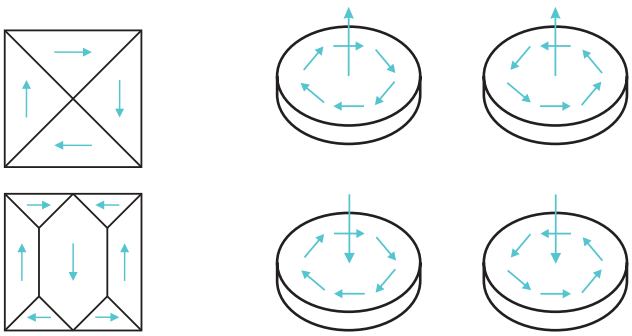

Figure 5.9: Schematic drawing of (a) square closure domain and (b) vortex type domain structures with different possible magnetic orientations.

sides of the nanodot and is determined by small magnetic irregularities. This gives a different handedness and hence nanodots with vortex ground state have a chirality. A schematic drawing of different vortex type closure domains is shown in Fig. 5.9. Additionally, they possess also a polarity which is given by the orientation of the magnetization at the vortex, upward or downward out of plane. These different orientation possibilities make nanodots interesting as storage elements.

5.2 Sample Preparation

As mentioned earlier, the aim of this work is to investigate spin transport in carbon nanotubes. The main challenges for this are to generate a spin polarized electron current, to inject this current into the CNT and to detect the signal after passing through the nanotube. To detect and distinguish the spin signal with electrical means was the major issue. Therefore every disturbing

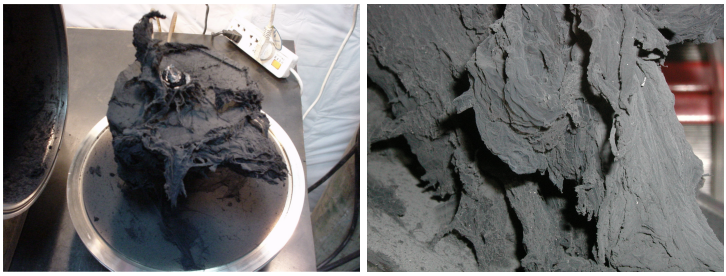

Figure 5.10: Carbon nanotube raw material as it is produced with the arc-discharge method. On the right hand side a closer view of the so called *spider web* which is hanging loosely on the target (left side) and inside the production chamber.

interaction from the surrounding had to be avoided wherever it was possible. To exclude any interplay between the neighboring walls, single walled carbon nanotubes (SWNT) were the material of choice. To produce SWNTs usually ferromagnetic catalysts are used but for our experiment such impurities would alter the results. Therefore a CNT material was chosen which was produced without magnetic catalyst particles [96].

CNT raw material is a fluffy powder, very much like soot, as shown in Fig. 5.10. It contains big agglomerations of all of the components. Beside the nanotubes there are graphitic and amorphous carbon impurities and catalyst particles. Like many nano materials they also tend to agglomerate, due to the Van der Waals forces. Especially the SWNT have a large surface area and are flexible, this promotes the formation of bundles. Therefore it is a material which is difficult to handle. Since the first requirement for our experiment is to bring *individual* CNTs onto a substrate, the raw material had to be dispersed and homogenized. The best way to do so is to suspend them stably in a liquid [97]. CNTs are hydrophobic and can not just

easily be dispersed in water. To do so they either have to be functionalized or covered by surfactants. It is also possible to suspend them in a few solvents like NMP or CHP [97], but this works only at very low CNT concentrations. Furthermore these solvents have a very high boiling point, which makes them not easy to process.

Since functionalization is impairing the conductivity and the solvents were not suitable for further process steps, our choice were the surfactants. We used the tenside *sodium dodecyl sulfate* SDS, which is a common dispersant for SWNTs. For this purpose we used a 1 wt % SDS solution in which the CNTs were dispersed with the help of ultrasound agitation. For this treatment a small horn type sonotrode was immersed into the liquid (see Fig. 5.11a)). Typical duration for the ultrasound (US) treatment was 30 to 60 seconds. We choose a rather short US treatment time. A longer treatment leads to a higher degree of dispersion but also breaks up the individual CNTs and shortens the length. During this short treatment time some of the CNT agglomerations get separated, which is enough for the sample production. The freely, in the solution moving nanotubes then will be enclosed immediately by the tenside molecules, which form the so called micells around the tubes. Due to the charge distribution on them these micells are then electrostatically suspended in the liquid. Therefore such dispersions of solids in liquids are called suspension. In order to remove the remaining agglomerates and other heavy particles like catalysts, the suspensions were then centrifuged at 14400 rpm 30 min. long. After centrifugation, the upper part of the suspension was decanted and used for the further steps during the sample preparation.

To built the circuits for the measurement the CNTs have to be put onto a carrying surface which is our substrate. Here

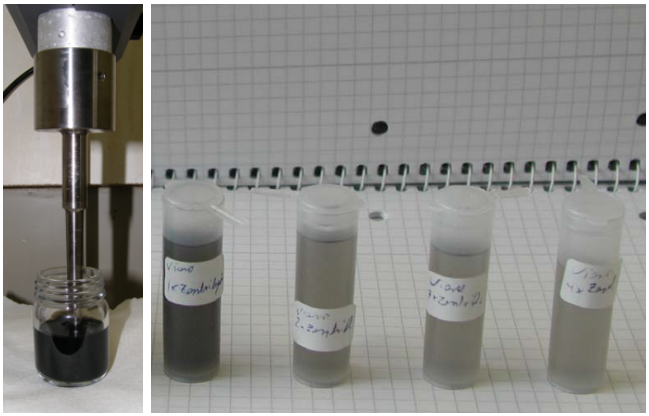

(a) (b)

Figure 5.11: a) Ultrasound tip sonicator immersed into a CNT suspension on the left and b) prepared suspensions with varying concentrations on the right hand side.

we adapted from the well known semiconductor technology. On top of highly doped silicon wafers a 200 nm thick layer of SiO_2 was grown with the *dry oxidation* method. During this growth method no water vapor is used. This slows the process down but leads to a higher density of the oxide layer, without pinholes. Such a high quality oxide protects against leakage currents and breakthroughs when higher voltages are applied to the gate electrode. From these wafers chips with the size of 4 mm x 4 mm were cut. This combination of the layers allowed the CNTs, to be contacted in the *field effect transistor* (FET) configuration. In this case the carbon nanotube acts as the conduction channel between the source and drain contacts and the highly doped Si substrate is used as the back gate electrode. The oxide layer serves as the insulator material between the back gate and the CNT (see Fig. 5.1).

There are different methods to place the CNTs on the mentioned substrates. Either the suspension has to be brought onto the substrate or the substrate has to be immersed into the liquid. During this step CNTs from the suspension are adsorbed on the surface. To increase the possibility of adhesion the surfaces of the substrates were silanized with *N-[3-(Trimethoxysilyl)Propyl] Ethylenediamine* (DAS). This creates a monolayer on the surface and enhances the adhesion between the nanotubes and substrate. Our method of choice was to put a droplet of the suspension on the silanized surface. After a waiting time of 5 min. the residual suspension was removed by blowing pure nitrogen gas with an airgun. This process is easier to apply than the dip-coating method since it does not require any apparatus to control the speed of the immersion and the emersion. Nevertheless, the adsorption process was one of the crucial ones. The density of the CNTs on the surface had to be adjusted more or less precisely at a very low density. Since the suspension consists besides the desired long individual tubes also of many bundles and short tubes. Actually one would need as many tubes as possible on the surface to be able to choose the appropriate ones, but on the other hand a dense network of tubes would cause also short-circuits between the contacting leads and would make a precise measurement impossible. This is the reason why the density had to be adjusted very well. For this adjustment the dispersion was diluted successively after each adsorption trial, until the desired concentration on the surface was reached. The remaining SDS is removed partially after the adsorption of the CNTs by rinsing with DI-water and by passing a high current, which is described later (see. Sec. 5.4).

After the adsorption of the CNTs on a carrier substrate the suitable ones for the measurement had to be located. For this

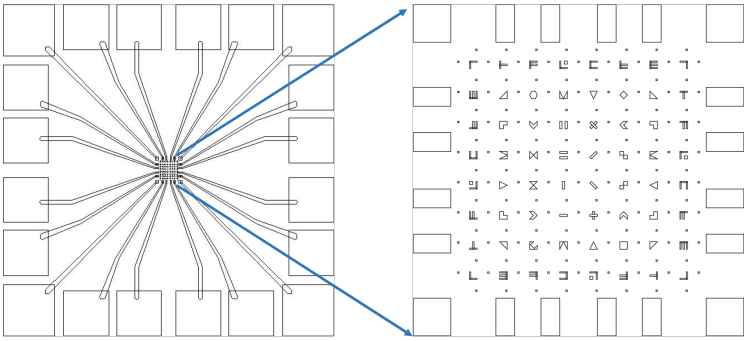

Figure 5.12: Contact pads on a substrate chip with leads towards the center (left) where geometrical shapes act as a coordinate system to relocate positions (right) [98].

purpose the surface of the substrates were scanned intensively with the help of an atomic force microscope (AFM), which was already mentioned at the beginning of this chapter. To define the positions of the tubes and to refind them after different processing steps a coordinate system was needed. For this purpose prior to the adsorption process markers, leads, and contact pads were produced on the surface. These markers consist of 30 nm thick evaporated gold thin film structures with different geometrical shapes. As can be seen on the right-hand side of Fig. 5.12, these markers form a coordinate system. With the aid of this shapes it was possible to navigate on the surface from marker to marker. The rectangles around the marker area are the inner contact pads. They are connected via leads with the outer contact pads (see left-hand side of Fig. 5.12). The outer contact pads are much bigger in size. This allows to attach thin gold wires to them with some special techniques. With a standard AFM under ambient conditions it is not possible to distinguish between thin CNT bundles and individual tubes. Therefore we

chose candidates which were thinner than 1,5 nm and longer then 1 µm. After choosing the proper tubes they had to be contacted with conductive pathways to the inner contact pads. This ensures the electrical connection to the measurement setup.

Here we adapted again from silicone technology. The method to produce tiny structures in semiconductor technology is called *lithography*. There are basically two types of lithography methods. In both cases the surface is covered with a resist, which is a sensitive polymer layer. Some portions of this resist layer can then be chemically altered by selective irradiation. By doing so one can achieve that the irradiated areas are more soluble with some certain solvents. After dissolving the altered regions, openings with the desired shapes are created in the resist layer. Through these openings one can selectively deposit many different materials, which have then the desired shape. The widely used and well know type of lithography is the optical one. Here the source of irradiation is UV-light. But this method has its limitations around structure sizes of several 100 nm's. To have geometrically well defined contacts below 100nm we used the so called *electron beam lithography* (EBL).

The steps of this procedure are similar as the previously described and are schematized in Fig. 5.13. After localizing suitable carbon nanotube candidates the substrates are covered with two polymethylmethacrylate (PMMA) layers. This is an electron beam sensitive resist. The underlying PMMA layer is chosen such that it is more sensitive to the electron beam. This creates an undercut (see Fig. 5.13 c)) below the upper PMMA layer and is crucial for the removal of the unwanted portions of the metal layer later on top of the resist. The substrates are then mounted into a specially modified *scanning electron microscope* (SEM), where the electron beam can be deflected in a controlled way,

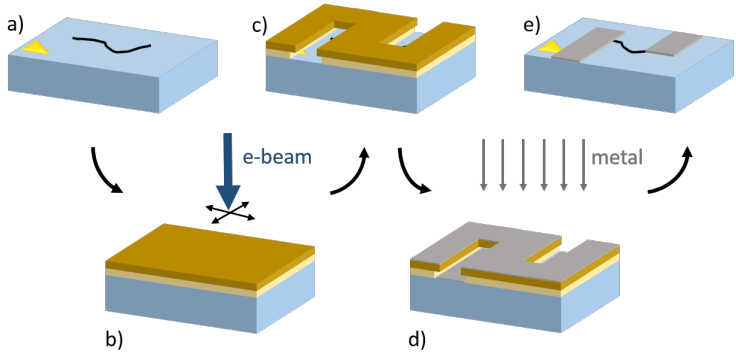

Figure 5.13: E-beam lithography (EBL) process steps a) to e) during sample preparation. Via this procedure metallic leads from the ends of the CNT until the inner contact pads are created.

such that the desired areas are exposed to the adjusted dose of electrons. These electrons hit the layer such that the polymer chains of the resist are broken into smaller pieces and can be dissolved with an appropriate solvent like MIBK. Since the underlying PMMA layer is more sensitive it will be affected more during the e-beam irradiation then the upper layer. When the altered parts of the PMMA are removed an undercut is created under the upper layer. With this procedure it is possible to open holes of any geometry well below 10 nm into the resist layer and to have access to the surface of the substrate.

After the realization of the open pathways from the inner contact pads till the ends of the CNT one can deposit on the whole surface the material of choice. For this purpose we have built our samples into a *physical vapor deposition* (PVD) device. This is basically a chamber in which for example metals can be heated such that they start to evaporate under high vacuum. The evaporated metal atoms spread towards all directions in the

chamber and on their way they also cover the substrates and build a layer on them. By controlling the temperature and the evaporation time the thickness of these layers can be adjusted. As can be seen in Fig. 5.13d) the metal layer also covers directly the surface of the substrate, through the openings in the resist layer.

Then the substrate is immersed into a solvent, in which the residual PMMA layer is dissolved. This has the consequence that also the parts of the metal layer without the supporting PMMA underneath are removed from the substrate. This process is the widely used *lift-off technique* in semiconductor industry. The previously mentioned undercut in the PMMA layer helps during this step to separate the upper metal layer from the metal layer in the openings and makes it usually easier to remove. But in the case of cobalt as the contacting metal it caused rather difficulties.

After the lift-off we observed under the AFM and SEM that the produced Co metal structures were surrounded by edges, which were fringed as can be seen in Fig. 5.14. From the AFM pictures the structure appears as if the metal is scattered back during the PVD process from the substrate‘s surface and piled up like a wall around the disks. The reason for this could be the high evaporation temperature of Co, which is considerably higher than for the usually used contact metals like Au, Ag, Cu, Al etc. The energy of the Co Atoms, when they arrive on the surface of the substrate, might be still to high and therefore the Co atoms might be mobile on the surface and form such surrounding walls. When the dimensions of magnetic metal structures are getting smaller, the edges, especially any asymmetries at the edges, affect the magnetic domain structure. Therefore the fringes were disturbing and had to be avoided. To overcome this problem we skipped during the EBL process the underlying first PMMA

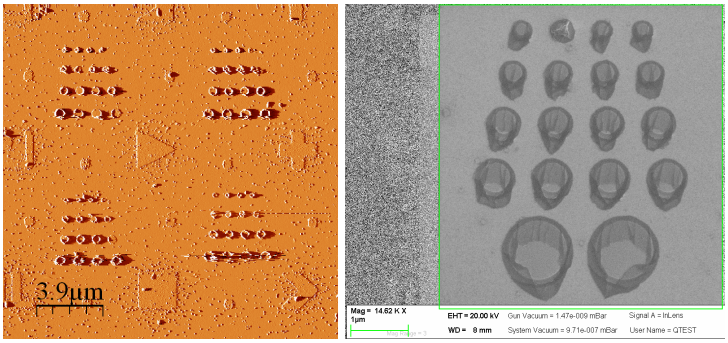

(a) (b)

Figure 5.14: Different sized Co disks after standard production show a) ring shaped surrounding walls under the AFM and b) a very thin more like a tulle surrounding under the SEM.

Layer. Because of the missing undercut in the PMMA layer the upper parts of the evaporated metal had a closed contact over the edge to the metal layer lying in the openings. This connection was then broken with the help of mild ultrasonic agitation during the lift-off process in an ultrasonic bath. As a consequence some of the contacts were destroyed, but the remaining structures had fairly smoothed edges.

An AFM image of Co nanodot contacts produced with the above described procedure is shown in Fig. 5.15a). These contact disks are placed on both ends of an individual or a thin bundle of SWNT, which is indicated by the red arrows on the same image. The Co nanodots, used as the source and drain contacts, are realized with different diameters of 400 nm and 600 nm. This difference is to ensure that both contacts have different coercive fields and switch the orientation of their magnetization at different field strengths. Some metals have a poor contact when they are evaporated onto the CNT. This is due to the

wetting problem of metals on the CNT surface. To improve the contact and hence the electrical connection at first a 3 nm thick layer of titanium was evaporated. Then a 30 nm thick layer of the ferromagnetic cobalt and on top of the Co layer a 10 nm layer of gold is evaporated as encapsulation. This Au layer protects the underlying Co layer from oxidation. Oxidation of Co would alter the results, since CoO is an antiferromagnetic material. After the production of the nanodot contacts the lithography, evaporation, and the lift-off process was run a second time to establish the conductive pathways between the nanodots and the inner contact pads. These leads were then made by pure Au. It has to be taken care during this step that the Au leads do not have direct contact with the CNT. This is controlled by SEM imaging shown in Fig. 5.15b). A schematic presentation and a optical microscopy image of the final CNT-SV device in single domain contact configuration is given in Fig. 5.15d) and c), respectively.

To perform the measurements an electrical wiring to the outer contact pads has to be established. For this purpose the chip with the lithographically contacted CNT is glued with electrically conductive silver paste into a chip carrier and *wire bonding* is applied. This is a very common method in semiconductor industry, to connect for example integrated circuit chips with their housing. During this step a thin gold wire with a diameter of 25 µm is pressed mechanically onto the desired metal surface and soldered by ultrasound. With this method one end of the gold wire is fixed to the chip carrier and the other end with the contact pads on the chip. This wiring can be seen in Fig. 5.16a) and b) as fine bright lines.

During the wire bonding step and also during the transportation of the samples between laboratories damage due to static

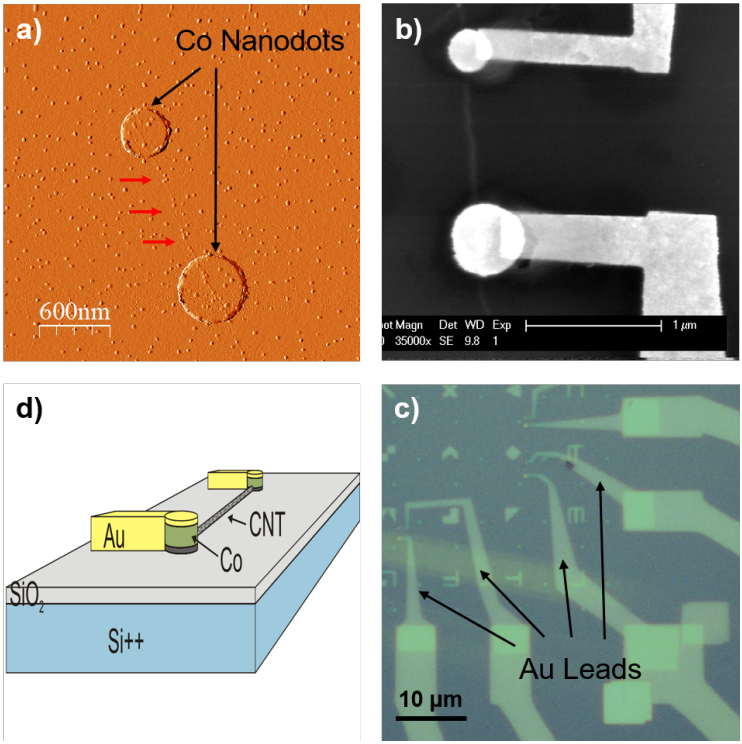

Figure 5.15: a) AFM image after the production of the Co nanodot contacts on a SWNT, the SWNT is indicated by red arrows. b) SEM and c) optical microscopy images of CNT-SV in the single domain configuration after the production of the gold leads. d) schematic of a whole CNT-SV device with cicular nanodot contacts.

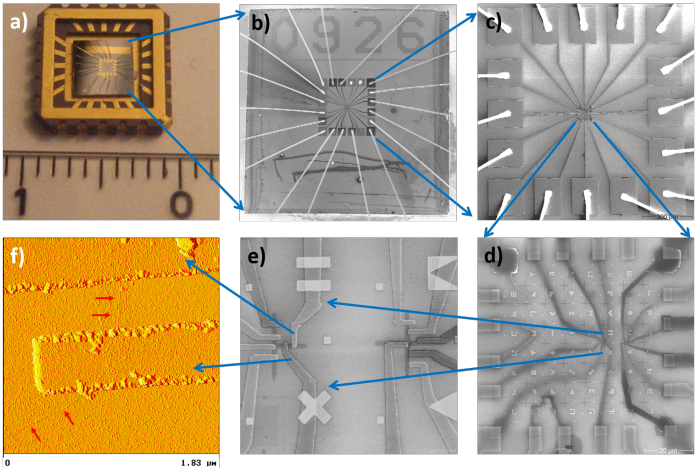

Figure 5.16: a) A sample chip mounted into a chip carrier and contacted by wire bonding. b) to e) SEM images showing a sequential zoom in until f) the AFM image of an individual SWNT (red arrows) between metallic leads.

discharging could occur. Therefore until the chip carrier was mounted into the sample stick all of the contacts were short-circuited with each other. This was done by wire bonding the contacts on the chip carrier with their neighboring ones. This short-circuiting wires were then removed after the sample was mounted into the sample stick. By short-circuiting, all the ends of the SWNT devices were on the same potential and they could not be harmed by relatively high currents caused by the discharge of static charge through the operator. With this precaution the yield of working CNT-SV devices could be increased from 10 % to 70 %.

5.3 Measurement Setup

Effects, which are related to spin polarization, are very sensitive to influences from outside and therefore difficult to measure. To study spintronic effects, the measurements have to be done in such a way that the electrical noise level is reduced to a minimum. A major source of noise is the thermal excitation of electrons. Consequently, cooling down the samples is the first method, to suppress the thermally caused white noise.

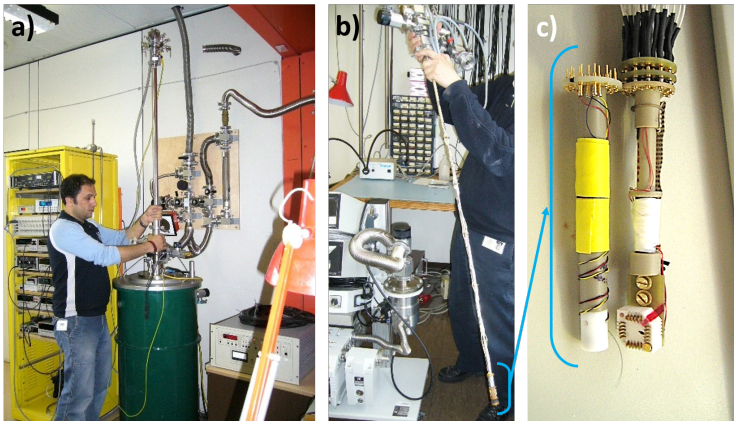

Figure 5.17: a) The cryostat during the insertion of the sample stick, the signal cables on top are connected to the measurement devices in the rack behind the operator b) The inner part of the sample stick with gas valves and connectors at the upper end and the special holder at the lower end c) Two different holders which can be attached to the sample stick.

This is usually done in a *cryostat*. Here we could benefit from the long term experience of our department. In Fig. 5.17a) the cryostat which is used for our measurements can be seen. It is actually a big, extremely well isolated barrel (vessel), filled with liquid helium. The temperature of liquid helium is 4,2 K

at standard atmospheric pressure. The cryostat has also a connection to a vacuum pump which can be used to decrease the pressure inside the cryostat. Depending on the pressure the helium reaches temperatures down to 1 K. The low temperature is also an important requirement to perform the magnetic field dependent measurements. It is needed to cool down the superconducting coil inside the cryostat. In the superconducting state of the coil a relatively high current can be passed through and hence a high magnetic field can be created. During our experiments a cryostat from *Cryogenic Limited* was used which could go up to six tesla.

To insert the samples into the cryostat a special holder had to be constructed. It consists of a metal stick with an attachment at the lower end. In Fig. 5.17c) two different attachments can be seen. Into the left one with the white cylindrical tip a hall sensor is mounted. This sensor is needed for the calibration of the magnet. Usually it is efficient to keep the cryostat cold but during longer breaks between the measurements it was not refilled with liquid helium so it went warm after the helium had evaporated. But after each new cooling down a recalibration of the magnet was required. The attachment on the right is used to hold the chip carrier with the sample devices. The chip carrier is clamped between the golden pins on the Teflon block at the lower end. This holder is connected via cables with a plug on the upper end of the sample stick. For the signal lines shielded coaxial cables were used. The sample stick is designed in such a way that also the surrounding atmosphere of the sample can be changed. Therefore the stick is put into a long stainless steel tube and closed tightly. For this reason also the used plugs had to be airtight. In Fig. 5.17b) the inner part of a typical sample stick can be seen. It incorporates also shieldings, temperature

sensors and the valves for evacuating and filling the needed gases.

Before the mounting of the chip carrier, the sample stick is connected to the measurement system and all signal lines are grounded. This is again a precaution to avoid static discharging. After the chip carrier is mounted into the sample stick the previously mentioned short-circuiting wires are removed. Then it is inserted into the tube and successively evacuated and flooded several times with helium. This washing with helium removes all oxygen from the tube and prevents the oxidation of the SWNTs in case of a local temperature increase due to Joule Heating during the measurements. After the final washing step the tube is flooded again with helium and left in this state. This residual helium is needed to ensure the thermal connection to the liquid helium bath when the sample stick is inserted into the cryostat.

As mentioned earlier, extreme care had to be taken to avoid sources of noises, therefore all connecting cables were shielded. As it could be seen from Fig. 5.15 there are usually several CNT-SV sample devices on the same chip. To access the individual devices separately the shielded cable connection is passed through a switch-box (see Fig. 5.18). This is a metal box acting as a *Faraday cage*. Herein the individual signal cables are separately connected to plugs on the outside of the box and are connected to the ground by a switch. This configuration prevents voltage spikes during the opening of the switches. By opening the switch actually the device is disconnected from the ground. After some preliminary characterization measurements at room temperature the sample stick is then immersed into the cryostat. The immersion of the stick is also the cooling down step for the sample. Hereby it is important to insert the stick as slowly as possible. This will reduce thermally induced stress and hence the breakdown of the contacts and any other parts on the chip.

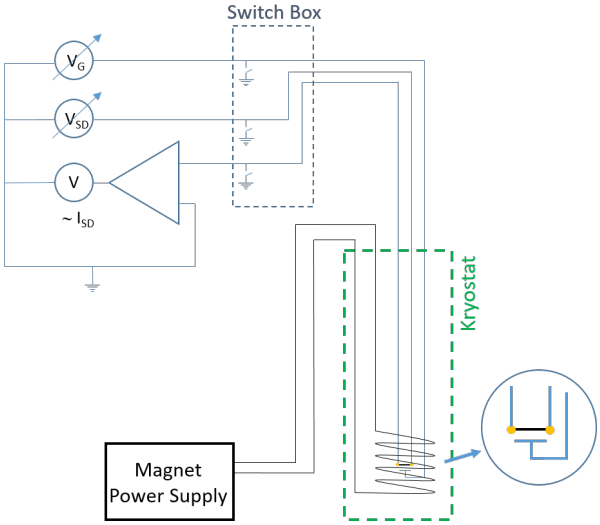

Figure 5.18: Measurement Setup Connection Scheme.

To apply a voltage and measure the currents the sourcemeter SMU 2400 and the multimeter 2000 from *Keithley Instruments* were used. To control the measurement and record the results the *Labview* software was utilized. It is a steering software, which allows the experimenter to program individual algorithms. We took care to generate some specific algorithms in order to have a precise and synchronous recording of the data. Especially the measurements depending on the magnetic field had to be recorded *on the fly*. This means that the measured electrical current I_{SD} was recorded while the magnetic field strength was increasing continuously. The synchronism of the magnetic field value with the corresponding current value was established through a synchronous start, a constant sweep rate and a syncronic read out from the measurement devices. The necessity of an on the fly measurement arose because of the self inductance

of solenoids. According to the relation,

$$U_{ind} = -L\frac{dI}{dt} \tag{5.1}$$

every change in the current induces an inverse potential. This behavior can be considered like a magnetic inertia. The generated magnetic field follows the set current with a time shift and this shift is depending on the sweep speed $\frac{dI}{dt}$. Therefore, if one wants to stop at distinct magnetic field values, one has to work with slow sweep rates and longer dwell times. Otherwise, between the stop points, it could also happen that the actual magnetic field is not at the desired value although the current of the power supply is at the set value. This could cause that the magnetic field crosses for example the critical coercive field strength value and hence a flip of the magnetization direction of the contacts between the stop points. And this would alter the results; as it would be difficult to correlate the measured values with the hysteretic behavior of the ferromagnetic contacts. To conduct the measurements at distinct steps of the magnetic field takes an unreasonable time. Therefore we choose the *on the fly* method since this method gives a continuous change of the magnetic field with a small constant offset and is less time consuming.

5.4 Current Induced Annealing

During several measurements it was observed that some devices don´t show any hysteretic magnetoresitive effect. To improve these devices we applied the so called *current-induced annealing* (CIA). This technique was developed also during this work. At the beginning of CIA was the observation that the conductivity

of CNT devices has increased after the application of a high bias voltage and hence a high current. This effect was observed with different contact metals like AuPd, Co and Ni under different atmospheres. The increase in conductivity is mainly attributed to the desorption of molecules from the CNT surface. Since the effect was observable as well at room temperature as at 4.2 K it can be explained by high energy phonon scattering rather then by Joule Heating. A detailed description is given in [99]. In Fig. 5.19 the I-V curves of a CNT-SV device are shown before and after several CIA cycles.

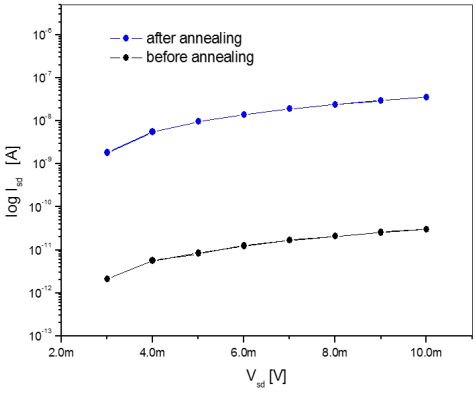

Figure 5.19: I-V curve of a CNT-SV device before and after the CIA treatment.

During the CIA treatment the bias voltage is slowly increased. The device is kept for one minute under the high current and then the voltage is decreased again slowly. Repeating this treatment showed each time an improvement which then saturated at some value. The improvement was roughly two or three orders of magnitude. Especially during the high current phase one has to

be careful about strong fluctuations of the current value. Since these can cause a sudden increase of conductivity which in turns increases the current beyond a critical value and damages the tubes. In cases of strong current fluctuations one has to abort and restart the CIA treatment. This increment of the conductivity recovered to its original value after the device was exposed to air again. This is also an indication that the effect is based on the desorption of molecules rather than the improvement of the contact to the metal. The molecules act as scattering centers which also cause the relaxation of the spin polarization. This effect and possible mechanisms are discussed in more detail in [100].

In Fig. 5.20 the magnetoresistance measurement before and after CIA treatment of a device is shown. With this technique it was possible to reduce the noise level and increase the observability of the spin signal.

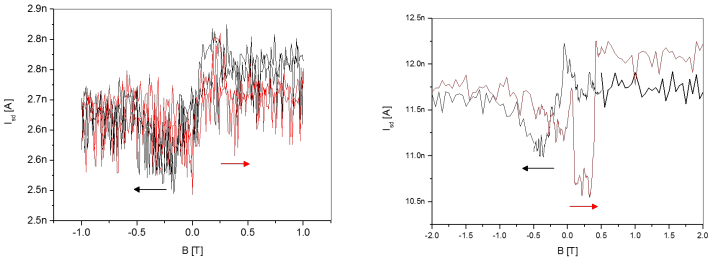

(a) Before annealing at $V_{SD} = 100\,mV$ (b) After annealing MR at $V_{SD} = 5\,mV$

Figure 5.20: Current through a standard CNT-SV device at 4,2 K a) before the CIA and b) after the CIA treatment. The arrows indicate the sweep direction of the magnetic field and correspond to the data with the same color.

5.5 Principle Spin-Valve Measurement

Until now we have described the required preparation steps for a nanotube spin valve sample, how to set up the measurement devices, and how to take care about some peculiarities. We are now in the state to conduct measurements on sample CNT-SV devices at helium temperature in the presence of a changing magnetic field. In the following we describe the principle of a basic spin valve measurement and expected results. The simple connection scheme of this situation is given in Fig. 5.21. Here the two Co contacts are colored differently with the according magnetization.

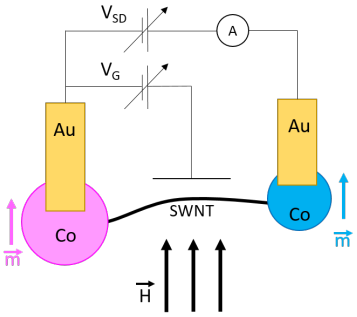

Figure 5.21: Basic connection scheme of a CNT-SV in single domain contact configuration with the external applied magnetic field $\vec{H}$.

In Fig. 5.22 the principle of a spin valve measurement is shown schematically. It shows the magnetization of the contacts and the corresponding current through the device, while the magnetic field is increased or decreased (upper or lower panel respectively). The left panels a) and c) represent the magnetization curves of the Co contact disks with respect to the applied magnetic field. Let us assume the blue curve belongs to contact

C1 and the pink curve to C2. On the right panels b) and d) the corresponding current I_{SD} flowing through the device is shown.

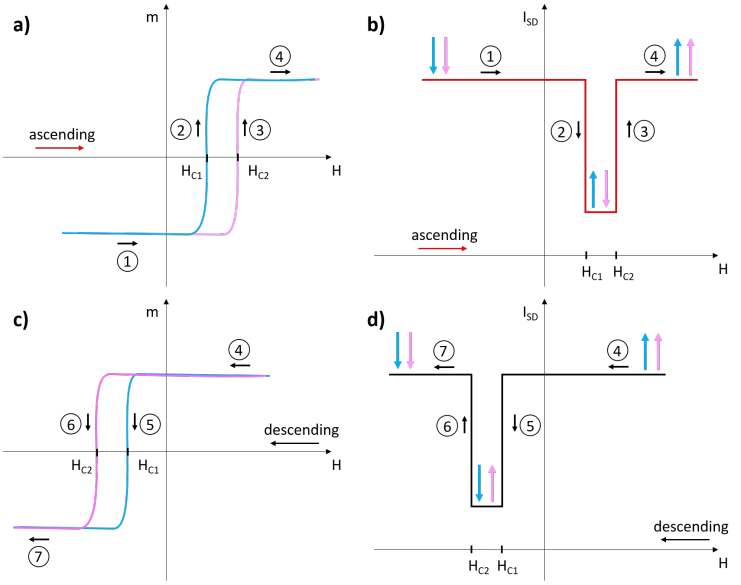

Figure 5.22: Schematic principle of the spin valve (SV) measurement. On the left panels the magnetization of the Co disk contacts and on the right panels the current I_{SD} passing through the device is shown.

A typical measurement starts usually after the magnetic field is driven to a low or high enough value, at which the magnetization of the contacts is saturated and aligned parallel with the applied magnetic field. This corresponds in our case to the starting state at position ① in Fig. 5.22a). Then a bias voltage V_{SD} is applied and the current flowing through the device is recorded. The appropriate voltage is deduced from preliminary characterization measurements. The current at this state is shown in panel b) and accordingly marked with ①. Then the applied magnetic

field is increased slowly. This is chosen to be the ascending direction. As we know from ferromagnetism (see Sec. 4.1.1) the magnetization of a domain flips its orientation when some specific magnetic field strength H_{ci} is exceeded (i stands here for the contact number i=1,2). This happens for the first contact at position ②. Both contacts are in the antiparallel orientation shortly after the flip of the first contact. This causes an abrupt increase of the resistance and hence a drop of the current which corresponds to the state between ② and ③ in the graph. After the coercive field strength for contact 2 is reached, it flips also at position ③ and both contacts are again in the parallel state ④. At this state the resistance drops and the current increases to its initial value again.

Similar behavior is observable when the magnetic field is slowly decreased again. This is shown in lower part of Fig. 5.22 in the opposite so called descending direction. We remember again from the magnetic hysteresis curve now the coercive field strengths are reached on the negative side at positions ⑤ and ⑥. Between them the magnetization is again in the antiparallel configuration this leads again to an abrupt increase of the resistance and this is observed as a drop of the current. After the flip of both contacts the initial resistance and current values are reached again.

To investigate the effect of the gate voltage or bias voltage on the ratio of I_{SD} between the parallel and antiparallel state one can run the above described measurement several times with the desired voltage values.

Chapter 6

Results and Discussion

In this chapter we present and discuss the results of the magnetoresistance measurements conducted with SWNTs, which were connected to disc shaped ferromagnetic cobalt contact structures, so called *nanodots*. The circular Co nanodots used here have, depending on their dimensions, either a single or a vortex type magnetic ground state domain configuration. Based on our study elucidating the domain structure of the contacts (see. Sec. 5.1) we choose this geometry for our contacts. The result of this work first to mention is the highly pronounced, sharply defined, and reproducible *tunneling magnetoresistance* (TMR), the value of which goes up to -70 %. This shows us that the combination of SWNTs with magnetic nanodot contacts is a highly suitable system to study spin transport. Further important results obtained with this system are the influence of magnetization reversal via the vortex state on the spin signal, the gate and bias voltage dependence of the TMR ratio, and a current flow in positive and negative direction at zero bias, which is attributed to magnon assisted tunneling.

As mentioned in the earlier chapter, samples are first characterized in terms of their voltage-current (I-V) and gate behavior at room temperature prior to the cooling. This characterization is needed to determine the type of the CNT. From the I-V characteristics in Fig. 6.1a) it can be seen that the sample device under investigation has an ohmic behavior. The figure shows also an important change from measurement to measurement already at room temperature, which is attributed to current induced annealing (CIA), described in the previous chapter. The initial resistance of the device was around $9,4\ M\Omega$ during the first measurement, but this dropped after some further characterization measurements. Especially the high current passing through the CNT during the gate behavior measurement caused a significant drop of the resistance down to $2,7\,M\Omega$. The gate characteristics taken at different bias voltages is given in Fig. 6.1b). It shows a weakly pronounced ambipolar behavior with a reduced conductance between the p- and n-type conduction regions. This is typical for small bandgap SWNTs. It shows also an increasing hysteretic effect, when the scan range of the gate voltage is increased.

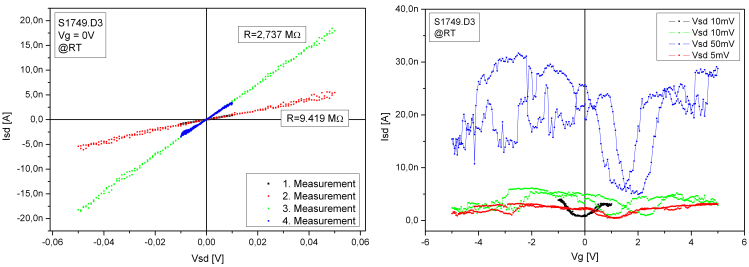

(a) (b)

Figure 6.1: a) Bias voltage and b) gate voltage dependent current measurement at room temperature (RT).

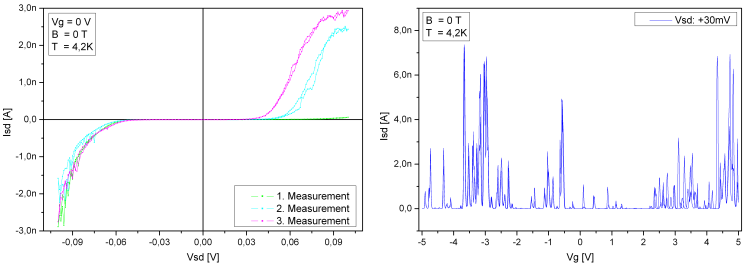

(a) (b)

Figure 6.2: a) I-V and b) gate behavior of a SWNT-SV device at liquid helium temperature (HT).

This hysteresis and the strong fluctuations of the current at higher bias voltages are an indication of *charge trap*ping, which is mainly caused by adsorbed molecules from the environment. To reduce the effect of adsorbed molecules the atmosphere inside the sample stick is replaced by helium after several cycles of flushing and evacuation.

After cooling down the sample to liquid helium temperature at 4,2 K the characterization measurements are carried out once more. The results are given in Fig. 6.2. The gate characteristics shows conductance oscillations which are typical for low dimensional transport experiments on mesoscopic structures like *quantum dots* (QD). This can be recognized also from the I-V curve. There is an extended flat region around 0 V bias voltage, which corresponds to the suppression of the current due to the Coulomb blockade (CB). The I-V curves shown in Fig. 6.2a) are recorded under the same conditions but with CIA treatments in between. We can clearly recognize the increase of the current after the successive treatments. The improvement occurs mainly on the positive side of the curve.

6.1 TMR on SWNT-SV Devices with Nanodot Contacts

In our measurements with circular Co nanodot contacts we found extremely pronounced and hysteretic magnetoresistance effect in SWNT spin valve devices. In Fig. 6.3a) the change of the current at a bias voltage of e.g. 30 mV is shown for 5 identical measurements, while the magnetic field is swept in the ascending direction from -500 mT up to +500 mT. This is a typical SV measurement. Here we have observed sharply defined abrupt changes in the source drain current flowing through the nanodot contacted SWNT device. The increase of the current between these switchings corresponds to almost 250 % of the initial current level for that given specific gate voltage. One can recognize that these two abrupt changes happen at small positive values of the magnetic field. A similar switching happens during the reversed, descending sweep of the magnetic field at the same magnitude with opposite sign (see. Fig. 6.4). The graph in Fig. 6.3b) shows a magnified view of the change. The switchings occur always exactly at the same coercive fields, indicated by the arrows in the graph and are symmetric with respect to zero magnetic field during the ascending and descending sweep of the magnetic field. This suggests strongly that the abrupt changes in the measured current are from the two ferromagnetic contacts. The two switching effects indicate also that two magnets with different coercive fields are involved. This is consistent with the different sizes of our nanodot contacts. Since there are on the sample only the two circular nanodot contacts of ferromagnetic material, they can only be the source for this response in the measured signal.

An internal abrupt change of the conductance within the nan-

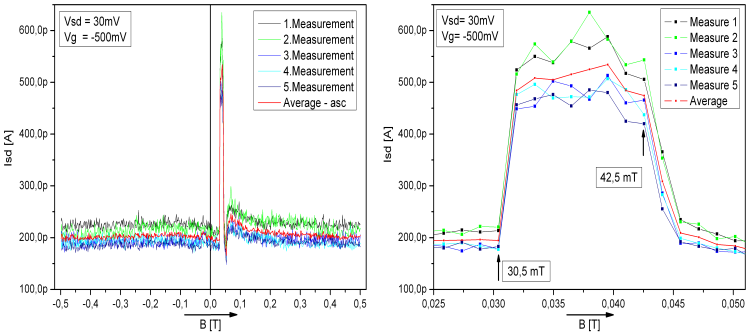

(a) (b)

Figure 6.3: TMR signal of circular nanodot contacted SWNT-SV a) 5 identical measurements during ascending scan of the applied magnetic field, the red curve is the average, b) magnified view of the measurement, the corresponding switching fields are pointed by arrows.

odots seems to be less likely responsible for the observed signal. Such an abrupt change within small sized (nanoscaled) ferromagnets can happen when the current flows across a domain wall and the two neighboring domains flip their magnetic orientation at different coercive fields [90]. But for our samples this seems to be less likely, because the applied magnetic field is in plane with the disk shaped nanodots, but the current flows vertically through the nanodot. The Co nanodots in our samples are capped with a gold layer which is then connected to gold leads (see Fig. 5.15b) and d)). The resistance between the gold cap and the gold lead is usually much less than the contact resistance between the gold lead and cobalt layer. Therefore the current from the lead will first flow to the gold capping layer and then from top to bottom through the contact configuration. In this direction the thickness of the nanodot is in the range of the domain wall and it

is known from literature that for thin films and flat nanostructures domain walls are built up only in the lateral dimensions. Previous MFM measurements (see Sec. 5.1) have revealed that the used nanodots have a vortex type ground state without domain walls. Additionally, if the observed effect would be caused by internal domain switching inside the nanodots, then it would also cause four switching effects due to the two nanodots, which was not observed in the case of the nanodot contacts during our measurements. The observed change in our case is therefore due to the change of the relative magnetic orientation between the two nanodot contacts involved. Hence we can conclude that the spin polarization in between must be preserved to some degree, while the current is passing through the SWNT.

This type of magnetoresistance is similar to the one in classical tunneling magneto resistance (TMR) devices, where the current tunnels between two ferromagnetic films through a barrier. In the case of the SWNT spin valve device the carbon nanotube represents a quantum dot which is connected to the ferromagnetic contacts through tunnel barriers. Therefore the observed effect can be called in analogy also a TMR effect. The main difference in our measurement compared to classical TMR is that the current level, against our expectation, increases for the antiparallel configuration. This results a negative TMR ratio. One possible explanation is that the spin orientation flips during tunneling and since more states are available during the antiparallel configuration for the opposite orientation this leads to an increased current. This idea is also supported by some of our other observations.

The tunneling magneto resistance TMR is defined as the ratio of the change in resistance ΔR to the resistance in the parallel configuration R_P. The Eq. 4.11 can be rewritten in terms of the

source drain current I_{SD}:

$$TMR = \frac{R_{AP} - R_P}{R_P} = \frac{I_p - I_{AP}}{I_{AP}} \tag{6.1}$$

where the subscripts P and AP correspond to the parallel and antiparallel orientation of the magnetization of the nanodots, respectively. A complete SV measurement cycle is given in Fig. 6.4a). The arrows indicate the start and end position of the measurement and the hysteretic behavior of the signal. This measurement is taken at a gate voltage of $V_G = -500\,mV$ and yields a TMR ratio of -59,9 %, which is also the largest of the observed values at the bias voltage of $V_{SD} = 30\,mV$. A graphical demonstration of a representative TMR calculation is shown in Fig. 6.4b). The current values used for the calculation are indicated by the green lines and yield a TMR of - 58,9 % at the gate voltage of $V_G = -520\,mV$.

As we have discussed earlier (see. Sec. 4.2.3) the TMR ratio depends on the spin polarization degree of the ferromagnets and can be calculated with the simple Jullière model. As a first approximation we can use the formula given in Eq. 4.15, but with the absolute value of the measured TMR.

$$|TMR| = \frac{2P_1P_2}{1 - P_1P_2}$$

where P_1 and P_2 correspond to the polarization degree of the ferromagnetic source and drain contacts, respectively. If we assume the same degree of polarization $P_1 = P_2 = P$ for both contacts. We can obtain from this equation e.g. for the highest observed TMR of $-59,9$ % a polarization degree of $P = 48$ %. This is in reasonable agreement with the value reported in literature

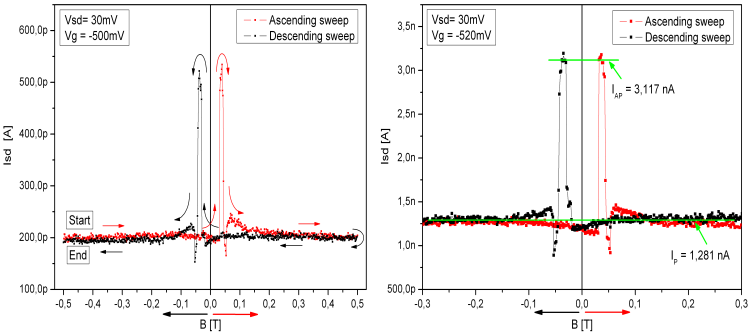

Figure 6.4: The current signal during a complete SV measurement cycle: a) the applied magnetic field is started at negative saturation and then slowly increased up to positive saturation and then decreased back again to negative saturation. b) the current values for the parallel and the antiparallel state are indicated by green lines.

$P_{Co} = 46$ % [89] for cobalt, measured by Andreev reflections at the interface to a superconductor (see Tab. 4.3).

Another approach to derive the polarization degree of the ferromagnetic contacts would be to include spin flip into the formula above. If we assume that all electrons undergo a spin flip then the conductance is correlated with the oppositely oriented density of states. This yields a modification of the formula 4.15 where now TMR^* is negative.

$$\begin{aligned} TMR^* &= \frac{G_P - G_{AP}}{G_{AP}} \\ &= \frac{[g_{1\uparrow} \cdot g_{2\downarrow} + g_{1\downarrow} \cdot g_{2\uparrow}] - [g_{1\uparrow} \cdot g_{2\uparrow} + g_{1\downarrow} \cdot g_{2\downarrow}]}{g_{1\uparrow} \cdot g_{2\uparrow} + g_{1\downarrow} \cdot g_{2\downarrow}} \\ &= \frac{2P_1(-P_2)}{1 - P_1(-P_2)} \end{aligned} \tag{6.2}$$

the polarization degree obtained from the modified formula is 65 % for the TMR of $-59,9$ %. This is rather higher than the value obtained with absolute value of TMR.

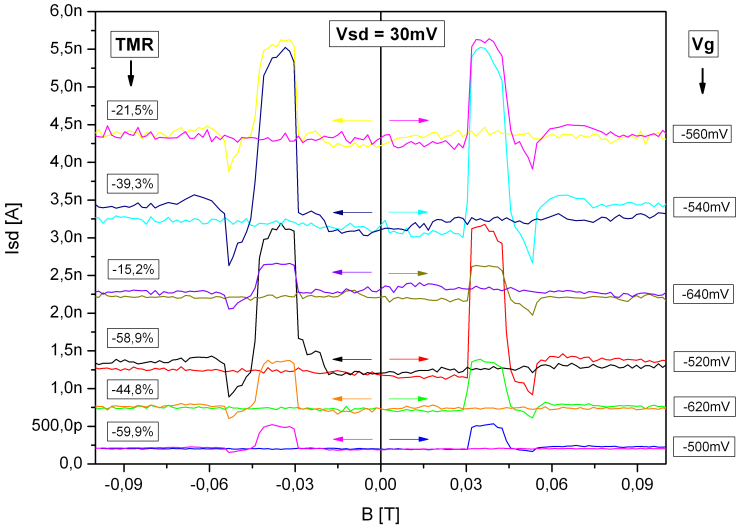

Figure 6.5: Spin valve measurements for different gate voltages at the bias voltage $V_{SD} = 30\ mV$. The gate voltages are given on the right hand side and the corresponding TMR values on the left.

The discrepancy between the values can be attributed to the difference of the model and our sample. In our case the tunneling between the ferromagnets happens additionally through a quantum dot. So the MR depends also on the energy levels of the QD. This is also the reason why we could observe a modulation of the TMR with varying gate voltage. The observed MR values for some gate voltages are given in Fig. 6.5. We can observe in this graph a strong gate dependence of the TMR value, which varies from 15 % to almost 60 %. The gate dependent change of MR is discussed in the following sections.

6.2 Effect of Magnetization Reversal via Vortex on TMR

An interesting and reproducible feature of the measurement is a small dip in the current signal during the SV measurement. It occurs after the second switching at higher ± magnetic field. In order to compare the effect at different gate voltages the measured current values are normalized to the current level I_p at parallel configuration. This comparison is shown in Fig. 6.6. Whereas the first switching ① is rather a sharp increase the second switching ② seems to be superimposed by a gradual change of the conductance. This can be recognized from the slow decrease which starts already between the switchings ① and ② and continues until the third switching ③. In these graphs one can also observe a correlation between the level of the dip and TMR ratio. As the magnitude of TMR decreases also the dip gets smaller. And when the TMR disappears as it is the case for the gate voltage $V_G = -660\ mV$, there is also no dip observable. After the dip, the current restores back to the I_p level via a third sharp switching at position ③. Interestingly, this picture is not consistent with the expected behavior of two single domain contacts. To explain this effect we have to look closer into the magnetization reversal behavior of circular nanodots.

We know that after saturation at higher magnetic field the reversal of the magnetization for small sized magnets e.g. nanodots depends on their ground state magnetization. As we have discussed earlier for flat circular sub-micron sized nanodots this happens through the vortex state with zero remanence and for smaller nanodots below 100 nm in diameter through spin-flip which is indicated by a high remanence. But there is a broad region of bi-stability between these types of ground states. This

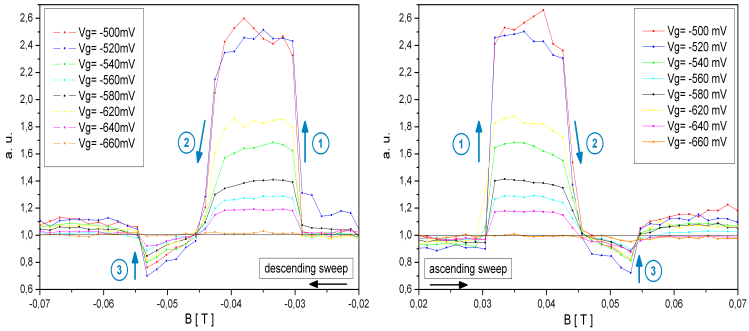

(a) (b)

Figure 6.6: For comparison the different current signals at different gate voltages are normalized to the current level at parallel magnetization at saturation. Besides the two main switchings a smaller third switching can be observed, which is also symmetric with respect to zero magnetic field for the a) descending and b) ascending sweep direction of the magnetic field.

means that magnetization reversal can occur for some nanodots via spin-flip like in a single domain although its magnetic ground state is a vortex state. Since circular nanodots with vortex state magnetization have attracted a lot of attention as non-volatile memory storage elements, there exists several experimental and theoretical work in literature. In Fig. 6.7a) a phase diagram for different magnetic ground states is given [101]. The authors have shown that between the three basic magnetization ground states, out of plane (I), single domain in-plane (II), and vortex state in-plane (V) there is a broad region (III) and (IV) where both ground states can exist. The authors conclude that the ground state in this region depends on the magnetic history and that it can be altered by thermal treatment. The two dashed lines added on the graph indicate the diameters of the nanodots

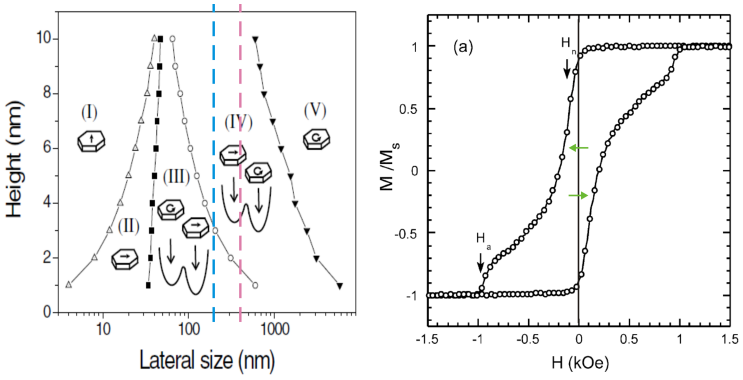

Figure 6.7: a) Phase diagram of magnetization reversal for nanodots [101] and b) magnetization hysteresis curve for elliptical nanodots [102].

used in this work. Since the data given in this diagram is only up to 10 nm height for the nanodots we can estimate by extrapolation that the nanodot with 400 nm diameter and 30 nm height will certainly lie in region (V), but the smaller one with 200 nm diameter might still be in the bistable region (IV) or at least close the border between region (IV) and (V). This means that while one of our nanodots will reverse its magnetization during the magnetic field sweep like a single domain at once through a spin-flip the other will switch via the vortex state.

Another observation reported in literature is, that for some cases the magnetization of the vortex state nanodots shows a high remanence at zero magnetic field but then they switch to the vortex state right after the sign change of the magnetic field. So the nucleation of the vortex does not happen as usual on the same side of the saturation magnetic field but on the other side with opposite sign after passing the zero field. This is shown

in Fig. 6.7 b) e.g. for the special case of slightly asymmetric elliptical nanodots [102]. This behavior has also been observed for nanodots with shape asymmetry e.g. a flat edge [103] or with nanodots which have an oxide ring outside [104]. Also lowering the temperature shifts the nucleation field H_n [105] so that the branches of the magnetization curve move apart as indicated by the green arrows in the graph (compare also Fig. 5.8).

If we now combine these observations from literature, we can suggest a possible explanation for the third switching which we observe in our current signal. In Fig. 6.8 a principle explanation for the ascending sweep is given. The left panel shows the magnetization curve of the two nanodots and the right panel the corresponding response of the current signal. The magnetic orientation of the nanodots are represented by the blue and pink arrows. Lets assume the magnetic field sweep is started from negative saturation in the ascending direction. When the applied magnetic field passes zero, first a vortex is nucleated at the field H_{n1} within the lager diameter nanodot. After the first switching indicated by ① the magnetic orientation of the nandots are maximally opposed to each other. The degree of opposition depends on the orientation of the applied magnetic field and the entrance point of the vortex. After further increase of the magnetic field the second i.e. the smaller nanodot reverses its magnetization via spin-flip at H_{C2}. This causes the second switching ② in the current signal. The magnetization of the smaller nanodot is given by the blue curve. During the further increase of the magnetic field the vortex continues to move inside the nanodot and the relative spin orientation is still changing. In this region we observe a further drop of the current which is even smaller than at the parallel configuration. One explanation could be that actually during parallel configuration in the vicinity of the

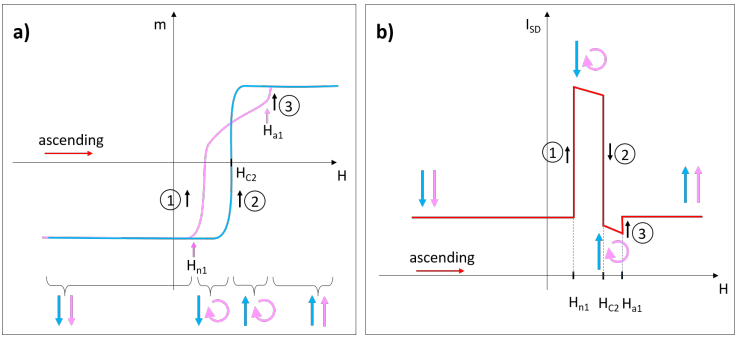

Figure 6.8: The magnetization reversal curves of the two nanodot contacts: single domain in blue and via vortex state in pink (left panel). The observed current signal as a function of the magnetic field (right panel).

CNT touch-point the magnetization is not parallel. This can be caused by a local pinning center. It might be that parallelism is achieved during the movement of the vortex through the contact and therefore the current reaches a smaller value between the second and third switching. Finally the vortex is annihilated at a field of H_{a1} which causes the current to switch for a third time ③ and the current signal restores to its original level at saturation. The same principle explanation can be applied symmetrically for the descending sweep of the magnetic field.

We made also the observation that the current level between the first and the third switching is not parallel to the current level at magnetic saturation (see Fig. 6.6). According to our model of the combination of the two reversal mechanisms this can be explained by the movement of the vortex inside the nanodot. As we can see in Fig. 6.8 the magnetization of the pink curve is not constant between the nucleation and annihilation field. During the movement of the vortex the relative orientation between the nanodots especially at the direct contact point

of the SWNT is still smoothly changing. This smooth change is probably responsible for the smooth change of the current in this region.

6.3 Gate Dependence of TMR

We have shown in the introductory part that SWNTs connected to metallic contacts through tunnel barriers behave like quantum dots and exhibit conductance oscillations with varying gate voltage (see Sec. 2.3.1). For our SWNT-SV we could observe similar behavior. A detailed analysis revealed a multi QD structure. This can be deduced from the charge stability diagram given in Fig. 6.9. In the stability diagram one can clearly recognize diamond shaped areas where the conductance is zero. This is an indication of single electron interaction. Additionally, it is also obvious that the shapes of the CB diamonds are irregular, they are ordered like shards, but the borders of the CB diamonds are still straight lines. These border lines show a few different slopes which repeatedly appear. This resembles the internal structure, that several QDs are involved in this transport result [106]. It is known from literature that single CNTs can behave like a series of quantum dots. The reason for this might be structural defects or adsorbed particles which behave like tunnel barriers.

We have already mentioned that magnetic field dependent measurements at different gate voltages yield different TMR ratios. This modulation can either be explained by a field effect from the gate directly on the spin or by interference effects caused by spin dependent reflections at the contacts. For a field effect as in the case of the Datta-Das transistor a relatively high spin-orbit coupling is required, which is not the case for CNT [107].

To obtain a more detailed view how the gate voltage effects

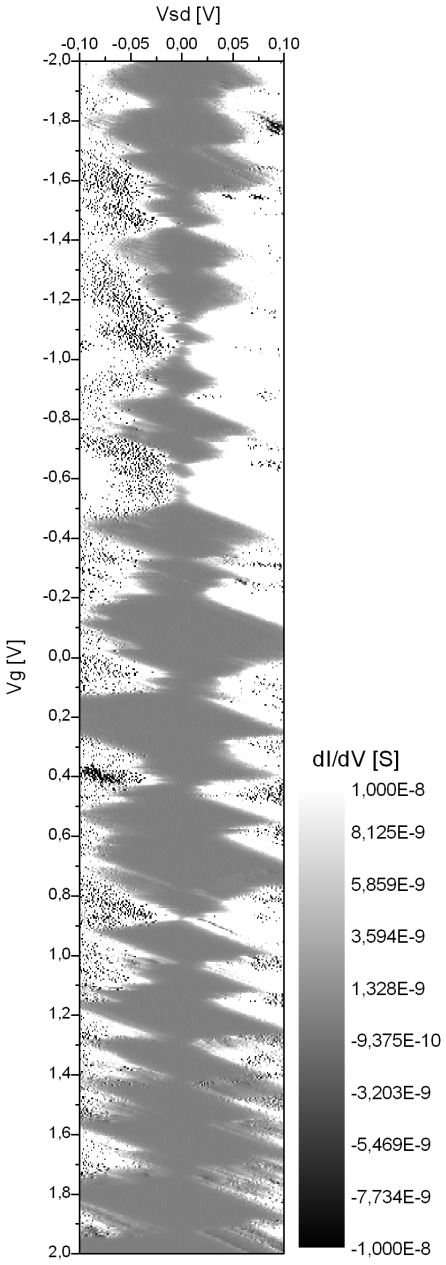

Figure 6.9: Charge stability diagram at B = 0T.

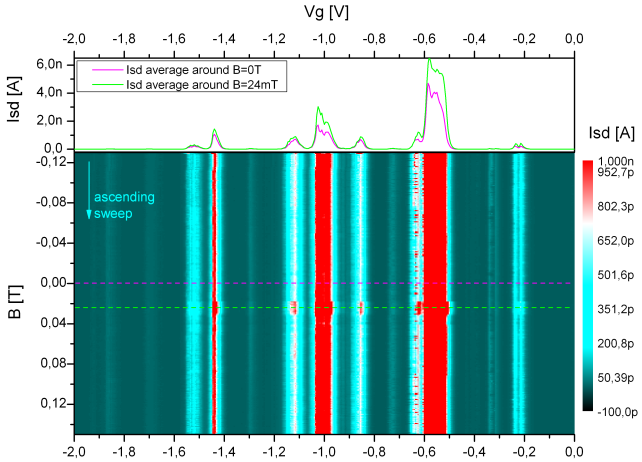

Figure 6.10: Gate dependence of TMR. Gate scans at different magnetic fields (lower panel) the current value is given in color scale. Two individual gate scans at the two different magnetic orientations (upper panel).

the TMR a series of measurements was taken. In Fig. 6.2b) a single gate voltage dependent current measurement was shown at zero magnetic field. Similar gate scans were now taken for clarity in a smaller gate voltage window between -2 V and 0 V. After each scan the magnetic field was increased gradually in the ascending direction from negative saturation towards positive saturation (from -150 mT to +150 mT). The result is a 3-dimensional data set, illustrated in Fig. 6.10.

The two varying parameters V_G and B are given on the x and y axis whereas the measured current is given in the z direction, here as a color scale image from topview. One can recognize many vertical parallel lines which correspond to the conductance peaks. From the colorscale given on the right-hand side one can see that some of the peaks lie well above 1 nA whereas many

others are below 500 pA. One can clearly recognize in the middle part of the color image a region where the conductance of almost all peaks are increased. This is the region between 18 mT and 31 mT and is indicated by the green dashed line. In the upper panel of the figure two individual gate scans are shown. The one in green is the average of several gate scans around 24 mT and the pink curve is the average of the gate scans around 0 mT. They correspond to the antiparallel and parallel magnetic orientation of the nanodots respectively. The positions of these curves are indicated by the dashed lines in the lower panel in corresponding colors.

We can deduce from these two curves that the difference is larger on the conductance peaks. If we calculate the TMR ratio and combine both diagrams we can recognize that with increasing conductance also the TMR increases in the negative direction. This comparison is shown in Fig. 6.11. We can see that the TMR values are negative for allmost all gate voltages and vary between 0 and -60 %. The peak values lie mainly between -30 and -50%. Similar modulation of the TMR value was already observed by others [57, 108] where conductance maxima also correlate with the TMR minima. In their case the amplitude of the modulation was about 5 % or 15 %. This behavior can be explained by the Breit-Wigner formula where the transmission probability is spin dependent. This model yields negative TMR for strong asymmetric coupling of the contacts which supports also our observations described in the next section.

A closer examination of our result yields that the TMR peak positions are slightly shifted but the current peaks during the parallel and antiparallel configuration are not shifted. To highlight this we have included vertical lines between the I_{SD} and the TMR curve as a guide for the eye. In order to have better

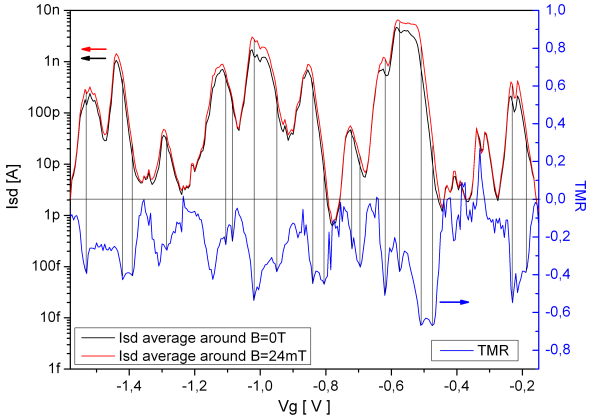

Figure 6.11: Comparison of TMR with the corresponding conductance oscillations. Black and red curves are current values at 0 and 24 mT, respectively. They are given in logarithmic scale. The TMR ratio is shown in blue. The appropriate y-scales are indicated by arrows. Vertical black lines are a guide for the eye.

correlation between the TMR and the current signal the current signal in Fig. 6.11 is shown in logarithmic scale. Otherwise the small conductance peaks between the main peaks are not visible and the correlation between the current and TMR signal is not obvious.

6.4 Tunneling Current and Spin Valve Effect at Zero Bias

During our measurements an interesting feature at low bias voltages attracted our attention. In Fig. 6.12 a gate scan of the sample is shown where this feature is visible. The arrows in the graph indicate the position of small dips where the current drops below zero although a positive bias voltage of 5 mV is applied.

By comparison with previous measurements e.g. as given in Fig. 6.2b) we find that the level positions of the SWNT-QD are at the same gate voltages but dips occur directly at the foot of conductance peaks. At first sight it looks like an uncorrected offset problem which is close to the noise level. But further investigation revealed that this is not the case. The noise level was determined to be around 0,5 pA with a positive offset of about 0,25 pA (see. inset of Fig. 6.13). As we will see in the next figure the negative signal is significantly above these values.

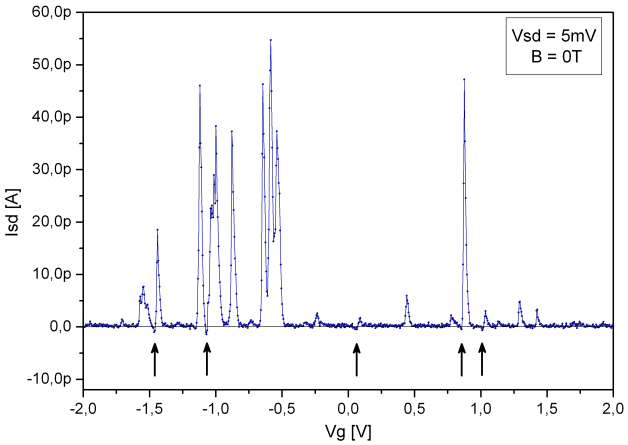

Figure 6.12: Gate scan at low bias voltage and zero magnetic field, arrows point the position of dips.

By decreasing the bias voltage we found that these dips became more pronounced. In Fig. 6.13 the measured current value I_{SD} at zero bias $V_{SD} = 0\,V$ is shown while the gate voltage is swept. Although there is no bias voltage applied one can observe a significant current flow through the device. The current oscillates between negative and positive values. This means that the flow direction depends on the level position of the dot. Actually

it is counterintuitive that current can flow without any potential difference at the source and drain contacts. Therefore we have to encounter other imbalances which could cause a net flow. The two gate scans in Fig. 6.13 were recorded one after the other but with changed sweep direction of the gate voltage. It is noticeable that the negative peaks occur mostly in pairs, it happens to be that the negative ones are always to the left of a positive one. This is the same for both scan directions. We can deduce from this that the flow direction of the current depends on the position of the QD level with respect to the Fermi level of the contacts. So whether the dot level is slightly above or below the Fermi level of the leads changes the current direction.

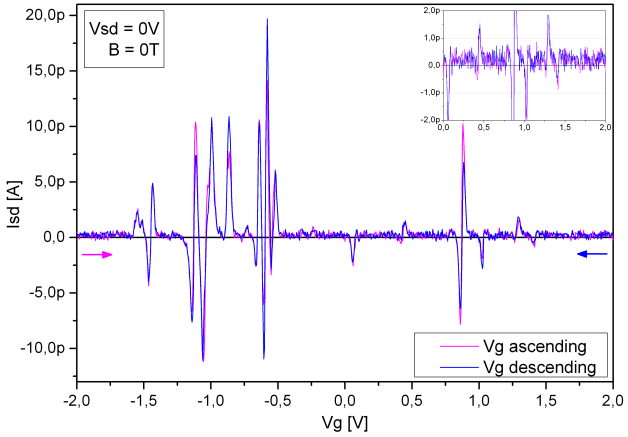

Figure 6.13: Gate scan at zero bias while gate voltage is swept in increasing and decreasing direction. Depending on the gate voltage a net current flow in both directions (±) is observable. Inset shows a magnified view of the measurement in order to visualize the offset and noise level.

In order to analyze this effect in detail a series of gate scans were taken at small bias voltages from +5 mV to -5 mV. For

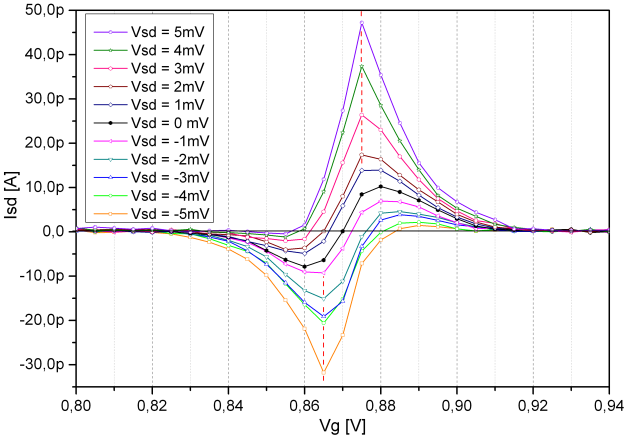

Figure 6.14: Current flow at zero bias (black dotted curve) and oppositely oriented current at small finite bias voltage.

clarity a zoom into this measurement around the gate voltage of +870 mV is shown in Fig. 6.14. With this measurement we can track the development of the oppositely oriented current. We can see that at zero bias (black line with full circles in the figure) the current levels in positive and negative direction have similar magnitude and are symmetric with respect to the intersection point of the x-axis. With increasing bias in one direction the current in the opposite direction reduces but is still present up to $\pm 5\,mV$.

A net current flow at zero bias can be achieved if the source and drain contacts couple asymmetrically to some external excitation fields. This has been experimentally demonstrated in a CNT-QD where microwave excitations give rise to photon-assited tunneling [109]. A similar imbalance is created for QDs with ferromagnetic contacts when the coupling to magnons in the contacts is asymmetric. This can be achieved when the tunnel or

spin wave coupling or the polarization of the contacts are different and this can cause a magnon-assited tunneling at zero bias [110]. Hereby an electron can enter or exit the dot by absorbing a magnon and flipping its orientation. If we assume the dot level to be slightly above the Fermi level of the contacts an electron can overcome this energy barrier by absorbing one magnon. Then the electron can leave the dot to both contacts. But the imbalance mentioned previously results in a net flow direction from the stronger coupled electrode to the weakly coupled one. Similarly if the level of the dot is below the Fermi level electrons can enter the dot from both contacts but the ratio of electrons leaving the dot by absorbing a magnon towards the stronger coupled electrode is higher and hence causes an oppositely oriented current.

For a better visualization of the negative current a 3D representation of the data from Fig. 6.14 is shown in Fig. 6.15a). To evaluate the conductance we have to look at the I-V curves. For this we can take cross-sections through the data as indicated by the white arrows and the red lines in the 3D representation. I-V curves obtained in this way are given in Fig. 6.15b). Although there are regions where current flows oppositely to the applied voltage as pointed by the black arrows, the trend for all three curves is an increasing current with increasing voltage. This means that the differential conductance of the SWNT-QD-SV is positive but with a negative or positive shift, depending on the level position. This offset seems also more likely to be the reason why the TMR extrema don´t coincide with the conductance maxima. We have seen in the previous section that they appear always slightly shifted to the right of the conductance peaks (see Fig. 6.11).

The spin valve measurements at zero bias revealed also im-

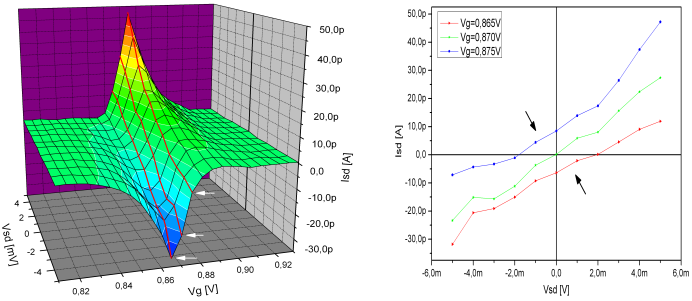

(a) (b)

Figure 6.15: a) 3D presentation of gate characteristics for the bias voltages between $\pm 5\,mV$ around Vg = 870 mV b) Three IV-curves obtained by cross sectioning the gate scan data at the positions indicated by the red curves and white arrows in a).

portant results. For this, the current signal at zero bias is measured at different gate voltages, while the magnetic fields is swept. The result is shown in Fig. 6.16. For clarity only the appropriate halfs of the measurements are shown in this graph. At gate voltages e.g. at $V_g = -480\,mV$, which is at the border between the Coulomb blockade region and a conductance peak, the current is almost at noise level. At this level there is also almost no TMR observable. By changing the gate voltage towards the conductance peak there is an enormous TMR observable. The TMR values for several different gate voltages with well different current values lie in this case all around 70 %. This is higher than the previously mentioned values at $V_{SD} = 30\,mV$ and they don´t show such a big variation as in the finite bias voltage case. The gate voltages and the corresponding TMR values at zero bias are given in Fig. 6.16.

In order to compare the SV effect at different gate voltages we have normalized the results to the current level at parallel

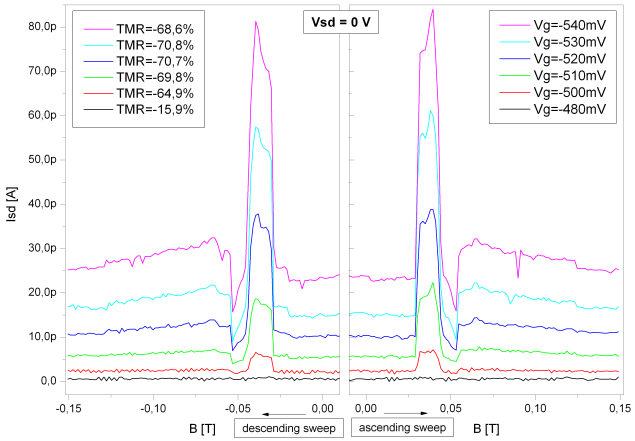

Figure 6.16: TMR at zero bias.

configuration I_p, as we did in the previous case. This is shown in Fig. 6.17. If we now compare the SV measurement at zero bias with SV measurements at finite bias as it was given in Fig. 6.6, we can deduce one significant difference. The magnitude of the TMR at zero bias shows no substantial variation with varying gate voltage. This suggests that ratio of the SV effect does not depend on the relative position of the dot level to the Fermi level, as long as it is in the energy window, which is reachable by the absorption of magnons. But as soon as a bias voltage is applied, the Fermi level window of the leads opens and the potential difference forces additionally the electrons to flow in a direction. We can interpret this behavior by the impairment through an additional effect which is disturbing the purely magnon assisted tunneling. There have been several proposals for MTJs to explain the decrease of TMR with increasing bias. All of them have difficulties to describe the behavior correctly. Among them, the decrease of spin polarization in the electrodes and spin relaxation

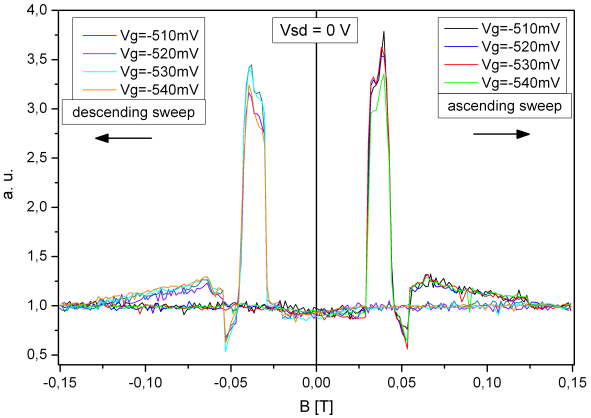

Figure 6.17: Normalized TMR at zero bias.

in the SWNT with increasing bias seem to be the more reasonable explanations. The effect of bias voltage on the nanodot contacted SWNT-QD-SVs are discussed in the next section.

Although the theory of magnon-driven electron transport was already mentioned in the literature [110], this is to the best of our knowledge the first time of its experimental indication. There has been already much experimental work on QDs with ferromagnetic contacts, but for low temperature transport measurements on QDs it is state of the art to use the lock-in-amplifier technique. During measurements with this technique there is always a small oscillating bias voltage applied to the sample and the obtained result is directly the differential conductance. As we have seen in Fig. 6.15 the slopes of the I-V curves do not change significantly between the negative and positive current direction. So during a conductance measurement the peaks of the positive and negative current peak can appear as a single one whereas during the direct measurement of the source drain current they appear as two. Due to the given measurement facilities we had

to measure directly the source drain current, but we were able to measure it at the very low level of pico-amperes. This might be the reason for our observation of current at zero bias in both directions depending on the level position.

6.5 The Effect of Bias Voltage on TMR

The results presented in the previous section have shown an enormously high TMR around -70% at zero bias, which was smaller at finite bias. This led us to investigate the effect of the bias voltage on the TMR. For this reason we have recorded the bias dependent current value (I-V) at the two different magnetic configurations of the electrodes. First the magnetic field was driven to negative saturation like for a SV measurement. Then it was swept in the ascending direction and stopped at $B = 0\,T$. Since this is still before the observed first switching, the magnetization of the electrodes was remaining in the parallel configuration. This is the parallel configuration for the ascending direction. Here the first I-V curve is recorded. Then the magnetic field is slowly increased up to a value well after the first switching and well before the second switching, in our case this was at +24 mT. At this value the magnetic configuration of the electrodes is antiparallel. Here again the I-V dependence is measured. Similar measurements are taken also for the descending direction. The I-V curves measured for the ascending and descending direction are shown in Fig. 6.18a) and b), respectively. One can already recognize from these curves the oscillating difference between the parallel and antiparallel state.

The TMR curves obtained from the I-V measurements are given in Fig. 6.19. Here we can recognize the strong bias dependence of the TMR. The higher TMR values occur at low bias but

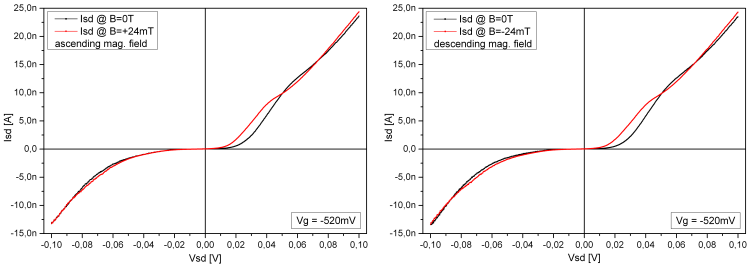

(a) (b)

Figure 6.18: IV curves taken at the parallel $B = 0\,T$ and antiparallel states $B = \pm 24\,mT$ a) in the ascending and b) in the descending magnetic field direction at $V_G = -520\,mV$.

it decays rapidly with increasing voltage. This is similar to the observation of other authors on carbon nanotube SV structures [54, 108, 111]. An interesting feature of our measurement are the extremum points as a result of the oscillating I-V curves. In our case there were three extremum points in both directions of the bias voltage but with reversed order. In addition it is also observable that the signal in the negative bias direction is significantly more noisy than in positive bias direction. This is a further indication of the asymmetric coupling of the electrodes.

Same measurements have also been conducted at a gate voltage of $V_G = -510\,mV$, which produced a similar result. This is presented in the middle part of Fig. 6.20. For both gate voltages we observed a high magnitude of TMR around -71% at zero bias. This is in a very good agreement with the direct SV measurements at zero bias presented in the previous section. With increasing bias the TMR not only decays rapidly but also changes sign to positive values. To verify this sign change we conducted again direct SV measurements at fixed bias voltages. Some of these measurements are given in the upper and lower

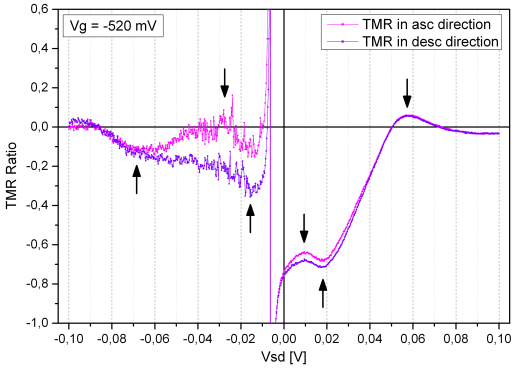

Figure 6.19: Bias dependence of TMR at $Vg = -520mV$ in both sweep directions of the magnetic field. It is noticeable that there are three local extremum points of TMR for both bias directions which are indicated by arrows.

panels of Fig. 6.20. Through these measurements we could confirm the sign change directly. These and some more of the direct SV measurement values are plotted on the TMR ratio graph as red dots. Here we can see the very good agreement between the direct SV measurement and the TMR values obtained from the I-V curves at the two different magnetic configurations.

The decay of the TMR signal with increasing bias and its sign change has been observed also on magnetic tunnel junctions [112, 113]. There have been several explanations discussed controversially. Zhang [114] and Bratkovsky [115] suggested a suppression of TMR with increasing bias due to the excitation of magnons at the interface between the tunneling barrier and the ferromagnet. But their explanation deviates at small bias voltages from experimental results e.g. by Moodera et al [113]. Impurities or defect states within the tunnel barrier are also discussed for thin-film MTJs [116]. Since they provide additional conduction channels which enhance spin mixing. Another expla-

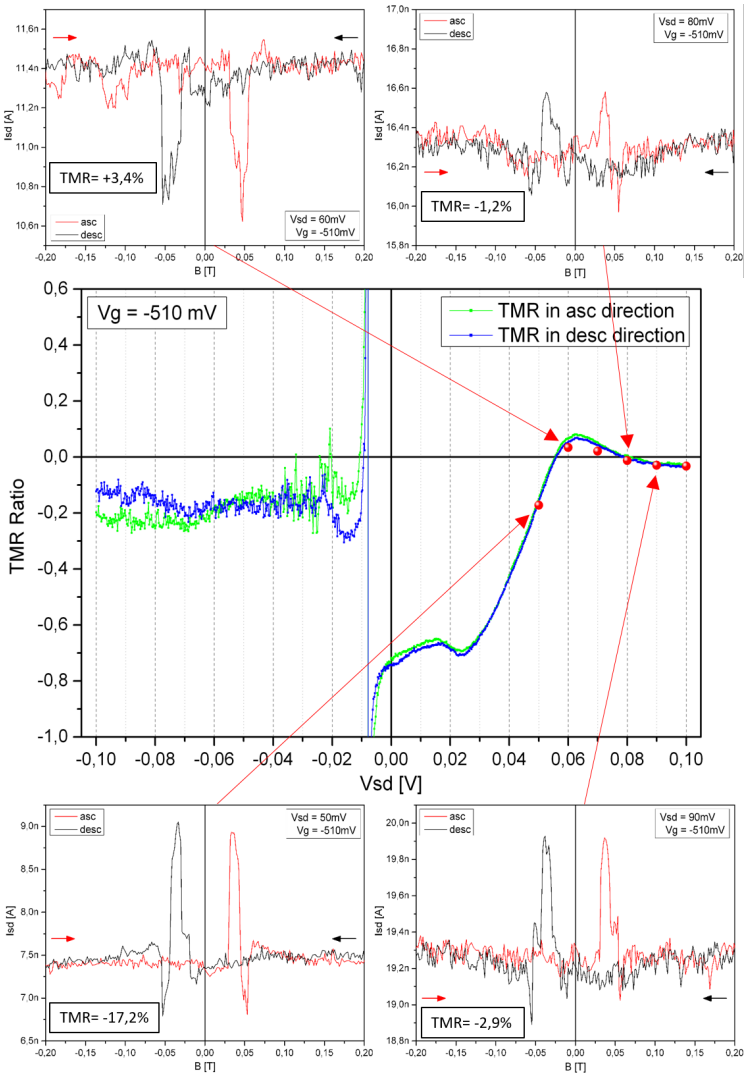

Figure 6.20: Bias dependence of TMR at $Vg = -510\,mV$ in the middle, red points are TMR values determined by direct SV measurement. The upper and lower small panels show the direct SV measurements at the given bias voltages. The arrows indicate to which point they correspond on the TMR curve obtained from I-V measurements.

nation given by Davis and MacLaren [117] suggests that the bias dependence of TMR is an intrinsic property of the ferromagnetic contacts. It is based on band structure changes and the change of the barrier shape with increasing bias voltage. This allows additional bands to contribute to the conduction and hence reduces the imbalance between the majority and the minority spin states. All these theories seem to explain the bias dependence of TMR to some extend, therefore it is accepted that all mechanisms contribute to this effect. Additionally a higher relaxation of the spin polarization within the SWNT with increasing bias may also play a role in carbon nanotube spin valve systems as suggested by Cottet et al. [118].

6.6 Conclusions

Based on our study of spin transport in carbon nanotubes we can conclude that the domain structure of the ferromagnetic contacts plays an important role in obtaining a clear spin signal in SWNT-QD-SV devices. Our investigation on the domain structure has verified that corners increase the possibility of multi domains. The successive switching of neighboring domains in a multi domain contact leads to undefinable measurement signals. But circular shaped contacts in a certain range of sizes do not build multi domains. So by using disk shaped ferromagnetic contacts, so called nanodots, the reversal mechanism of the magnetization is limited to two options (see Sec. 6.2). Based on this insight we were able to conduct several interesting experiments where we could investigate the spin transport in carbon nanotube quantum dots.

We observed a sharply defined, hysteretic change during our magnetic field dependent current measurements. At finite bias

voltage the change of the current was up to 250 % which yields a TMR ratio of ca. -60 %. By decreasing the bias voltage this ratio increased up to -70 %. This is so far the highest reported magnitude of TMR in carbon nanotube spin valve devices. We can conclude from this that the used contact geometry and the contact configuration with the Ti wetting layer is an appropriate choice to study spin polarized transport through SWNT-QDs. Further we can conclude that the spin polarization is preserved over the entire length of roughly 950 nm of the SWNT. Calculations based on this value and the Jullière model reveal a spin polarization degree of 48 % for cobalt. As discussed in Sec. 6.1 is this value in reasonable agreement with results mentioned in the literature.

Gate dependent measurements showed an oscillating TMR value between zero, within the Coulomb blockade regions and a high negative value in the conduction regions. The negative value is against the expectation based on measurements on magnetic thin films. In contrast to the situation in our devices, there are many parallel currents tunneling directly from one film to the other. This results in an averaged TMR ratio, which is closely related to the spin split density of states of the ferromagnet and is described by the two-current model. Whereas our device structure has a quantum dot inbetween the ferromagnets whose energy levels are quantized. Electrons can flow through such systems only if the energy levels are within certain limits and are blocked in the Coulomb blockade region. Therefore it is reasonable that TMR is reduced when current is blocked. In our system the tunneling to or from the ferromagnet should also be proportional to the density of states. But we observed mainly a negative TMR, which means a higher current flow when the magnetization is antiparallel. This indicates that in our devices

a major part of tunneling occurs in combination with a spin-flip.

Another observation made during this work, which is actually supporting the spin-flip proposal, is a net current at zero bias. We were able to measure a current flow at zero bias, the direction of which was changing depending on the position of the dot level with respect to the Fermi level of the contacts. A net current flow without a bias voltage can happen only if the system couples to an other excitation field and the coupling is asymmetric. As discussed in Sec. 6.4, we attribute this observation to the already theoretically predicted mechanism of magnon-assited tunneling, where electrons can overcome an energy barrier by absorbing a magnon. The absorption of magnons is an inelastic process which causes the aforementioned spin-flip. We can conclude from this that for QDs which couple asymmetrically to ferromagnetic contacts, magnon-assited tunneling plays an important role and is responsible for the negative TMR.

Our measurements showed also a strong dependence of the TMR on the bias voltage. The highest magnitude of TMR values occurred at zero bias, which decayed rapidly with increasing bias voltage. At zero bias the dependence of the TMR on the gate voltage was diminishingly small compared to its dependence at higher bias voltage. This means that when the Fermi levels of the contacts are aligned the relative position of the dot level in the vicinity of the Fermi level does not have an influence on the TMR. But as soon as a voltage is applied the Fermi level of the contacts are shifted and the difference between the parallel and antiparallel state currents decreases. From these results and the idea of magnon-assited tunneling with the connected spin-flip we can infer that increasing bias causes a decrease of the spin polarization. This might be, as also discussed by others, either due to changes in the band structure of the ferromagnet or to

change of the barrier shape or due to increasing spin relaxation within the carbon nanotube with increasing bias voltages (see. Sec. 6.5).

Chapter 7

Summary and Outlook

After the discovery of ***giant magnetoresistance (GMR)*** and the development of sensors based on this effect a new field of research and technology the so-called ***spintronics*** emerged. It is based on the idea to incorporate the spin degree of freedom of the electrons into electronics, which will open up new possibilities for computing and will be less energy consuming. It is seen as the next evolutionary step for information technology. Also the ***carbon nanotubes (CNT)*** have proven themselves as a highly innovative material for electronic applications. As shown by several others and discussed within this thesis, carbon nanotubes appear as a high potential candidate for spin transport. The main reason for this is their long spin coherence length due to the low spin-orbit coupling.

Many years after the discovery of carbon nanotubes and the invention of spintronics they are still amongst the very interesting research topics. But for both of them there are still big challenges to be solved. Many research groups investigating CNT-***quantum dots (QDs)*** with ferromagnetic contacts

suffer from spurious switching effects during ***spin valve (SV)*** measurements. The signal is either not clearly identified or not symmetric with respect to zero magnetic field or even shows step like switching behavior. According to our results these disturbances occur mainly with rectangular shaped contacts due to their multi domain configuration. Even if the contacts are very thin and narrow, multi domains appear if they are long enough. Spin valve like switching effects have been shown within a single Co nanowire with 35 nm diameter. This arises due to the successive switching of neighboring domains, while the current flows across the domain boundary between these domains. Therefore the main aim of this thesis was to find new ferromagnetic contact possibilities to overcome such disturbing effects.

To the best of our knowledge this work is the first one to conduct measurements on ***SWNT-QD-SV*** contacted with ferromagnetic circular thin-films. For the nanomagnetics community these structures are known as ***nanodots***. Main advantage of this type of contacts is that within certain size limits they are mainly in single domain state. But for slightly bigger sizes the vortex type domain configuration is also observable. It was possible for us by using Co nanodot contacted ***single-walled carbon nanotubes (SWNTs)*** to observe a sharply defined, symmetric and highly reproducible spin-valve effect with a high magnitude of up to $-70\,\%$. Additionally it was also possible to recognize the influence of magnetization reversal through vortex state on the SV signal.

The other aim of this thesis was to investigate spin transport through SWNTs. Here we were able to observe the correlation between the gate voltage and the ***tunneling magnetoresistance (TMR)***. The device under test showed mainly negative TMR. We could identify that highest magnitude of TMR val-

ues occur close to conductance maximum but with slightly shift towards higher gate voltages. One possible explanation of this shift, which was also observed by others, is the contribution of magnon-assited tunneling. The TMR signal showed also a strong dependence on the bias voltage. The highest values occur at low voltages and it decays rapidly with increasing bias voltage, but there is an additional modulation, which causes a sign change of the TMR signal. This sign change from negative to positive was also verified by direct SV measurements. The bias dependence of TMR showed also a strong noise on the signal on negative bias part which is attributed to an asymmetric coupling of leads to the QD.

An other important observation of this work was a significant current flow at zero bias. This observation was possible via the direct measurement of the source drain current at low level. The current flow showed an oscillatory behavior regarding its direction. Its flow direction was depending on the level position of the QD. Although this effect was already explained in theory as a ***magnon-driven current at zero bias*** the results presented in this thesis are, to the best of our knowledge, the first experimental indication of it. It is predicted to occur when the magnon coupling to the source and drain leads are asymmetric. The electrons can overcome the energy barrier to a higher or from a lower dot level by absorbing a magnon and since the coupling is different this results in a net flow direction. This gives than rise to a current flow in the positive of negative direction at zero bias voltage, when dot level is slightly above or below the Fermi level.

Almost all new research opens new windows and doors towards the unknown fields of knowledge. One can have a look through or step into it. Keeping the tradition this work raised

also new questions and answered some of the old ones. Therefore it is worthwhile to mention some of the future tasks which might help to shine some more light into the darkness. Since nanodots offer a better identification of the spin signal it is now important to realize samples with smaller nanodots. This will guarantee the single domain switching behavior. At the same time it is also important to realize samples with two vortex type contacts. For this type of SWNT-QD-SVs one can change the position of the nucleation and annihilation point of the vortex by rotating the sample relatively to the applied magnetic field. This would give the possibility to study until which distance from the contact point of the CNT the magnetic orientation has an influence on the spin signal. Further experiments should be conducted on the temperature dependence of the TMR down to temperatures well below 1K. Here one could reduce the temperature smearing effect and resolve the single particle states more clearly. Finally the temperature dependence of magnon-assited tunneling and of magnon-driven current at zero bias will open-up new possibilities to investigate the role of magnons in spin transport.

Bibliography

[1] Wikipedia, "Information age — wikipedia, the free encyclopedia," 2017. [Online; accessed 19-June-2017].

[2] G. E. Moore, "Cramming more components onto integrated circuits," *Electronics* **38**, pp. 114–117, April 1965.

[3] ITRS Committee, "International technology roadmap for semiconductors." http://www.itrs2.net/itrs-reports.html.

[4] L. D. Landau and E. M. Lifshitz, *Quantum Mechanics: non-relativistic theory*, Pergamon Press, 1965.

[5] S. A. Wolf, D. D. Awschalom, R. A. Buhrman, J. M. Daughton, S. von Molnar, M. L. Roukes, A. Y. Chtchelkanova, and D. M. Treger, "Spintronics: A Spin-Based Electronics Vision for the Future," *Science* **294**(5546), pp. 1488–1495, 2001.

[6] M. N. Baibich, J. M. Broto, A. Fert, F. N. Van Dau, F. Petroff, P. Etienne, G. Creuzet, A. Friederich, and J. Chazelas, "Giant magnetoresistance of (001)Fe/(001)Cr magnetic superlattices," *Phys. Rev. Lett.* **61**, pp. 2472–2475, November 1988.

[7] G. Binasch, P. Grünberg, F. Saurenbach, and W. Zinn, "Enhanced magnetoresistance in layered magnetic structures with antiferromagnetic interlayer exchange," *Phys. Rev. B* **39**, pp. 4828–4830, Mar 1989.

[8] S. Ikeda, J. Hayakawa, Y. Ashizawa, Y. M. Lee, K. Miura, H. Hasegawa, M. Tsunoda, F. Matsukura, and H. Ohno, "Tunnel magnetoresistance of 604 % at 300 K by suppression of Ta diffusion in CoFeB/MgO/CoFeB pseudo-spin-valves annealed at high temperature," *Appl. Phys. Lett.* **93**, p. 082508, 2008.

[9] M. Bowen, M. Bibes, A. Barthelemy, J.-P. Contour, A. Anane, Y. Lemaitre, and A. Fert, "Nearly total spin polarization in $La_{2/3}Sr_{1/3}MnO_3$ from tunneling experiments," *Appl. Phys. Lett.* **82**(2), pp. 233–235, 2003.

[10] C. Buchal and D. Bürgler, "Peter Grünberg Nobelpreis für Physik 2007." Forschungszentrum Jülich GmbH in der Helmholtz-Gemeischaft, 2008.

[11] L. Geppert, "A giant leap for disk drives," *IEEE Spectrum* **35**, p. 23, 1998.

[12] S. Iijima, "Helical microtubules of graphitic carbon," *Nature* **354**, p. 56, November 1991.

[13] M. F. L. D. Volder, S. H. Tawfick, R. H. Baughman, and A. J. Hart, "Carbon nanotubes: Present and future commercial applications," *Science* **339**, pp. 535–539, 2013.

[14] W. Marx and A. Barth, "Carbon nanotubes - a scientometric study," *Phys. Stat. Sol. B* **245**, pp. 2347–2351, September 2008.

[15] A. Barth and W. Marx, "Graphene - a rising star in view of scientometrics." Private communications, August 2009. Used Sources: Thomson Reuters SCI and CPCI-S under the Web of Science (WoS) and STN International (SCI growth).

[16] M. Endo, *Mecanisme de croissance en phase vapeur de fibres de carbone*. PhD thesis, L'Universite D'Orleans, October 1975.

[17] A. Thess, R. Lee, P. Nikolaev, H. Dai, P. Petit, J. Robert, C. Xu, Y. H. Lee, S. G. K. nd Andrew G. Rinzler, D. T. Colbert, G. Scuseria, D. Tománek, J. E. Fischer, and R. E. Smalley, "Crystalline ropes of metallic carbon nanotubes," *Science* **273**, pp. 483–487, July 26 1996.

[18] P. Kohler-Redlich. MPI for Metals Research, Stuttgart.

[19] R. Saito, G. Dresselhaus, and M. Dresselhaus, *Physical Properties of Carbon Nanotubes*, Imperial College Press, 1998.

[20] A. H. Castro Neto, F. Guinea, N. M. R. Peres, K. S. Novoselov, and A. K. Geim, "The electronic properties of graphene," *Rev. Mod. Phys.* **81**, pp. 109–162, January 2009.

[21] "Graphene Brillouin Zone and Electronic Energy Dispersion" from The Wolfram Demonstrations Project http://demonstrations.wolfram.com/GrapheneBrillouinZoneAndElectronicEnergyDispersion/ Contributed by: Vladimir Gavryushin (Vilnius University, Lithuania).

[22] J.-C. Charlier, X. Blase, and S. Roche, "Electronic and transport properties of nanotubes," *Rev. Mod. Phys.* **79**, pp. 677–732, May 2007.

[23] "Electronic Band Structure of a Single-Walled Carbon Nanotube by the Zone-Folding Method" from The Wolfram Demonstrations Project http://demonstrations.wolfram.com/ElectronicBandStructureOfASingle WalledCarbonNanotubeByTheZon/ Contributed by: Jessica Alfonsi (University of Padova, Italy).

[24] "Brillouin Zone of a Single-Walled Carbon Nanotube" from The Wolfram Demonstrations Project http://demonstrations.wolfram .com/BrillouinZoneOfASingleWalledCarbonNanotube/ Contributed by: Jessica Alfonsi (University of Padova, Italy).

[25] T. Sun, T. Zeng, C. Xia, S. Li, and H. Wu, "Purification and separation of single-walled carbon nanotubes (SWCNTs)," *J. Nanosci. Nanotechnol.* **12**, pp. 2955–2963, 2012.

[26] R. Saito, M. Fujita, G. Dresselhaus, and M. S. Dresselhaus, "Electronic structure of chiral graphene tubules," *Appl. Phys. Lett.* **60**(18), pp. 2204–2206, 1992.

[27] W. Hoenlein, G. S. Duesberg, A. P. Graham, F. Kreupl, M. Liebau, werner Pamler, R. Seidel, and E. Unger, "Nanoelectronics beyond silicon," *Microelectron. Eng.* **83**, pp. 619–623, 2006.

[28] M. M. Shulaker, G. Pitner, G. Hills, M. Giachino, H. S. P. Wong, and S. Mitra, "High-performance carbon nanotube

field-effect transistors," in *2014 IEEE International Electron Devices Meeting*, pp. 33.6.1–33.6.4, Dec 2014.

[29] S. Ilani and P. L. McEuen, "Electron transport in carbon nanotubes," *Annu. Rev. Condens. Matter Phys.* **1**, pp. 1–25, 2010.

[30] J. Kong, E. Yenilmez, T. W. Tombler, W. Kim, H. Dai, R. B. Laughlin, L. Liu, C. S. Jayanthi, and S. Y. Wu, "Quantum interference and ballistic transmission in nanotube electron waveguides," *Phys. Rev. Lett.* **87**, p. 106801, Aug 2001.

[31] W. Liu, C. Hierold, and M. Haluska, "Electrical contacts to individual SWCNTs: A review," *Beilstein J. Nanotechnol.* **5**, pp. 2202–2215, 2014.

[32] E. A. Laird, F. Kuemmeth, G. A. Steele, K. Grove-Rasmussen, J. Nygård, K. Flensberg, and L. P. Kouwenhoven, "Quantum transport in carbon nanotubes," *Rev. Mod. Phys.* **87**, pp. 703–764, Jul 2015.

[33] L. P. Kouwenhoven, C. Marcus, P. L. McEuen, S. Tarucha, R. Westerwelt, and N. Wingreen, *Electron Tansport in Quantum Dots*, vol. 345 of *NATO Advanced Studies Institute Series E: Applied Sciences*, p. 16. Kluwer Academics, 1997.

[34] W. Liang, M. Bocrath, and H. Park, "Shell filling and exchange coupling in metallic single-walled carbon nanotubes," *Phys. Rev. Lett.* **88**(12), p. 126801, 2002.

[35] R. Hanson, L. P. Kouwenhoven, J. R. Petta, S. Tarucha, and L. M. K. Vandersypen, "Spins in few-electron quantum dots," *Rev. Mod. Phys.* **79**, pp. 1217–1265, Oct 2007.

[36] D. H. Cobden and J. Nygård, "Shell filling in closed single-wall carbon nanotube quantum dots," *Phys. Rev. Lett.* **89**, p. 046803, Jul 2002.

[37] G. E. Uhlenbeck and S. Goudsmit, "Ersetzung der Hypothese vom unmechanischen Zwang durch eine Forderung bezüglich des inneren Verhaltens jedes einzelnen Elektrons," *Die Naturwissenschaften* **13**, pp. 953–954, November 1925.

[38] S.-I. Tomonaga, *The Story of Spin*, University of Chicago Press, 1997.

[39] W. Gerlach and O. Stern, "Der experimentelle Nachweis der Richtungsquantelung im Magnetfeld," *Zeitschrift für Physik* **9**(1), pp. 349–352, 1922.

[40] S. Datta and B. Das, "Electronic analog of the electro-optic modulator," *Appl. Phys. Lett.* **56**, pp. 665–667, February 1990.

[41] C.-G. Sefanita, *Magnetism Basics and Applications*, Springer, 2012.

[42] R. Winkler and M. Oestreich, "Spinelektronik - Das Potential des Elektronenspins in der Halbleiterelektronik," *Physik Journal* **3**, pp. 39–44, 2004.

[43] G. Schmidt, D. Ferrand, L. Molenkamp, A. Filip, and B. van Wees, "Fundamental obstacle for electrical spin injection from a ferromagetic metal into a diffusive semiconductor," *Phys. Rev. B* **62**, pp. R4790–R4793, 2000.

[44] H. Ohno, "Making nonmagnetic semiconductors ferromagnetic," *Science* **281**, pp. 951–956, August 1998.

[45] A. H. MacDonald, P. Schiffer, and N. Samarth, "Ferromagneic semiconductors: moving beyond (Ga,Mn)As," *Nat. Mater.* **4**, pp. 195–202, March 2005.

[46] T. Jungwirth, J. Sinova, J. Masek, J. Kucera, and A. H. MacDonald, "Theory of ferromagnetic (III,Mn)V semiconductors," *Rev. Mod. Phys.* **78**, pp. 809–864, July 2006.

[47] D. Qu, S. Y. Huang, J. Hu, R. Wu, and C. L. Chien, "Intrinsic spin seebeck effect in au/yig," **110**, p. 067206, 2013.

[48] J. Gregg, I. Petej, E. Jouguelet, and C. Dennis, "Spin electronics - a review," *J. Phys. D: Appl. Phys.* **35**, pp. R121–R155, September 2002.

[49] R. Gross and A. Marx, *Festkörperphysik*, De Gruyter Studium, De Gruyter, 2014.

[50] I. Zutic, J. Fabian, and S. D. Sarma, "Spintronics: Fundamentals and applications," *Rev. Mod. Phys.* **76**, pp. 323–410, April 2004.

[51] K. Tsukagoshi, B. Alphenaar, and H. Ago, "Coherent transport of electron spin in a ferromagnetically contacted carbon nanotube," *Nature* **401**, pp. 572–574, October 1999.

[52] D. Orgassa, G. Mankey, and H. Fujiwara, "Spin injection into carbon nanotubes and a possible application in spin-resolved scanning tunnelling microscopy," *Nanotechnology* **12**, pp. 281–284, September 2001.

[53] S. Sahoo, T. Kontos, C. Schonenberger, and C. Surgers, "Electrical spin injection in multiwall carbon nanotubes with transparent ferromagnetic contacts," *Appl. Phys. Lett.* **86**, p. 112109, March 2005.

[54] B. Zhao, I. Mönch, H. Vinzelberg, T. Mühl, and C. M. Schneider, "Spin-coherent transport in ferromagnetically contacted carbon nanotubes," *Appl. Phys. Lett.* **80**(17), pp. 3144–3146, 2002.

[55] L. E. Hueso, J. M. Pruneda, V. Ferrari, G. Burnell, J. P. Valdes-Herrera, B. D. Simons, P. B. Littlewood, E. Artacho, A. Fert, and N. D. Mathur, "Transformation of spin information into large electrical signals using carbon nanotubes," *Nature* **445**, pp. 410–413, January 2007.

[56] J. Kim, H. So, J. Kim, and J. Kim, "Spin-dependent transport properties in a single-walled carbon nanotube with mesoscopic Co contacts," *Phys. Rev. B* **66**, p. 233401, December 2002.

[57] S. Sahoo, T. Kontos, J. Furer, C. Hoffmann, M. Graber, A. Cottet, and C. Schonenberger, "Electric field control of spin transport," *Nat. Phys.* **1**, pp. 99–102, November 2005.

[58] A. Jensen, J. Hauptmann, J. Nygard, and P. Lindelof, "Magnetoresistance in ferromagnetically contacted single-wall carbon nanotubes," *Phys. Rev. B* **72**, p. 035419, July 2005.

[59] A. Jensen, J. Nygard, and J. Borggreen, "Single-wall carbon nanotubes with ferromagnetic electrodes," in *Towards the Controllable Quantum States: Mesoscopic Superconductivity and Spintronics*, Takayanagi, H and Nitta, J, ed., pp. 33–37, 2003. 2nd International Symposium on Mesoscopic Superconductivity and Spintronics, Atsugi, Japan, March 04-06, 2002.

[60] É. Du Trémolet de Lacheisserie, D. Gignoux, and M. Schlenker, *Magnetism*, Grenoble Sciences, Springer, 2005.

[61] M. V. Berry and A. K. Geim, "Of flying frogs and levitrons," *Eur. J. Phys* **18**, pp. 307–313, 1997.

[62] B. D. Cullity and C. D. Graham, *Introduction to Magnetic Materials*, IEEE/Wiley, 2 ed., 2009.

[63] P. Weiss, "L'hypothese du champ moleculaire et la propriete ferromagnetique," *J. de Phys. Rad.* **6**, pp. 661–690, 1907.

[64] C. Kittel, *Introduction to Solid State Physics*, Wiley, 8 ed., 2005.

[65] N. Ashcroft and D. Mermin, *Festkörperphysik*, Oldenbourg Wissenschaftsverlag, 2012.

[66] H. Barkhausen, "Zwei mit Hilfe der neuen Verstärker entdeckte Erscheinungen," *Physikalishce Zeitschrift* **20**, pp. 401–403, 1919.

[67] A. Hubert and R. Schäfer, *Magnetic Domains: The Analysis of Magnetic Microstructures*, Springer Berlin Heidelberg, 2008.

[68] S. Blundell, *Magnetism in Condensed Matter*, Oxford University Press, 2001.

[69] S. Hunklinger, *Festkörperphysik*, De Gruyter, 4 ed., 2014.

[70] J. Janak, "Uniform susceptibilities of metallic elements," *Phys. Rev. B* **16**(1), pp. 255–262, 1977.

[71] C. S. Callaway and C. S. Wang, "Self-consistent calculation of energy bands in ferromagnetic nickel," *Phys. Rev. B* **7**, pp. 1096–1103, 1973.

[72] J. Stöhr and H. C. Siegmann, *Magnetism*, Springer, 2006.

[73] J. M. D. Coey, *Magnetism and Magnetic Materials*, Cambridge University Press, 2009.

[74] N. Mott, "Electrical conductivity of transition metals," *Proceedings of the Royal Society of London* **153A**, pp. 699–717, February 1936.

[75] A. Fert and I. A. Campbell, "Two-current conduction in nickel," *Phys. Rev. Lett.* **21**, p. 1190, October 1968.

[76] I. A. Campbell and A. Fert, *Ferromagnetic Materials - A Handbook on the properties of magneticordered substances*, vol. 3, North-Holland Publishing Company, 1982.

[77] S. S. P. Parkin, N. More, and K. P. Roche, "Oscillations in exchange coupling and magnetoresistance in metallic superlattice structures: Co/Ru, Co/Cr, and Fe/Cr," *Phys. Rev. Lett.* **64**, p. 2304, 1990.

[78] A. Fert, "Nobel lecture: Origin, development, and future of spintronics," *Rev. Mod. Phys.* **80**(4), p. 1517, 2008.

[79] J. Mathon, "Phenomenological theory of giant magnetoresistance," in *Spin Electronics*, M. Ziese and M. J. Thornton, eds., pp. 71–88, Springer, 2001.

[80] M. Julliere, "Tunneling between ferromagnetic films," *Phys. Lett. A* **54**, p. 225, 1975.

[81] S. Yuasa, T. Nagahama, A. Fukushima, Y. Suzuki, and K. Ando, "Giant room-temperature magnetoresistance in single crystal Fe/MgO/Fe magnetic tunnel junctions," *Nature Materials* **3**, pp. 868–871, 2004.

[82] S. S. P. Parkin, C. Kaiser, A. Panchula, P. M. Rice, B. Hughes, M. Samant, and S. H. Yang, "Giant tunneling magnetoresistance at room temperature with MgO (100) tunnel barriers," *Nature Materials* **3**, pp. 862–867, 2004.

[83] R. Meservey, P. M. Tedrow, and P. Fulde, "Magnetic field splitting of the quasiparticle states in superconducting aluminum films," *Phys. Rev. Lett.* **25**, pp. 1270–1272, Nov 1970.

[84] P. M. Tedrow and R. Meservey, "Spin-dependent tunneling into ferromagnetic nickel," *Phys. Rev. Lett.* **26**, pp. 192–195, Jan 1971.

[85] E. Y. Tsymbal, O. N. Mryasov, and P. R. LeClair, "Spin-dependent tunneling in magnetic tunnel junctions," *J. Phys.: Condens. Matter* **15**, pp. R109–R142, 2003.

[86] R. Meservey and P. Tedrow, "Spin-polarized electron tunneling," *Phys. Rep.* **238**(4), pp. 173–243, 1994.

[87] J. S. Moodera, J. Nassar, and G. Mathon, "Spin-tunneling in ferromagnetic junctions," *Annu. Rev. Mater. Sci.* **29**(1), pp. 381–432, 1999.

[88] D. J. Monsma and S. S. P. Parkin, "Spin polarization of tunneling current from ferromagnet/Al_2O_3 interfaces using copper-doped aluminum superconducting films," *Appl. Phys. Lett.* **77**(5), pp. 720–722, 2000.

[89] G. J. Strijkers, Y. Ji, F. Y. Yang, C. L. Chien, and J. M. Byers, "Andreev reflections at metal/superconductor point contacts: Measurement and analysis," *Phys. Rev. B* **63**, p. 104510, Feb 2001.

[90] U. Ebels, A. Radulescu, H. Y., L. Piraux, and K. Ounadjela, "Spin accumulation and domain wall magnetoresistance in 35 nm co wires," *Phys. Rev. Lett.* **84**, pp. 983–986, 2000.

[91] G. Binnig, H. Rohrer, C. Gerber, and E. Weibel, "Surface studies by scanning tunneling microscopy," *Phys. Rev. Lett.* **49**(1), pp. 57–61, 1982.

[92] G. Binnig, C. Quate, and C. Gerber, "Atomic force microscope," *Phys. Rev. Lett.* **56**(9), pp. 930–933, 1986.

[93] E. Meyer, H. J. Hug, and R. Bennewitz, *Scanning Probe Microscopy*, Springer, 2003.

[94] R. Cowburn, D. Koltsov, A. Adeyeye, M. Welland, and D. Tricker, "Single-domain circular nanomagnets," *Phys. Rev. Lett.* **83**(5), pp. 1042–1045, 1999.

[95] I. L. Prejbeanu, M. Natali, L. D. Buda, U. Ebels, A. Lebib, Y. Chen, and K. Ounadjela, "In-plane reversal mechanisms in circular Co dots," *J. Appl. Phys.* **91**, pp. 7343–7345, 2002.

[96] M. Haluska, M. Hulman, B. Hornbostel, J. Cech, V. Skakalova, and S. Roth, "Synthesis of SWCNTs for C82 peapods by arc-discharge process using nonmagnetic catalysts," *Phys. Status Solidi B* **243**(13), pp. 3042–3045, 2006.

[97] J. N. Coleman, "Liquid-phase exfoliation of nanotubes and graphene," *Adv. Funct. Mater.* **19**(23), pp. 3680–3695, 2009.

[98] G.-T. Kim, U. Waizmann, and S. Roth, "Simple efficient coordinate markers for investigating synthetic nanofibers," *Appl. Phys. Lett.* **79**(21), pp. 3497–3499, 2001.

[99] C.-W. Liang, S. Sahakalkan, and S. Roth, "Electrical characterization of the mutual influences between gas molecules and single-walled carbon nanotubes," *Small* **4**, pp. 432–436, 2008.

[100] C.-W. Liang, *Electrical Characterization of Carbon Nanotubes for Electronics.* PhD thesis, Eberhard-Karls-Universität zu Tübingen, 2009.

[101] H. F. Ding, A. K. Schmid, D. Li, K. Y. Guslienko, and S. D. Bader, "Magnetic bistability of Co nanodots," *Phys. Rev. Lett.* **94**, p. 157202, Apr 2005.

[102] A. Fernandez, M. Gibbons, M. Wall, and C. Cerjan, "Magnetic domain structure and magnetization reversal in submicron-scale Co dots," *J. Magn. Magn. Mater.* **190**(1-2), pp. 71 – 80, 1998.

[103] N. M. Vargas, S. Allende, B. Leighton, J. Escrig, J.Mejia-Lopez, D. Altbir, and I. K. Schuller, "Asymmetric magnetic dots: A way to control magnetic properties," *J. Appl. Phys.* **109**, p. 073907, 2011.

[104] W. L. Pei, G. W. Qin, Y. P. Ren, S. Li, T. Wang, H. Hasegawa, S. Ishio, and H. Yamane, "Incoherent magnetization reversal in Co-Pt nanodots investigated by mag-

netic force microscopy," *Acta Mater.* **59**, pp. 4818–4824, 2011.

[105] R. K. Dumas, K. Liu, C.-P. Li, I. V. Roshchin, and I. K. Schuller, "Temperature induced single domain-vortex state transition in sub-100nm Fe nanodots," *Appl. Phys. Lett.* **91**(20), p. 202501, 2007.

[106] Y. V. Nazarov and Y. M. Blanter, *Quantum Transport*, Cambridge University Press, 2009.

[107] A. D. Martino and R. Egger, "Rashba spin-orbit coupling and spin precession in carbon nanotubes," *J. Phys.: Condens. Matter* **17**(36), p. 5523, 2005.

[108] H. T. Man, I. J. W. Wever, and A. F. Morpurgo, "Spin-dependent quantum interference in single-wall carbon nanotubes with ferromagetic contacts," *Phys. Rev. B.* **73**, p. 241401, 2006.

[109] C. Meyer, J. M. Elzerman, and L. P. Kouwenhoven, "Photon-assited tunneling in a carbon nanotube quantum dot," *Nano Lett.* **7**(2), pp. 295–299, 2007.

[110] B. Sothmann, J. König, and A. Kadigrobov, "Influence of spin waves on transport through a quantum-dot spin valve," *Phys. Rev. B* **82**, p. 205314, 2010.

[111] S. Sahoo, *An Experimental Investigation of Spin Polarized Transport in Carbon Nanotubes.* PhD thesis, University of Basel, 2005.

[112] E. Y. Tsymbal, A. Sokolov, I. F. Sabrianov, and B. Doudin, "Resonant inversion of tunneling magnetoresistance," *Phys. Rev. Lett.* **90**, p. 186602, 2003.

[113] J. S. Moodera, J. Nowak, and R. J. M. van de Veerdonk, "Interface magnetism and spin wave scattering in ferromagnet-insulator-ferromagnet tunnel junctions," *Phys. Rev. Lett.* **80**, p. 2941, 1998.

[114] S. Zhang, P. M. Levy, A. C. Marley, and S. S. P. Parkin, "Quenching of magnetoresistance by hot electrons in magnetic tunnel junctions," *Phys. Rev. Lett.* **79**, pp. 3744–3747, Nov 1997.

[115] A. M. Bratkovsky, "Assisted tunneling in ferromagnetic junctions and half-metallic oxides," *Appl. Phys. Lett.* **72**, p. 2334, 1998.

[116] H. Swagten, "Spin-dependent tunneling in magnetic junctions," in *Handbook of Magnetic Materials*, K. Buschow, ed., pp. 1–121, Elsevier, 2007.

[117] A. H. Davis and J. M. MacLaren, "Spin dependent tunneling at finite bias," *J. Appl. Phys.* **87**, p. 5224, 2000.

[118] A. Cottet, T. Kontos, S. Sahoo, H. T. Man, M.-S. Choi, W. Belzig, C.Bruder, A. F. Morpurgo, and C. Schonenberger, "Nanospintronics with carbon nanotubes," *Semicond. Sci. Technol.* **21**, pp. S78–S95, 2006.

Acknowledgments

First of all I would like to thank my *Doktorvater* Prof. Dieter Kern from the *University of Tuebingen* for his support and the encouragement to continue scientific research.

I am also very grateful to Prof. Klaus von Klitzing for giving me the opportunity to join his department at the *Max Planck Institute for Solid State Research* with its fruitful scientific atmosphere and tremendous facilities and also his endless support.

Special thanks go of course to my supervisor Prof. Siegmar Roth for his excellent knowledge and guidance from which I could benefit and also for his endless patience and support. Without him it would not be possible to finish this work. Thanks for all the interesting discussions about science, history, the god and everything. I will be always in your debt.

I also appreciate the collaboration with my friendly colleague Dr. Chen-Wei Liang, who triggered the spintronic measurements in our Group. I thank him especially for the lively discussions and nightly measurement sessions we had.

Furthermore I would like to thank Dr. Viera Skakalova for all the scientific and not scientific discussions and her esteem towards me and my work. Special thanks also go to Dr. Viktor Siegle for his endurance in calling, mailing and texting me.

I am also deeply grateful to Dr. Ursula Dettlaff and Dr. Miro

Haluska for the special nanotube material which was a crucial ingredient for this work.

It is also a great pleasure to acknowledge the support from the members of the *Synthetic Nanostructures Group* our special 4C11 team. It was a valuable experience to work with Dr. Martti Kaempgen, Dr. Dirk Obergfell, Dr. Michael Lebert, Dr. Björn Hornbostel, Dr. Jannik Meyer, Dr. Guisy Scalia, Dr. Alberto Ansaldo, Dr. Monica Jung de Andrade, Dr. Marcio Dias Lima and all the others.

Some of the key essential devices for the experiments were provided by Dr. Jürgen Weis, Dr. Jürgen Smet and Dr. Werner Dietsche, therefore my gratitude extends to them.

I have also benefited much from the technical services especially the help by Ulrike Waizmann, Thomas Reindl, Monika Riek, Achim Güth, Manfred Schmid, Ingo Hagel and Steffen Wahl, sincere thanks go also to them.

My final acknowledgments I dedicate to my beloved family for their support and understanding and especially I dedicate to my wife Ayse for her endless patience and her believe in me.